UNIVERSITÉ DU LUXEMBOURG

PhD-FSTM-2023-076
The Faculty of Science, Technology and Medicine

DISSERTATION

Defence held on 12/09/2023 in Esch-sur-Alzette

to obtain the degree of

DOCTEUR DE L'UNIVERSITÉ DU LUXEMBOURG

EN PHYSIQUE

by

Alfredo Blázquez Martínez
Born on 02 December 1996 in Baeza (Spain)

PHOTOFERROELECTRIC EFFECTS IN POLYCRYSTALLINE BISMUTH FERRITE

Dissertation defence committee

Dr. Mael Guennou, Chair
Assistant Professor, University of Luxembourg

Dr. Morgan Trassin, Vice Chair
Professor, Eidgenössische Technische Hochschule Zürich

Dr. Torsten Granzow, Supervisor
Lead Researcher, Luxembourg Institute of Science and Technology

Dr. Barbara Malič
Professor, Jožef Stefan Institute

Dr. Josep Fontcuberta
Professor, Institute of Materials Science of Barcelona

Dr. Sebastjan Glinsek, Expert in an advisory capacity
Senior Researcher, Luxembourg Institute of Science and Technology

Affidavit

I hereby confirm that the Ph.D. thesis entitled "*Photoferroelectric effects in polycrystalline bismuth ferrite*" has been written independently and without any other sources than cited.

Luxembourg, 22/10/2023

Name Alfredo Blázquez Martínez

Acknowledgements

I would like to express my gratitude to the Fonds National de la Recherche (FNR) for funding my Ph.D. studies under the PACE project (PRIDE17/12246511/PACE). Additionally, I would like to extend my thanks to the COST Action: European Network for Innovative and Advanced Epitaxy, for providing funding for my short-term scientific mission at ETH Zürich.

I would also like to acknowledge the University of Luxembourg for fostering a challenging atmosphere that facilitated both personal and scientific development throughout my studies. Furthermore, I am grateful to the Luxembourg Institute of Science and Technology for providing the necessary infrastructure and support for conducting most of the experiments included in this thesis.

This thesis was possible thanks to the support of numerous scientists. First and foremost, I would like to express my gratitude to my supervisor and scientific mentor, Dr. Torsten Granzow. Thank you for placing your trust in me for this project and for being an exceptional mentor. You guided me in becoming a rigorous physicist. I cannot adequately express my gratitude for all your efforts over these years. Your supervision approach and unwavering support are deeply appreciated.

I would also like to thank my co-supervisor, Dr. Sebastjan Glinsek. Everything I know about the solution-deposition of complex oxides, I owe to you. Thank you for your support during these four years, especially during the reviewer fighting rounds.

Additionally, I would like to express my gratitude to our group leader, Dr. Emmanuel Defay. If all managers in academia were like you, academia would undoubtedly be healthier. I am sincerely thankful for the opportunity to be part of your team.

Thank you to Prof. Dr. Mael Guennou and Prof. Dr. Barbara Malic for their invaluable contribution as members of my thesis supervision committee. I deeply appreciate the support throughout my doctoral studies. I would also like to thank Prof. Dr. Josep Fontcuberta for being part of my dissertation defense committee and reviewing this thesis. Furthermore, I want to express my special appreciation to Prof. Dr. Morgan Trassin for being part of my dissertation defense committee and for hosting me at ETH

Zürich as part of the COST Opera action. I am truly grateful for the knowledge and skills I acquired under his guidance, particularly in the epitaxial growth of complex oxides and scanning probe microscopy techniques.

Science is no longer an individual pursuit but a collaborative endeavor that thrives on partnerships, exchanges, and interdisciplinary discussions. Therefore, I would like to acknowledge and express my deep appreciation for the invaluable contributions of all the internal and external collaborators who dedicated their time to make this dissertation possible.

First, thanks to Dr. Andreja Bencan and her team. Their expertise in transmission electron microscopy was crucial in acquiring a better understanding of the films' microstructure.

I would also like to thank Dr. Stéphanie Girod, whose guidance was key in shaping my understanding of lithography. Thank you for introducing me to the art of working with our beloved MLA and for engaging in numerous fruitful discussions in the cleanroom.

I am grateful to Patrick Grysan for introducing me to scanning probe microscopy and teaching me about lock-in detection techniques, which were essential in obtaining the electro-optic results. Your expertise has been invaluable.

I would also like to thank Dr. Constance Toulouse for introducing me to the fascinating world of negative pressure. I have thoroughly enjoyed our scientific and non-scientific discussions. I am grateful for the knowledge and insights gained through our interactions.

While I may inadvertently overlook some people, I would like to thank all the collaborators from the University of Luxembourg and the Luxembourg Institute of Science and Technology who contributed to this work. Your collective efforts have played a significant role in its success.

This thesis could not have been possible without the support of all members of the Ferroic Materials for Transducers group, and my colleagues at LIST. My heartfelt thanks go to my two Luxembourg siblings, Poorani and Longfei. You have undoubtedly been one of my greatest support throughout these four years. We embarked on this adventure together, enjoyed it together, and we will see it through to the end together. You were always there for me, during the challenging times, as well as the joyful moments. Mauro, thank you for all the drinking games and life-saving water bottles at De Gudde Wëllen at 2 a.m. I extend my appreciation to my FMT tennis buddies, Youri and Alvar. Our matches and the fun we had during the courses are cherished memories. I would also like to express my gratitude to Cosme, Naveen, Hugo, Mónica, Andreas, Barnik, Georgy, Christina, Juliette, Constance, Veronika, Pierre, John, Ashwath, Natalya, Nicolas, Sangita, Paola, Sam, Marco, Uros, Misbah, Pranab, and many others who have played a part in my journey. Thank you for having made this period of life so much more memorable.

I would also like to express my gratitude to all the colleagues I had the pleasure of meeting at conferences and during my travels throughout these years. In particular, I would like to thank the Laboratory for Multifunctional Ferroic Materials, who made my stay in Zürich an incredibly joyful experience. Morgan, Ipek, Martin, Alex, Gerrit, and many others, thank you for the engaging discussions and enriching interactions. I also would like to thank Tony. It was a coincidence to discover that we were both working on the bulk photovoltaic effect. Your theoretical insights helped me to gain a better understanding of the shift current theory. Thank you for all the mind-blowing conversations.

I also want to thank my high-school friends: Pilar, Alberto, Álvaro, Iván, Julia, Lucia, Marcos, and Rocio. As I write this paragraph on my way to my 9^{th} trip to Cabopino (Málaga), I reflect on the fact that you have been there for me during both the most challenging and the most joyous moments. In a world where everything around us constantly changes as we grow, we often find happiness in the constants that remain. That is precisely what our friend group represents to me: the time-travel ticket to the years when traveling, partying, and losing the key to the beach house with all the phones inside was our biggest problem. Thank you for always being there.

Thank you to my girlfriend, Valeryia, for all your love and support. You are my family in Luxembourg. Thank you for all the dates, movie nights, and weekend trips during the last few years. You always pushed me to improve, be better and do my best. I will never forget those weekends in Würzburg, those coffee breaks at Golden Bean, and those sports sessions that kept me alive by the end of this thesis. I owe you a thousand pizzas. I would also like to thank Tatjana, Jos, and Ellie for the wonderful spaghetti bolognese nights.

Most importantly, none of this could have happened without my family. My parents offered their unwavering support throughout my entire educational journey. I vividly remember the evenings when they dedicated their time to help me with my school homework, especially when I struggled with primary school. I managed to "give fuel to the monkey and the trapeze" after all. They taught me the importance of consistency and constantly pushing myself. My brother, Alvarito, the last words of this text are for you. You cannot imagine how proud I am of having you. Thank you for being my biggest support.

Abstract

Photoferroelectrics effects include a variety of properties observed in materials exhibiting both ferroelectric and photoresponsive properties. Some examples of these effects include the bulk photovoltaic effect, photostriction, and photorefraction. These effects display a potential for light-driven applications, such as light-induced ferroelectric switching, light-driven actuators, or holographic data storage.

Bismuth ferrite ($BiFeO_3$) is a prototypical photoferrolectric material due to its high remanent ferroelectric polarization and relatively narrow bandgap. In addition, the high-temperature stability of the ferroelectric phase and high birefringence make $BiFeO_3$ an interesting candidate for electro-optic modulation. The bulk photovoltaic and electro-optic properties, combined with the large dark conductivity of $BiFeO_3$, could make it suitable for transient photorefractive applications, such as reconfigurable waveguides.

Consequently, this thesis reports on the synthesis and photoferroelectric properties of polycrystalline $BiFeO_3$ films fabricated using solution-deposition methods. High-quality polycrystalline $BiFeO_3$ films were grown by precise doping and control of the microstructure using seeding strategies. The photovoltaic properties were measured, showing that the bulk photovoltaic effect is the main light-induced charge transport mechanism at zero fields. The influence of stress and doping on the bulk photovoltaic properties was studied. Additionally, the electro-optic properties were measured using a modified Teng-Man set-up. Larger Pockels coefficients were measured in films under compressive stress. A drastic enhancement of the electro-optic response is achieved by combining the Pockels effect and transient ferroelectric switching contributions. The results discussed in this thesis highlight the potential of low-cost polycrystalline $BiFeO_3$ films for light-driven applications.

Table of Contents

Abbreviations and notations

α	Absorption coefficient
β	Bulk photovoltaic tensor
V_{OC}	Open-circuit photovoltage
σ_0	Attempt conductivity
σ_{DC}	Frequency-independent conductivity
σ_d	Dark conductivity
σ_{ph}	Photoconductivity
E_a	Activation energy
E_{ph}	Photoinduced electric field
j_{SC}	Short-circuit photocurrent density
k_B	Boltzmann's constant
r	Electro-optic coefficient
AFM	Atomic Force Microscopy
BPV	Bulk photovoltaic
CSD	Chemical Solution Deposition
DF	Dark Field
E_C	Conduction band energy level

E_F	Fermi energy level
E_V	Valence band energy level
EO	Electro-Optic
FTO	F:SnO_2
IDE	Interdigitated Electrodes
LF	Lotgering Factor
MePro	1-methoxy-2-propanol
MIM	Metal-insulator-metal
MOE	2-methoxyethanol
n	Refractive index
PFM	Piezoresponse Force Microscopy
PV	Photovoltaic
SAED	Selected Area Electron Diffraction
SEM	Scanning electron microscopy
SIMS	Secondary ion mass spectrometry
TEC	Thermal Expansion Coefficient
TEM	Transmission electron microscopy
TM	Teng-Man
XRD	X-ray diffraction

List of Figures

List of Tables

Chapter 1

Introduction

Ferroelectric materials exhibit a spontaneous electrical polarization that can be reversed by applying an external electric field. They belong to the category of noncentrosymmetric materials, meaning they lack inversion symmetry.[1] The lack of inversion symmetry gives rise to unique photoinduced properties, including the photorefractive effect and the bulk photovoltaic effect.[2, 3] While these photoinduced effects exist in all noncentrosymmetric materials, attention is often focused on ferroelectrics because they offer the ability to control and modify these effects by altering the direction of electrical polarization. As a result, these effects are classified as photoferroelectric effects.[4]

The recent resurgence of interest in photoferroelectrics has primarily focused on the bulk photovoltaic effect. Although the bulk photovoltaic effect, arising from the noncentrosymmetric structure of ferroelectrics, was extensively studied in the 1970s, it has remained an academic curiosity due to its low efficiency.[2] However, recent reports have suggested that ferroelectric materials could play an important role in solar energy harvesting applications.[5] It has been proposed that the involvement of non-thermalized carriers in charge carrier separation could potentially circumvent the thermalization losses inherent in classical solar cells.[6] Nonetheless, both theoretical calculations and experimental results indicate that the microscopic mechanisms responsible for the bulk photovoltaic effect are orders of magnitude less efficient than classical p-n junctions. The photon conversion efficiencies achieved with the bulk photovoltaic effect typically remain on the order of 10^{-5}.[7, 8]

Consequently, efficiency should not be the primary research objective of studies on the bulk photovoltaic effect.[8, 9] The focus should be placed on the generation of extremely large switchable photovoltages.[10] It has been reported that photovoltages larger than 1000 V can be achieved when the bulk photovoltaic effect is the main charge-carrier separation mechanism.[11] In classical semiconductor solar cells, the pho-

tovoltage is limited by the quasi-Fermi energy level splitting, which cannot exceed the material's bandgap. In contrast, ferroelectrics exhibit exceptionally large photovoltages that have the potential for photoinduced effects: uniform illumination creates a large electric field, which in turn leads to light-induced functionalities.

A good example of light-induced functionality is photostriction, where the photoinduced electric field leads to mechanical deformation through the converse piezoelectric effect.[12–14] Another interesting functionality that can be triggered by photoinduced electric fields is the Pockels effect, i.e., change of the refractive indices in a noncentrosymmetric material under an electric field. The refractive index change under illumination is known as photorefraction. This effect has been studied for applications such as reconfigurable waveguides,[15] holographic data storage,[16, 17] or all-optical computing.[18, 19]

Since 2009,[20] the model photoferroelectric material is $BiFeO_3$.[5] A switchable photocurrent in ferroelectric $BiFeO_3$ was first reported in single crystals.[20, 21] Since this discovery, it has been the focus of most research on ferroelectric photovoltaics, owing to its relatively narrow bandgap of 2.7 eV[22] and high remanent polarization along the $[111]_{pc}$ direction.[22, 23] In addition, $BiFeO_3$ also exhibits antiferromagnetic order and it has been shown that magnetoelectric switching can be triggered.[24] This shows the potential of achieving remote magnetoelectric switching using light.

Despite the strong focus in recent years on the photoferroelectric properties of ferroelectric films, particularly their bulk photovoltaic effect and the linear electro-optic effect, all the studies are focused only on epitaxial single-crystal films. Until now, there are no reports on polycrystalline $BiFeO_3$ films, which are more interesting for practical applications. The main reason behind this is the challenge of obtaining low-cost solution-processed films with excellent ferroelectric properties and low leakage. Therefore, this thesis aims to answer the following research questions:

- **Solution processing of $BiFeO_3$:** Can an economic solution-based process for the fabrication of low leakage polycrystalline $BiFeO_3$ films be developed? What is the influence of doping on the ferroelectric and electrical properties of the films? Can ferroelectric properties rivaling those of epitaxial films be achieved?

- **Photovoltaic effect of $BiFeO_3$:** What is the origin of the photovoltaic effect in polycrystalline $BiFeO_3$? If the bulk photovoltaic effect is the main mechanism: what bulk photovoltaic tensors can be reached? What is the influence of doping and ferroelectric domain configuration on the bulk photovoltaic tensors? Do $BiFeO_3$ films show an intrinsic "piezophotovoltaic" effect, as observed in $LiNbO_3$ single crystals?[25] Under which substrate-induced stress conditions can optimum properties be reached?

- **Electro-optic properties of $BiFeO_3$:** What linear electro-optic coefficients can be reached? What is the influence of substrate-induced stress and ferroelectric domain configuration on the linear electro-optic properties? How do these factors depend on processing and poling conditions? Can larger electro-optic coefficients be achieved through ferroelectric domain reconfiguration? Under which conditions can optimum properties be realized? What is the potential of $BiFeO_3$ for photorefractive applications?

To answers these questions, the following thesis is structured into seven chapters. While **Chapter 1** serves as an introduction to the thesis, **Chapter 2** covers the necessary scientific background related to ferroelectricity, the bulk photovoltaic effect, the electro-optic effect, and the material that is used in this thesis. **Chapter 3** introduces the experimental methods utilized in this thesis. The methods used for the synthesis and basic characterization of $BiFeO_3$ are detailed. A strong emphasis is placed on the electrical, optical, and electro-optic characterization of the films, which are the core experimental techniques of this thesis.

In **Chapter 4**, the characterization of polycrystalline $BiFeO_3$ thin films fabricated using solution-deposition methods is discussed. The properties of films fabricated using various strategies are studied. The chapter focuses on the influence of seed layers on the film's texture, the influence of cation substitution on the charge transport properties, and the impact of various electrode configurations on the functional properties. These strategies result in $BiFeO_3$ films with excellent ferroelectric properties.

Having established a process for the growth of high-quality polycrystalline $BiFeO_3$ films, the focus now turns to the physical investigations. In **Chapter 5**, the photovoltaic effect of a polycrystalline ferroelectric is studied. It is demonstrated that the bulk photovoltaic effect dominates the light-induced charge transport in polycrystalline $BiFeO_3$ films with interdigitated electrodes. Measurements of the bulk photovoltaic tensors are carried out and compared with the values reported in the literature for epitaxial films. The chapter discusses the influence of doping and substrate-induced stress on the bulk photovoltaic properties.

In **Chapter 6**, the linear electro-optic properties of polycrystalline $BiFeO_3$ films with interdigitated electrodes are measured using a Teng-Man set-up built in-house. The influence of substrate-induced stress, as well as the use of transient domain switching to enhance the electro-optic response, is discussed. **Chapter 7** summarizes the results of the doctoral dissertation and provides an outlook for future work.

Chapter 2

Fundamentals

In this chapter, the fundamentals of the photoferroelectric properties investigated in the thesis are discussed. The chapter begins with an overview of ferroelectricity, covering its basic principles and characteristics. Following that, the photovoltaic effects observed in ferroelectric materials are discussed. Subsequently, the linear electro-optic (EO) effect is described. Finally, the fundamental aspects of the system under investigation, namely solution-processed $BiFeO_3$, are presented in detail.

2.1 Ferroelectricity

Ferroelectric crystals display a spontaneous polarization in a given crystallographic direction whose sign can be reversed when a sufficiently strong electric field is applied.[1] The discovery of ferroelectricity is often attributed to Valasek, who observed a switchable spontaneous polarization $\overrightarrow{P}$ in Rochelle salt in 1920.[26] Ferroelectric crystals undergo a structural phase transition from a high-symmetry non-polar paraelectric phase to a low-symmetry polar ferroelectric phase. This transition occurs at the Curie temperature (T_C), accompanied by a divergence of the susceptibility.[27]

The presence of a spontaneous ferroelectric polarization leads to the accumulation of bound charges at the surfaces. When these surface-bound charges are not effectively screened by external charge carriers (e.g. charged defects or metal electrodes) they create an electric field oriented opposite to the polarization referred to as the depolarization field.[28, 29] When a ferroelectric crystal is cooled from a paraelectric phase without an electric field, two or more orientation states become available. To minimize the electrostatic energy associated with the depolarization field and the elastic energy associated with the stress

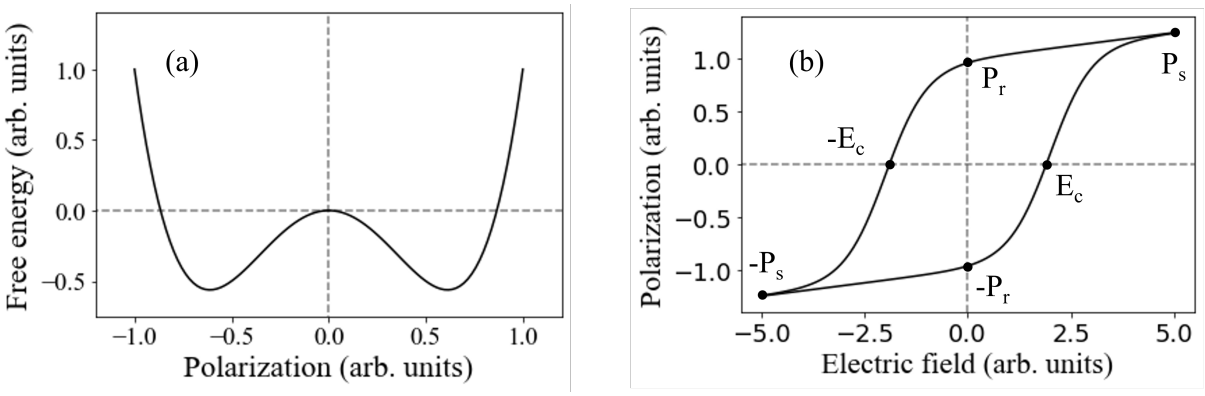

Figure 2.1: (a) The energy diagram illustrates the ferroelectric switching process between the two orientation states. (b) The polarization hysteresis loop depicts the behavior of the polarization as a function of the applied electric field in a ferroelectric material.

and clamping, different regions of the crystal polarize in different directions. These regions with identical polarization directions are known as ferroelectric domains, and the interfaces between domains with different polarization directions are referred to as domain walls.[30, 31]

These orientation states can be switched by an electric field $\overrightarrow{E}$. The energy change during ferroelectric switching between the two orientation states can be represented by a double-well energy landscape, as depicted in Figure 2.1 (a). When an electric field that is sufficiently high to overcome the energy barrier is applied to the ferroelectric crystal, the direction of the spontaneous ferroelectric polarization switches.

The measurement of ferroelectric hysteresis is commonly obtained by integrating the switching current when a triangular or sinusoidal electrical signal is applied.[32, 33] Figure 2.1 (b) illustrates a typical ferroelectric hysteresis loop. P_r denotes the remanent polarization, P_s represents the saturated polarization, and E_c corresponds to the coercive field.

Ferroelectric crystals possess significant dielectric and piezoelectric constants, making them highly appealing for various applications, including high-energy storage capacitors or actuators.[34] The electrical switching behavior of ferroelectrics is also utilized in the development of ferroelectric random access memories (FeRAM).[35] Additionally, the large non-linear polarizability of ferroelectric crystals makes them suitable for applications such as EO modulation[36] and second-harmonic generation.[3]

2.2 Photovoltaic effect in ferroelectric materials

The photovoltaic effect refers to the generation of a photovoltage and a photocurrent under illumination. It relies on the separation of photo-excited carriers. In conventional photovoltaic devices, at the interface between an n-type material with a p-type material, the greater chemical potential of the electrons in the

n-type material (and of the holes in the p-type material) drives a diffusion current. The diffusion currents continue until an electrical potential difference compensates for the gradient in chemical energy.[6] This effect will be referred to in the following as interface-driven photovoltaic (PV) effect. In ferroelectrics, in addition to the interface-driven PV effect, the separation of photo-excited carriers is driven by the lack of inversion symmetry, this is known as the bulk photovoltaic (BPV) effect.[2, 7] In this section, the basics of both, the interface-driven PV effect and the BPV effect will be described.

2.2.1 Interface-driven photovoltaic effect

In classical p-n junction solar cells, two semiconductor layers, a p-type and n-type, are brought together to form a junction. The difference in charge carrier concentration causes the movement of electrons from the n-type side to the p-type side, resulting in an exposed positive ion region on the n-type side. Similarly, the movement of holes from the p-type side to the n-type side exposes a negative ion region on the p-type side.[37] This arrangement creates an electrical potential difference that plays a crucial role in the separation of photo-generated charge carriers, such as electrons and holes when the solar cell is illuminated.[6]

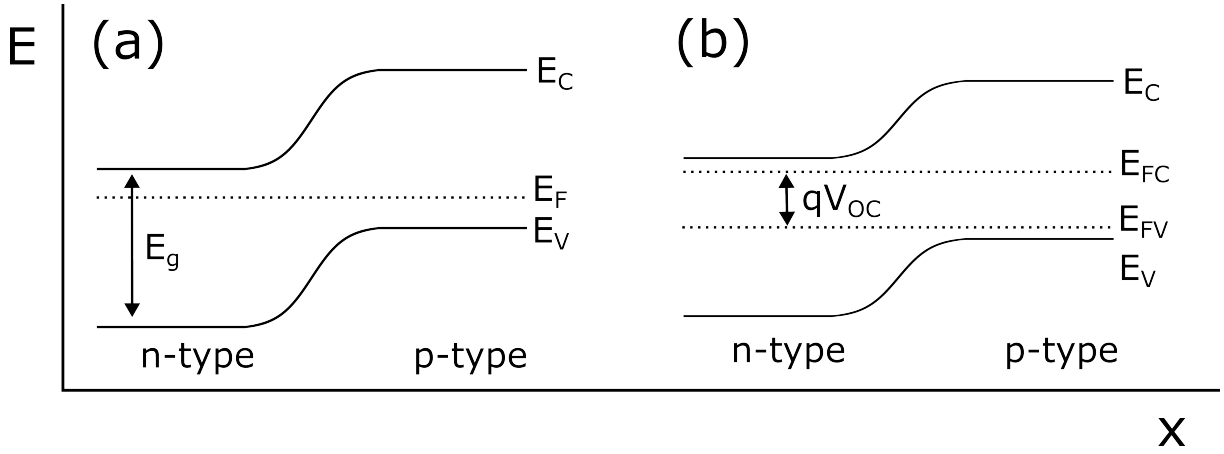

Figure 2.2: Schematic band diagram showing the potential distribution in a p-n junction. (a) In the dark in equilibrium (b) Under illumination in open-circuit conditions.

In thermal equilibrium, the Fermi levels (E_F) of electrons and holes align, as shown in Figure 2.2(a). Under illumination, electrons are excited from the valence band (E_V) to the conduction band (E_C) and electron-hole pairs are generated, causing the Fermi levels of electrons and holes to split, as depicted in Figure 2.2 (b). These shifted levels are known as the quasi-Fermi energy levels (E_{FV}, E_{FC}) and they represent the energy distribution function of the electrons in the conduction band (E_{FC}) and holes in the valence band (E_{FV}). The difference between these energy levels is referred to as quasi-Fermi energy level splitting. This splitting directly influences the open-circuit voltage of the p-n junction solar cell.

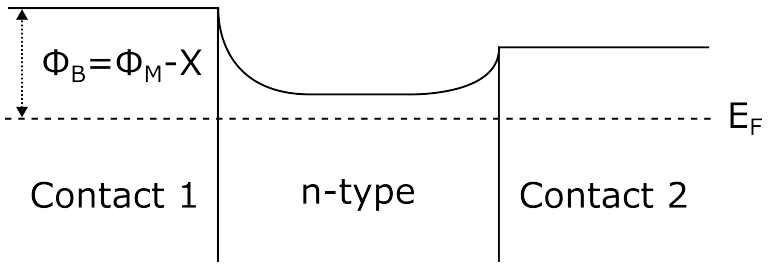

Figure 2.3: Schematic band diagram illustrating the potential distribution in a metal-n-type semiconductor-metal under equilibrium conditions.

In an ideal device, the upper limit of V_{OC} is determined by the rate of electron-hole production and recombination.[38] Following the Shockley-Queisser limit,[39] which describes the limits of photovoltaic energy conversion based on the thermodynamic principle of detailed balance, the maximum value of V_{OC} in classical p-n junction solar cells is determined by the material's bandgap.

A similar band-bending process occurs in homogeneous materials with dissimilar metal-semiconductor interfaces.[6] The energy difference between the Fermi level of the metal and the conduction band of the ferroelectric semiconductor creates a potential difference, enabling the separation of charge carriers and the generation of photovoltages. Adhering to the same thermodynamic limitations, the upper limit of the V_{OC} in a Schottky diode is also constrained by the bandgap of the ferroelectric material. As a first approximation, the barrier between a metal and a semiconductor is determined by the Schottky–Mott rule,[40] which states that it is proportional to the difference between the metal-vacuum work function (Φ_b) and the semiconductor-vacuum electron affinity (χ):

$$\Phi_B = \Phi_M - \chi \tag{2.1}$$

Fully symmetric Schottky interfaces in a metal-insulator-metal structure are unable to induce net light-induced charge transport. Nevertheless, modifying the charge carrier concentration in one interface can alter the electron affinity of the semiconductor, resulting in asymmetric Schottky interfaces.[41, 42] Figure 2.3 illustrates an example of the conduction band in a metal-n-type semiconductor-metal configuration, demonstrating asymmetric Schottky interfaces.

For example, in ferroelectric oxide perovskites[43] the barrier height can be tuned by modifying the donor or acceptor doping concentration at the interface. This can be achieved by applying a high DC voltage to the ferroelectric material, leading to the electromigration of oxygen vacancies, which drives positive

charges to one of the interfaces.[21, 41] The accumulation of oxygen vacancies induces a heavily doped layer, resulting in the formation of asymmetric Schottky interfaces or even Schottky-to-Ohmic interfaces. Furthermore, the height of the Schottky barrier can be modulated by the ferroelectric polarization.[20]

The influence of the electrode work function on the barrier height of out-of-plane ferroelectric capacitors was systematically investigated by You et al.[44] Their study demonstrates that the metal work function is not the primary parameter determining the barrier height responsible for the photovoltaic effect. Instead, the oxidation free energy of the metal contact plays a crucial role. Metals with higher oxidation free energy act as a reducing agent at the surface of the ferroelectric, thereby reducing the energy barrier.

Obtaining perfectly symmetric metal-ferroelectric-metal devices, where the top and bottom interfaces are identical, is challenging. For instance, the high temperatures utilized in the fabrication of perovskite oxides lead to the creation of additional oxygen vacancies at the top interface of the film. Consequently, this results in an unavoidable interface-driven photovoltaic effect when studying the electrical properties of out-of-plane thin film capacitors.

Current-voltage characteristics of interface-driven photovoltaic effect

Devices, where the charge transport is dominated by interface-driven photovoltaic effect, are characterized by the formation of asymmetric j-V curves that show rectifying behavior. In the simplest case, according to the thermionic-emission theory, if a single Schottky diode is formed, the current flows according to:[37]

$$j = AT^2 \exp\left(-\frac{q\phi_B}{k_B T}\right)\left[\exp\left(\frac{qV}{k_B T}\right) - 1\right] \tag{2.2}$$

where A is the Richardson constant, T the diode temperature, q the electronic charge, ϕ_B the barrier height, k_B the Boltzmann constant and V the applied bias.

In an ideal case, where a single Schottky diode is formed, the j-V curves display the characteristic rectification behavior. As shown in Figure 2.4 (a) at forward bias, the conductivity of the diode increases, while at reverse bias the conductivity of the Schottky diode decreases. Under illumination, as shown in Figure 2.4 (b) the j-V curve shifts as the Schottky diode begins to generate power.

Nevertheless, in most metal-ferroelectric-metal devices, both contacts have a rectifying nature and are commonly asymmetric. The different chemistry at the interface and local defects modifies ϕ_B. Despite the opposite polarity of the diodes, the different ϕ_B leads to a net photovoltaic current. In these situations, a more sophisticated description of the charge transport, considering two-diode models with different ϕ_B and ideality factors is needed to understand the charge transport properties of the device.[45]

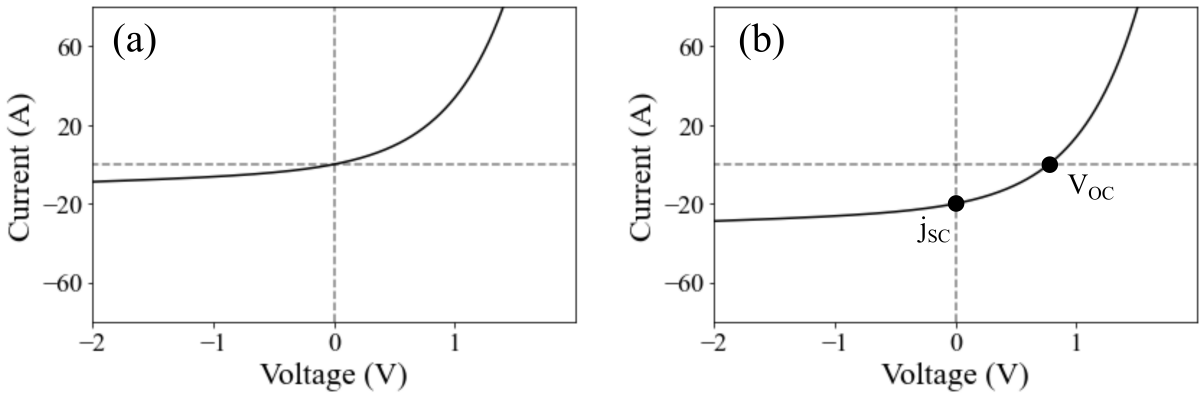

Figure 2.4: Simulated j–V plots of a single Schottky diode at forward and reverse bias in the (a) dark and (b) under illumination.

Some unique aspects must come together when a photocurrent in a ferroelectric is dominated by an interface-based PV effect:

- Non-linear j-V curves, arising from the presence of asymmetry Schottky diodes.
- V_{OC} is lower than the bandgap and increases logarithmically with light intensity, saturating at the bandgap of the material.
- The direction of photocurrent is not symmetrically switched after reversed poling.

Consequently, a careful analysis of the j-V characteristics and the dependency on light intensity is key to neglecting or confirming that the light-induced charge transport is driven by the interface-based PV effect.

2.2.2 The bulk photovoltaic effect

When a crystal is homogeneously illuminated with an electromagnetic wave with an electric field amplitude of:

$$\tilde{\mathbf{E}}(t) = \mathbf{E}(\omega)e^{-i\omega t} + \mathbf{E}(-\omega)e^{i\omega t} \tag{2.3}$$

a second-order response to the incident electromagnetic wave can be generated:

$$\tilde{E}^a(t)\tilde{E}^b(t) = E^a(\omega)E^b(\omega)e^{-i2\omega t} + E^a(-\omega)E^b(-\omega)e^{i2\omega t} + E^a(\omega)E^b(-\omega) + E^a(-\omega)E^b(\omega) \tag{2.4}$$

where a and b correspond to different electric field components. the first two terms correspond to a contribution at $2w$, which can lead to light generation at the second-harmonics frequency. The last two terms, however, do not pertain to the generation of electromagnetic radiation, as their second time derivative cancels out. Instead, these terms contribute to the generation of a DC component within the crystal.[3] It is noted that such second-order response is non-zero only in noncentrosymmetric crystals, in which the second-order susceptibility $\chi^{(2)}$ is nonzero.[46]

Consequently, upon illumination of a noncentrosymmetric crystal, a photocurrent, and a photovoltage can be measured. These are not produced by any crystal inhomogeneities, such as the photovoltaic effect in p-n junctions,[6] nor by nonuniform illumination, referred to as the Dember effect.[47] Rather, they arise from the symmetry breaking within the crystal. This effect exhibits two characteristic features: the magnitude of the photocurrent depends on the orientation of the light electric field relative to the crystal symmetry, and the photovoltage within the crystal can reach several thousand volts.[2, 4, 7]

The first observation of a BPV current in a noncentrosymmetric crystal is attributed to A. G. Chynoweth in 1956.[48] In his work, a steady photocurrent was observed in $BaTiO_3$ upon illumination. However, it was not until the 1970s that the BPV effect in crystals of practical importance, such as $BaTiO_3$[49] and $LiNbO_3$[18] was extensively studied and firmly established. Glass et al.[18] observed stationary photocurrents in $LiNbO_3$ single crystals that exhibited a linear increase with light intensity. Fridkin et al. reported the observation of anomalously large photovoltages of the order of 1000 V.[11] Additionally, their experiments suggest that the BPV effect, in combination with the EO effect, is one of the origins of photorefraction.

The BPV effect has been measured in numerous crystals, demonstrating its presence in all noncentrosymmetric crystal classes.[18, 49–51] All piezoelectric crystals exhibit the BPV effect. Interestingly, there are only a few reports on the BPV effect of polycrystalline ferroelectrics. While there is no basic physical principle that prohibits BPV-induced charge transport in poled polycrystalline systems, its observation is not guaranteed. Factors such as incomplete poling of the ceramic or scattering of hot charge carriers at grain boundaries may reduce the BPV effect below the detection limit. Examples in the literature are limited to P(L)ZT and $BaTiO_3$ bulk ceramics.[52–55]

Phenomenological description

The phenomenological description of the BPV effect was developed in the 1970s by Fridkin, Belinicher, Sturman, Ivchenko, and Pikus.[2, 56–58] It represents the most comprehensive approach for describing the photovoltaic effect and it is the description used in this thesis. The induced current density in a material under homogeneous illumination can be described as follows:

$$j_j = \sigma^d_{jk} E_j + I\sigma^{ph}_{jkl} E_j e_k {e_l}^* + I\beta^L_{jkl} e_k {e_l}^* + iI\beta^C_{jl}[e{e}^*]_l \tag{2.5}$$

where σ^d_{jk} represents the dark conductivity, I is the light intensity, σ^{ph}_{jklm} corresponds to the photoconductivity, e_k and e^*_l denote the light electric field unit vectors, β^L_{jkl} denotes the third-rank linear BPV tensor and β^C_{jl} represents the second-rank circular BPV tensor. (Here, e^* refers to the complex conjugate of the light electric field). The BPV tensor exhibits non-zero values only in noncentrosymmetric crystals. Out of the 32 point symmetry classes, 21 are noncentrosymmetric, including all piezoelectric crystals.

Noncentrosymmetric crystals can be divided into three groups.[2] Group I comprises systems that display piezoelectric and gyrotropic behavior, where the polarization direction of light rotates as it propagates through the crystal. This group exhibits both non-zero β^L_{jkl} and β^C_{jl}. The following point symmetry classes, according to the Hermann–Mauguin notation, are included in this group: 1, m, 2, 3, 4, $\bar{4}$, 6, 312, 23, 222, 422, 622, mm2, $\bar{4}$2m, 4mm, 3m, 6mm. Group II consists of piezoelectrics that do not exhibit optical activity. In this group $\beta^{\mathrm{L}}_{\mathrm{jkl}} \neq 0$, while $\beta^{\mathrm{C}}_{\mathrm{jl}} = 0$. The corresponding point symmetry classes are: $\bar{6}$m2, $\bar{6}$ and $\bar{4}3m$. Group III consists of non-piezoelectric crystals that exhibit optical activity. In this group, $\beta^{\mathrm{L}}_{\mathrm{jkl}} = 0$, but $\beta^{\mathrm{C}}_{\mathrm{jl}} \neq 0$. This group corresponds to class 432. When the crystal's symmetry is known, the non-zero independent components of β^L_{jkl} and β^C_{jl} can be determined. These tensors describe the dependence of the BPV effect on light polarization and intensity.

Historically, the BPV effect was first measured in ferroelectric materials, where photocurrents were observed along the polar $\vec{c}$ axis. Additionally, the direction of the photocurrent in these materials can be switched by changing the direction of the polar axis. In these studies, the dependence of the photocurrent on light intensity and polarization is often described using the glass coefficients (G).

$$j_j = I\alpha G^L_{jkl} e_k {e_l}^* \tag{2.6}$$

where α represents the absorption coefficient and G_{jkl} denotes the Glass tensor, which characterizes the current excitation performance. However, in recent literature β_{jkl} is commonly used to compare the photovoltaic response of different systems. The movement of non-equilibrium carriers builds up a photovoltage. Under open-circuit conditions, the steady-state open-circuit photovoltage (V_{OC}) can be expressed as follows:

$$V_{OC} = \frac{j_{SC}}{\sigma^d + \sigma^{ph}} l \tag{2.7}$$

where l represents the spacing between the electrodes. From equation 2.7, it can be observed that V_{OC} increases with the distance between the electrodes. In fact, remarkably large photovoltages can be achieved when the electrodes are significantly separated. Therefore, when comparing materials, it is more meaningful to compare the steady-state photoinduced electric fields (E_{ph}).

To prove that a photocurrent in a ferroelectric is of BPV nature, four unique aspects must come together:

- The direction of j_{SC} can be modified by reversing the ferroelectric polarization. If the BPV effect is the only mechanism for the current generation, the reversal must be symmetric.
- j_{SC} must increase with light intensity. Besides, when $\sigma^{ph} \gg \sigma^{d}$, both j_{SC} and σ^{ph} increase linearly with light intensity. In this situation, E_{ph} is independent of the light intensity.
- V_{OC} must show a linear dependence on the electrode distance.
- j_{SC} must be dependent on the direction of the light electric field.

These aspects can occur independently in systems with interface-dominated PV effects. For example, as demonstrated in the previous section, a switchable photovoltaic effect can be observed due to either the electromigration of n-type defects or the polarization-mediated modulation of the Schottky energy barrier height. Therefore, all four aspects must be present to attribute the charge transport mechanism to a BPV effect.

Microscopic description

The microscopic description of the BPV effect in the steady state under linearly polarized light is based on the time-dependent perturbation theory.[46, 59] It stems from the frequency-independent term of the second-order response of a noncentrosymmetric material under illumination as shown in Equation 2.4. To develop a microscopic theory, one is interested in how the equilibrium density matrix of the system under study will evolve under the perturbation from light. The steady-state current can be computed as:[46]

$$j = \sum_{nm} \rho^{I}_{nm} \nu^{I}_{mn} \tag{2.8}$$

where ρ^{I}_{nm} is the steady-state density matrix under continuous illumination and ν^{I}_{mn} is the velocity operator. ρ^{I}_{nm} can be calculated using perturbation theory for the electric field. Consequently, after a certain amount of algebra, the steady state photocurrent can be explicitly written as:[46]

$$j = \frac{\pi e^3}{\omega^2} Re \left[\sum_{l,m,n} \sum_{\Omega=\pm\omega} \int_{BZ} \frac{dk}{(2\pi)^3} (f_{lk} - f_{nk}) \times \frac{\nu^r_{nl}(k)\nu^s_{lm}(k)\nu^q_{mn}(k)}{(\epsilon_{nk} - \epsilon_{mk} - i\eta)(\epsilon_{nk} - \epsilon_{lk} - \hbar\Omega - i\eta)} \right] E_r E_s \quad (2.9)$$

where l, m, n refer to the single-particle eigenstates of the crystal, e is the electron charge, ω is the light wavelength, k refers to the crystal momentum, f_{lk} is the Fermi-Dirac distribution function, $\nu^r_{nl}(k)$ are the matrix elements of the velocity operator and ϵ is the energy of the corresponding single-particle eigenstates of the crystal. Equation 2.9 is the central result for the BPV effect theory as it expresses the steady-state current response tensor with quantities that can be obtained from numerical models such as quadratic band structure models, tight binding models, or from first-principles calculations. To simplify equation 2.9, two different contributions are considered: the ballistic and shift contribution.[58]

In the ballistic contribution, an asymmetric distribution of hot carrier momenta in the band and a violation of the principle of detailed balance occur due to the excitation of nonthermalized carriers in a noncentrosymmetric crystal. This contribution stems from the diagonal terms of the density matrix, ρ^I_{nm}, where $n = m$, commonly referred to as two-band contribution.[46]

The shift current contribution arises from the excitation of electrons into coherent superpositions, allowing for net current flow due to the potential asymmetry. This contribution arises from the non-diagonal terms of the density matrix, where $n \neq m$.[60–63]

These two contributions were experimentally distinguished for the first time by Burger et al.[64] in $Bi_{12}GeO_{20}$ crystals. In their work, they assumed that the shift current is less susceptible to magnetic field whereas the ballistic current can give rise to a Hall current as any classical charge current. Nevertheless, their results demonstrate that under monochromatic light, the photocurrents exhibit opposite directions, but similar magnitudes.

Based on this microscopic description, recent calculations indicate that the efficiency of the BPV is below 10^{-5}.[7, 8] Only one report claims the measurement of power-conversion efficiencies exceeding the Schokley-Queisser limit in $BaTiO_3$ thin films using tip-enhanced BPV effect.[65] However, Kirk et al.[66] explained in their response letter to [65] that the power was obtained considering only the area of a scanning probe microscopy tip, not the real area of the device, as is the standard definition of power conversion efficiency. Therefore, the high power-conversion efficiency arises from an underestimation of the contact area, which is a challenging calculation when using scanning probe microscopy tips.[66]

Piezophotovoltaic effect

As explained in the previous sections, the BPV effect arises from symmetry breaking in the crystal. As a result, its magnitude is sensitive to perturbations in the crystal structure, such as temperature,[67] strain,[25, 68] or strain gradients.[69]

Recently, strain engineering has emerged as a powerful approach to modulating the BPV effect. Yang et al.[69] demonstrated that the application of a strain gradient to a centrosymmetric material leads to the appearance of a BPV-like effect referred to as the flexo-photovoltaic effect. In noncentrosymmetric perovskite oxides, Nadupalli et al.[25] showed that the BPV effect of $LiNbO_3$ single crystals can be enhanced by the application of a uniaxial compressive strain, known as the piezophotovoltaic effect.

This effect has also been extended to noncentrosymmetric 2D transition metal chalcogenides, both experimentally and theoretically,[70–72] demonstrating the potential of strain engineering in boosting the photovoltaic performance of noncentrosymmetric materials. However, this topic remains largely unexplored, and the existing examples in the literature are limited to epitaxial films or single crystals.

The revival of ferroelectric photovoltaics

The research on the photovoltaic effect of ferroelectric materials received a significant boost with the discovery of a switchable photovoltaic effect in $BiFeO_3$.[20] However, the origin of the photovoltaic response was first found to be associated with the interface-driven PV effect.[21] It was observed that the effect exhibited a dependence on light polarization. Nevertheless, this dependency was attributed to anisotropic absorption coefficients rather than the dominance of a BPV effect. These initial findings highlighted the challenging task of distinguishing between interface-based photovoltaic effects and BPV effects, which are often erroneously categorized under the term "ferroelectric-based photovoltaics".

The separation of non-thermalized carriers in noncentrosymmetric materials is not associated with the thermalization losses of interface-based photovoltaic effects, offering the potential to achieve efficiencies surpassing the Shockley-Queisser limit.[38, 39] This promise sparked a notable increase in publications on photoferroelectrics in the last decade, as depicted in Figure 2.5.

However, it is important to note that every reported instance of high efficiency ($>$2%) in these materials has been attributed to the formation of Schottky barriers at the ferroelectric/metal interface, thereby being limited by the same mechanisms as classical p-n junctions.[73] It remains quite common in the research community to observe current-voltage behaviors that perfectly rectify, indicating the formation of diodes at the interface of ferroelectric materials, while simultaneously claiming the presence of a BPV effect.[74]

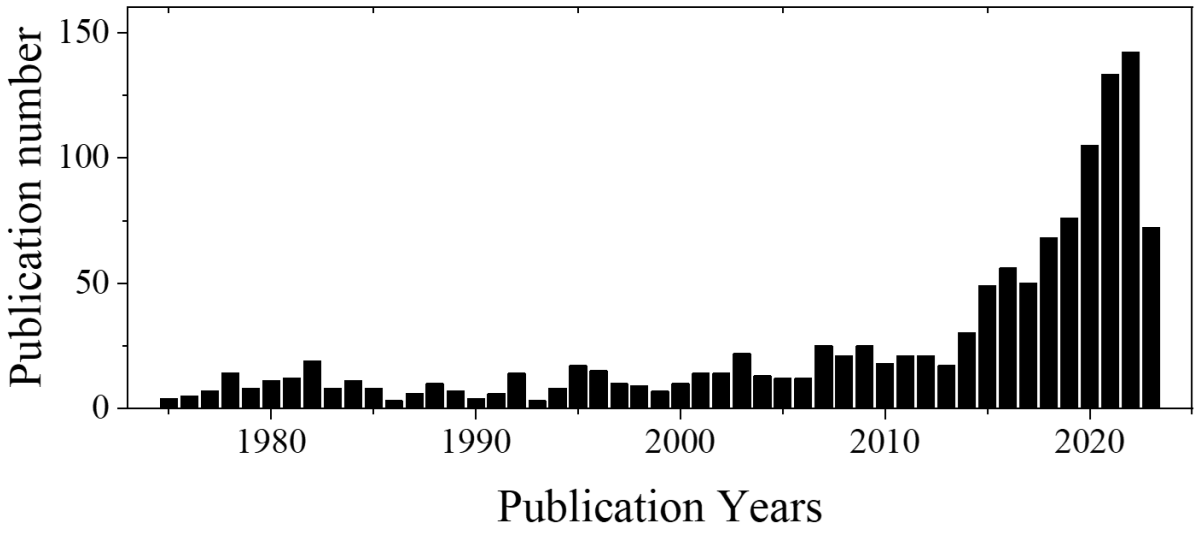

Figure 2.5: Evolution of the number of publications in Web of Science containing the terms ”photoferroelectric” or ”bulk photovoltaic effect” or ”photogalvanic effect” or ”ferroelectric photovoltaic” in the title or abstract.

As suggested by Kreisel et al.,[9] it is important to shift the focus towards exploring photoinduced effects in ferroelectrics. The unique property of the effect, which is the generation of large photovoltages under illumination, can be coupled to other effects.[75] In recent years, significant attention has been given to applications involving photostriction,[13, 76] light-induced switching of ferroelectric polarization,[77] and photo-catalysis.[78]

2.3 The electro-optic effect

The EO effect is based on the modification of the refractive index of a material upon the application of an electric field.[3] The modification of the refractive index (n_{ij}) under an electric field can be expressed as a power series as follows:

$$n_{ij} = n_{ij}^{(0)} + \sum_{k} r_{ijk} E_k + \sum_{kl} s_{ijkl} E_k E_l + ... \tag{2.10}$$

where r_{ijk} refers to the linear EO coefficient, a third-rank tensor, and s_{ijkl} refers to the quadratic EO coefficient, a fourth-rank tensor. For simplicity, since r_{ijk} is symmetric in its first two indices, it is usually represented as a two-dimensional matrix r_{hk}, e.g., $r_{111} \rightarrow r_{11}, r_{233} \rightarrow r_{43}, r_{231} \rightarrow r_{41}$. In noncentrosym-

metric materials, the odd-rank tensor components are non-zero, and the modification of the refractive index under an electric field is dominated by the first-order term. This change is known as linear EO or Pockels effect.

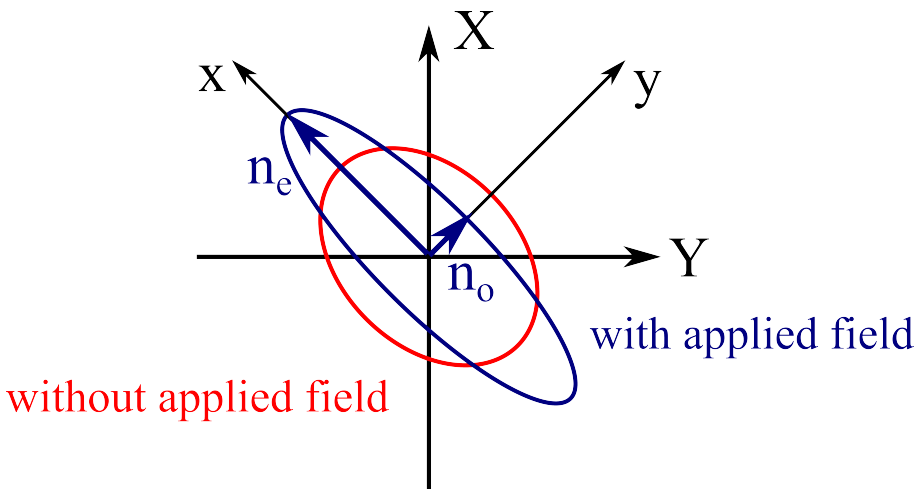

Figure 2.6: Schematic depicting the projection of the refractive index ellipsoid with and without the application of an electric field. In the current scenario, the refractive index ellipsoid undergoes a transition from slightly to highly anisotropic behavior along the [X,-Y] direction.

Following this notation, the lowest-order modification of the refractive index ellipsoid $(1/n^2)_i$ upon the application of an electric field (Figure 2.6) can be expressed as follows:

$$\Delta\left(\frac{1}{n^2}\right)_i = \sum_j r_{ij} E_j \tag{2.11}$$

The physical origin of the EO effect has been investigated using various methods, including first-principles calculations[79, 80] and less computationally intensive approaches like perturbation theory on model Hamiltonians.[81] This effect is attributed to the displacement of ions within the material under an electric field, leading to alterations in the band wave function of the lattice electrons.[82] By considering the bandgap, refractive index, and dielectric constant of the material,[83] the EO effect can be estimated. Nevertheless, it is important not to overlook the influence of the ferroelectric domain structure.[84]

The EO effect in non-ferroelectric piezoelectrics is generally characterized by low values, typically on the order of 1 pm V^{-1} in quartz at 1540 nm.[85] On the other hand, ferroelectric materials exhibit the largest EO coefficients, making them the primary candidates for studying and utilizing this effect.[86]

Among the various ferroelectric materials, $LiNbO_3$ stands out as the most relevant choice for bulk EO modulators due to its excellent optical properties and the ability to produce large, high-quality single crystals.[87] However, its EO coefficients are not particularly high at around 30 pm V^{-1} at 633 nm.[88] In comparison, EO coefficients of 1300 pm V^{-1} at 633 nm have been reported for $BaTiO_3$ single crystals in stress-free conditions,[89] but the properties of $BaTiO_3$ suffer from a strong temperature dependence.

Another alternative is the use of relaxor-lead titanate based ($PbTiO_3$) crystals, such as PIN-PMN-PT, which display giant EO coefficients around 900 pm V^{-1} at 1064 nm.[90] The origin of the high EO response in relaxor ferroelectrics is based on the ease of ferroelectric polarization rotation under an external electric field. Nevertheless, Pb-based ferroelectrics are subject to environmental restrictions and also display strong temperature dependence.[91]

In recent years, the focus has shifted to thin films, with a particular emphasis on integration with silicon technologies. Cubic Si displays a Pockels effect only under mechanical strain.[92] However, this mechanism is inefficient, slow, and lossy. Therefore, there is a strong trend to create integrated heterostructures combining ferroelectrics such as $BaTiO_3$ or PZT on Si.[93] The recent growth of ferroelectric materials such as $BaTiO_3$ on silicon with giant EO coefficients has spurred the research of ferroelectric thin films for integrated photonics.[94, 95]

A challenge that remains is to find an EO material with properties less sensitive to temperature, that is environmentally friendly and can be produced economically using a process compatible with Si technology.

2.4 Bismuth ferrite

$BiFeO_3$ is a rhombohedral multiferroic of perovskite structure type at room temperature.[96] It has the unique property of exhibiting both ferroelectric and antiferroelectric order. In the bulk, it has a Curie temperature of 810 °C and a Néel temperature of 370 °C.[97] In terms of its ferroelectric characteristics, remanent polarization values of 100 $\mu C\,cm^{-2}$ with coercive field E_C of 250 $kV\,cm^{-1}$ along the [111] direction have been reported in epitaxial $BiFeO_3$ thin films at room temperature deposited using vacuum technologies.[23, 98]

2.4.1 Basics of the chemical solution deposition of $BiFeO_3$ thin films

The preferred method for the growth of high-quality ferroelectric films for optical applications is direct epitaxial growth on single-crystal substrates.[99] Techniques such as pulsed laser deposition, molecular beam epitaxy, or off-axis sputtering enable precise control of growth at the atomic level, allowing for mon-

itoring unit cell by unit cell using reflection high-energy electron diffraction.[100, 101] This level of control ensures accurate manipulation of the interface chemistry. However, achieving high-quality growth using these techniques is typically limited to small areas, slow growth rates, and expensive vacuum conditions.

In contrast, chemical solution deposition (CSD) methods offer advantages for the growth of oxide perovskites in terms of larger area coverage, higher deposition rates, and lower cost. However, these advantages come at the expense of reduced control over the interface chemistry. Nonetheless, CSD is compatible with large-scale industrial production. [102]

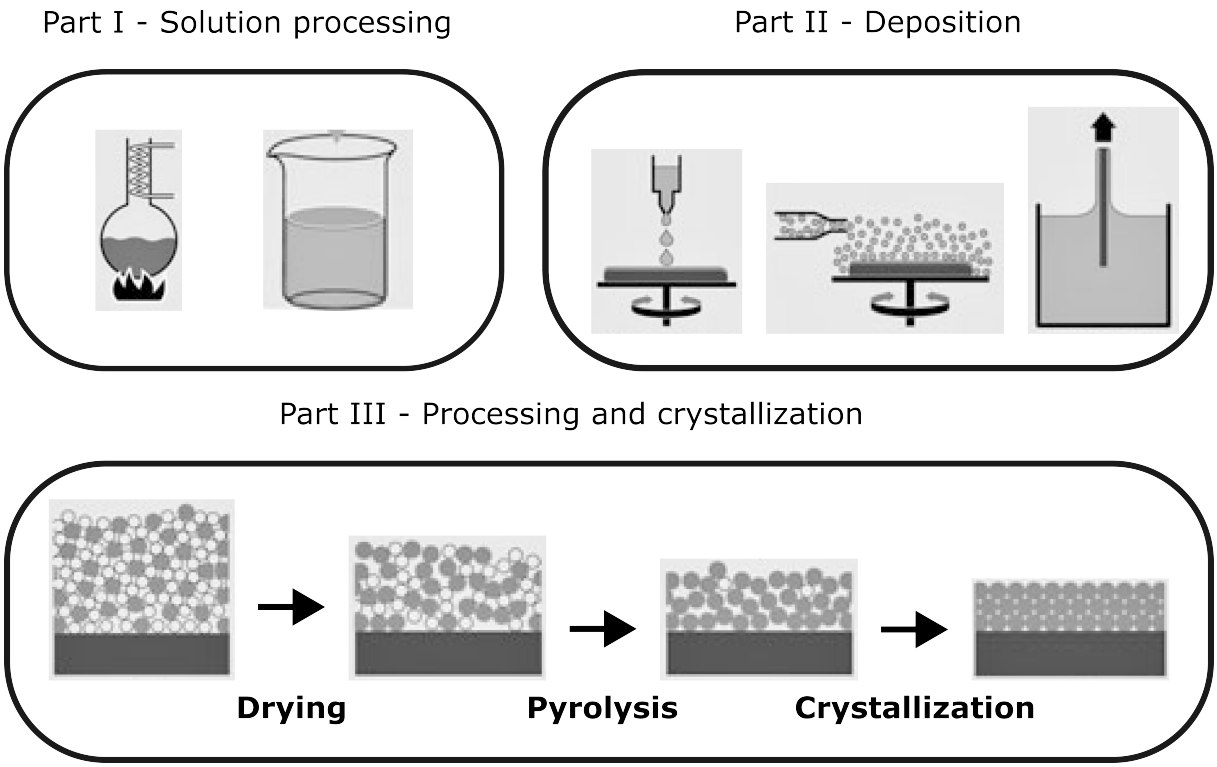

Figure 2.7: Schematic of the solution deposition process. Adapted from [103].

In solution deposition processes, a precursor solution is deposited and annealed to form a crystalline film. A schematic of this process is illustrated in Figure 2.7. During the initial step, metallic precursors such as metal nitrates, acetates, or alkoxides are dissolved into an organic solvent such as 2-methoxyethanol. Various drying agents can be employed to eliminate crystallization water, while complexing agents may be added to enhance the chemical homogeneity and stability of the solution.[104] It is crucial to consider the cation distribution within the solution's chemical composition, as it plays a vital role in producing high-quality films since it will be transferred to the final material.[105]

In the subsequent step, the precursor solution is deposited onto a substrate using one of various deposition techniques. For the purposes of this study, particular attention is given to the spin-coating technique.[106] In this technique, the solution is deposited onto the substrate, which is then rotated at a high speed, typically 3000 rpm, until a uniform film forms on the surface. Following this, a drying step is employed to facilitate the evaporation of the solvent. The result is a gel. Subsequently, a pyrolysis step is carried out to remove all organic compounds, resulting in the formation of an amorphous film. Finally, high-temperature annealing is performed to crystallize the amorphous film.

The fabrication of $BiFeO_3$ films with robust ferroelectric properties poses a significant challenge due to the high leakage current density observed in these films.[107, 108] The presence of intra-bandgap defects, such as reduced cation gap states (e.g., Fe^{2+} instead of Fe^{3+}), oxygen vacancies[109–112] or the formation of secondary phases, e.g., Bi_2O_3,[113–115] contribute to the high leakage current density by providing conductive paths within the capacitor. These defects are often a result of the high processing temperatures required for film fabrication, which can cause sublimation of Bi^{3+} ions.[116] As a consequence of these challenges, only a limited number of reports demonstrate robust ferroelectric properties at relatively low frequencies.

The main strategy to tune the charge transport mechanisms that are responsible for leakage is the use of doping to decrease charge carrier concentration or to modify the dominating charge transport mechanism. The introduction of a high-valent cation, such as Ti^{4+} (Ti'_{Fe}), has been shown to effectively decrease the concentration of oxygen vacancies.[117] Furthermore, both experimental and theoretical results suggest that isovalent dopants with partially or fully electron-filled e_g states, like Mn^{3+}, can act as traps for oxygen vacancies, thus impeding the electromigration of vacancies under electric fields.[118–120] Both Ti^{4+} (75 pm) and Mn^{3+} (78 pm) have a similar ionic radius to Fe^{3+} (63 pm) acting as B-site dopants in the lattice. In line with recent literature findings, this thesis adopts a precise co-doping approach with Mn^{3+} and Ti^{4+} to mitigate the issue of leakage currents.[121, 122]

2.4.2 The photovoltaic effect in $BiFeO_3$

The photovoltaic effect in $BiFeO_3$ single crystals was initially attributed to the formation of asymmetric Schottky interfaces between $BiFeO_3$ and the contacts.[20, 21] However, other studies have shown that $BiFeO_3$ single crystals exhibit a BPV effect.[123] The high concentration of oxygen vacancies is the main challenge in unveiling the mechanism responsible for the photovoltaic effect.

Measurements conducted on films with a high concentration of oxygen vacancies or asymmetric contacts exhibit electrical rectification characteristics, whereby the photovoltaic effect is primarily governed by the formation of Schottky barriers at the electrode interfaces rather than a BPV effect.[41, 73, 74, 125] During

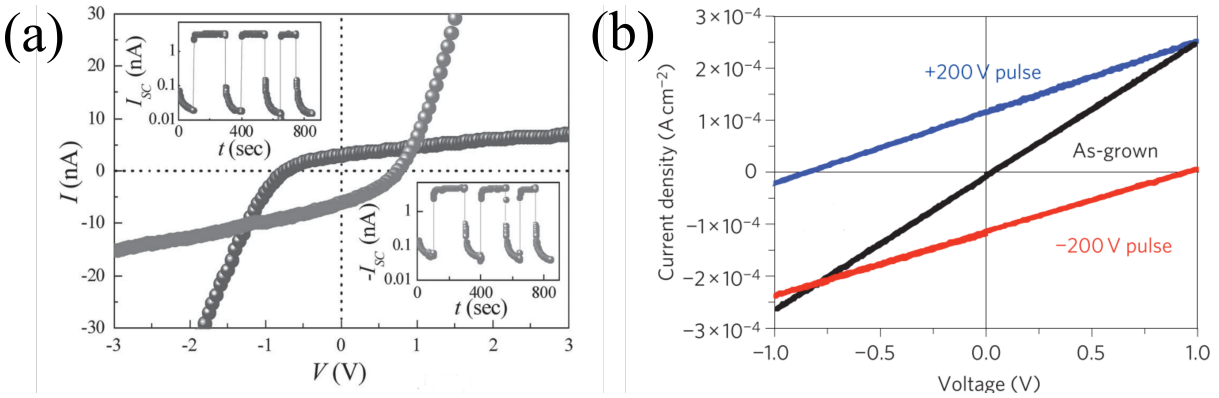

Figure 2.8: (a) Switchable photovoltaic effect in $BiFeO_3$ single crystals. The rectification behavior and the asymmetry of the j-V curves indicate that the mechanism is driven by the interface-based PV effect. The switchability of the effect arises from the changes in ϕ_B related to the electro-migration of defects and the ferroelectric polarization. Adapted from [21]. (b) Switchable photovoltaic effect in $BiFeO_3$ epitaxial films. The linear j-V curves, as well as the symmetry in the switchability of the effect, indicate the charge transport is dominated by the BPV effect. In the as-grown sample, the net polarization along the measuring direction is zero, resulting in a zero net current. After poling, a photocurrent can be measured. The change in the photoconductivity is related to changes in the domain structure during poling.[124] Adapted from [10].

electrical poling, the accumulation of defects at one interface modifies the Schottky barrier height, leading to asymmetric contacts responsible for the photovoltaic effect (Figure 2.8 (a)). In fact, it is common in the literature to find photovoltaic phenomena in $BiFeO_3$ films attributed to the BPV effect with no direct evidence.[74]

It is worth noting that the Schottky barrier-induced photovoltaic effects are usually neglected in devices with a co-planar electrode geometry, mainly due to the symmetric contacts.[10, 126] In contrast, the photovoltaic effect of out-of-plane thin film capacitors is commonly dominated by the interface-based photovoltaic effect, primarily because of the difficulties in achieving symmetric contacts.[44]

The PV effect in epitaxial $BiFeO_3$ co-planar capacitors resulted in a BPV light-induced charge transport (Figure 2.8 (b)). Initially, these were attributed to the separation of photo-generated carriers at the domain walls.[10] However, this theory did not explain the dependence of the photocurrent on light polarization or the generation of a net charge transport when a free electron generated at one domain wall recombines with the hole generated at the next domain wall. Subsequent studies in monodomain and domain-engineered structures have shown that the actual mechanism behind these anomalously large photovoltages is the BPV effect.[126–128] The strong dependence of the photovoltaic effect on the domain walls was associated with the intrinsic conductivity of the domain walls, which introduces a conductive

path that increases conductivity and lowers the open-circuit voltage.[126] Moreover, later studies have demonstrated that the BPV effect of $BiFeO_3$ can be tuned by engineering the sub-band levels through chemical doping with Mn^{3+} or Ti^{4+}.[128–130]

2.4.3 The electro-optic effect in $BiFeO_3$

$BiFeO_3$ has peculiar properties that make it interesting for EO applications. Contrary to other candidates for EO modulators, such as $BaTiO_3$ or $PbTiO_3$-based compounds, the high Curie temperature of $BiFeO_3$ allows for high-temperature applications. Indeed, not only its T_C is much higher than for $BaTiO_3$ or $PbTiO_3$-based compounds, but in addition, mode softening is much weaker due to the more complex nature of the ferroelectric transition in $BiFeO_3$.[131, 132] In addition to the intrinsic linear EO effect, the massive birefringence of $BiFeO_3$ of 0.15-0.31 allows for refractive index tuning by reorientation of the optical axis through ferroelectric domain switching.[133, 134]

Although the interaction of $BiFeO_3$ with light is widely studied, there are surprisingly few papers on its EO properties. In 5% Mn-doped $BiFeO_3$ grown by PLD on $SrTiO_3$, coefficients of $r_{33} = 4.4\,\mathrm{pm\,V^{-1}}$, $r_{13} = -6.4\,\mathrm{pm\,V^{-1}}$ and $r_{eff} = 12\,\mathrm{pm\,V^{-1}}$ have been measured, while Density Functional Theory (DFT) calculations predict $r_{13} = 3.16\,\mathrm{pm\,V^{-1}}$ and $r_{33} = 14.75\,\mathrm{pm\,V^{-1}}$.[134] The disagreement between measured and calculated values was associated with the effect of the epitaxial mechanical constraints imposed experimentally on the thin films. Higher coefficients up to $r_{eff} = 19.3\,\mathrm{pm\,V^{-1}}$ were observed in $BiFeO_3$ films grown on $SrTiO_3$ by magnetron sputtering.[135] It is not known if good EO properties can be obtained in films produced by more economical methods such as solution deposition, or how a variation of domain orientation, in combination with the high birefringence, can be utilized for refractive index modulation.

Chapter 3

Experimental methods

In this chapter, the main experimental methods used in the thesis will be detailed. The chapter will be divided into three sections:

1. a section dedicated to the synthesis of solution-processed $BiFeO_3$ thin films, the microfabrication of devices, and the structural characterization of the thin films;
2. another section will be dedicated to the electrical characterization of thin films. Several techniques such as dielectric spectroscopy and the measurement of optoelectronic properties will be described;
3. the last section will discuss the optical and electro-optical characterization of thin films.

3.1 Synthesis and characterization of thin films

3.1.1 Chemical solution deposition

The synthesis of the thin films presented in this thesis is done using chemical solution deposition (CSD). As explained in Section 2.4.1, this technique requires two steps: first, the preparation of a precursor solution, and second, the fabrication of a thin film by spin-coating and successive thermal treatment. Prior to the deposition of the functional perovskite, e.g., $BiFeO_3$, highly-oriented seed layers e.g., $PbTiO_3$ or $LaNiO_3$, are deposited to obtain textured films. All chemical reagents were purchased from Merck unless otherwise specified.

The first seeding strategy used in this thesis, and the one used for the films in the physical investigations is a highly-oriented $PbTiO_3$ seed layer. (see Section 4.2) [136, 137] For the fabrication of a highly-oriented $PbTiO_3$ seed layer, a precursor solution was prepared by combining lead(II) acetate ($\geq$ 99.99%) and ti-

tanium(IV) isopropoxide ($\geq$ 98.0%) as metal precursors in 1-methoxy-2-propanol (MePro) ($\geq$ 99.99%). The crystallization water from lead(II) acetate was removed by freeze-drying. Acetylacetone ($\geq$ 99.99%) was added to modify the titanium alkoxide precursor.[138] The mixture was stirred and refluxed under an inert atmosphere for 2 hours. Then, the solution was distilled to remove the remaining acetates and isopropanol side products, and diluted with MePro until it reached a concentration of 0.1 M. A Pb^{2+} excess of 30% was included to compensate for PbO sublimation during deposition.[139] The solution ages and is not usable after 30 days; longer times lead to a decrease in the degree of orientation of the films. The resulting precursor solution was spin-coated on the substrate of choice at 3000 rpm and dried at 130 °C. It was then pyrolyzed at 350 °C and crystallized at 700 °C in an 80% N_2 and 20% O_2 atmosphere using rapid thermal annealing (RTA, Annealsys AS-MASTER 2000). The resulting thickness is (10 ± 5) nm. All the RTA heating rates were set to 50 °C s^{-1} unless otherwise specified.

Another strategy is based on using a highly-oriented $LaNiO_3$ seed layer. The process was adapted from Miyazaki et al.[140]. $La(NO_3)_3 \cdot 3\,H_2O$ ($\geq$ 98.0%) and $Ni(OAc)_2 \cdot 4\,H_2O$ ($\geq$ 98.0%) were freeze-dried and dissolved in 2-methoxyethanol (MOE) and 2-aminoethanol ($\geq$ 98.0%) (mixing ratio of 9:1). Then, the solution was refluxed for 2 hours. The final concentration of the solution was 0.3 M. The solution expires in 7 days; precipitates are formed in the solution at longer times. The solution was spin-coated and dried at 150 °C for 3 min. Pyrolysis was extensively optimized from the results obtained in this thesis as shown in Section 4.2. The optimized pyrolysis temperature was 450 °C for 15 min. Crystallization was performed at 700 °C for 5 min. To obtain oriented films, the deposition-crystallization process needs to be repeated five times. The degree of orientation towards the $(100)_{pc}$ increases after each deposition, saturating after five layers. Here, a heating rate of 3 °C s^{-1} was necessary to obtain highly-oriented films.

For the preparation of $BiFeO_3$ thin films a precursor solution was prepared following a nitrate-based route.[141, 142] Four systems with different dopings are used in this thesis: $BiFeO_3$, $BiFe_{0.95}Mn_{0.05}O_3$, $BiFe_{0.98}Ti_{0.02}O_3$, and $BiFe_{0.93}Mn_{0.05}Ti_{0.02}O_3$. The stoichiometry of the different compounds refers to the nominal stoichiometry of the solution and not necessarily the final stoichiometry of the compound. The starting solution was composed of $Bi(NO_3)_3 \cdot 5\,H_2O$ ($\geq$ 98.0%), $Fe(NO_3)_3 \cdot 9\,H_2O$ ($\geq$ 98.0%), and $Mn(NO_3)_2 \cdot 4\,H_2O$ ($\geq$ 99.99%) in MOE. 5% Bi^{3+} excess was used to compensate for Bi_2O_3 sublimation during the high temperature annealing of the films.[116] Ti was introduced through a 0.1 M precursor solution prepared using titanium(IV) isopropoxide, acetylacetone, and MOE as the solvent.

The metal ion concentration in the solution was 0.25 M, with the assumption that Mn^{x+} and Ti^{4+} would occupy the Fe^{3+} sites in the $BiFeO_3$ perovskite structure.[143] Manganese is introduced from a Mn^{2+} precursor. However, in the $BiFeO_3$ structure, it commonly adopts a Mn^{3+} oxidation state,[144] but small amounts of Mn^{2+} and Mn^{4+} are also commonly observed.[145]. Consequently, in the following, the text will refer to Mn^{x+}.

The molecular mass of the hydrated precursors was used to calculate the concentration of the solution. Non-hydrated precursors are usually preferred for the preparation of precursor solutions. However, several attempts to freeze-dry $Fe(NO_3)_3 \cdot 9\,H_2O$ were unsuccessful. To remove the crystallization water from the solution, a stoichiometric amount of acetic anhydride ($\geq 98.0\%$) was added. Acetic anhydride reacts with the crystallization water, producing acetic acid as a product. This reaction is highly exothermic.[146] Therefore, acetic anhydride must be added slowly to prevent excessive heating. The acetic acid byproduct also acts as complexing agent for the metal cations.[142] The $BiFeO_3$ precursor solution was deposited on the substrate of choice and it was spin-coated at 3000 rpm during 30 s. The coated substrate was then heated at 90 °C for gelation, as previously described by Zhang et al.[142] The gel was then dried at 270 °C. Pyrolysis and crystallization were performed in pure O_2 atmosphere at 450 °C for 5 minutes and 600 °C for 5 minutes respectively, using a RTA furnace. The deposition-crystallization process resulted in films with a thickness of 25 nm, which could be repeated to create thicker films.

Substrates

The films fabricated in this thesis were deposited on different substrates. A summary of the different substrates used is shown in Table 3.1. A non-ferroelectric HfO_2 layer was deposited between the film and the substrate (fused silica, sapphire, and magnesium oxide) to prevent diffusion from the film into the substrate.

	Supplier	Stack
Platinized silicon	Sintef	$Pt(100\,nm)/TiO_x(20\,nm)/SiO_2(500\,nm)/Si$
Fused silica	Siegert Wafer	$HfO_2\ (23\,nm)/SiO_2$
Sapphire	Siegert Wafer	$HfO_2\ (23\,nm)/Al_2O_3$
Magnesium oxide	Biotain Crystals	$HfO_2\ (23\,nm)/MgO$
LAO	Crystal	$LaAlO_3$

Table 3.1: Substrates used for the deposition of $BiFeO_3$ films.

3.1.2 Microfabrication techniques

To characterize the electrical properties, three different types of devices were fabricated using lift-off photolithography and sputtering. For the out-of-plane electrical properties, metal-insulator-metal (MIM) structures were built. A scheme of the device is shown in Figure 3.1 (a). To characterize the in-plane fer-

roelectric properties, the bulk photovoltaic and the electro-optic response, interdigitated electrodes (IDE) were patterned on the $BiFeO_3$ films as shown in Figure 3.1 (b). Embedded IDEs (Figure 3.1 (c)) were patterned prior to the deposition of the $BiFeO_3$.

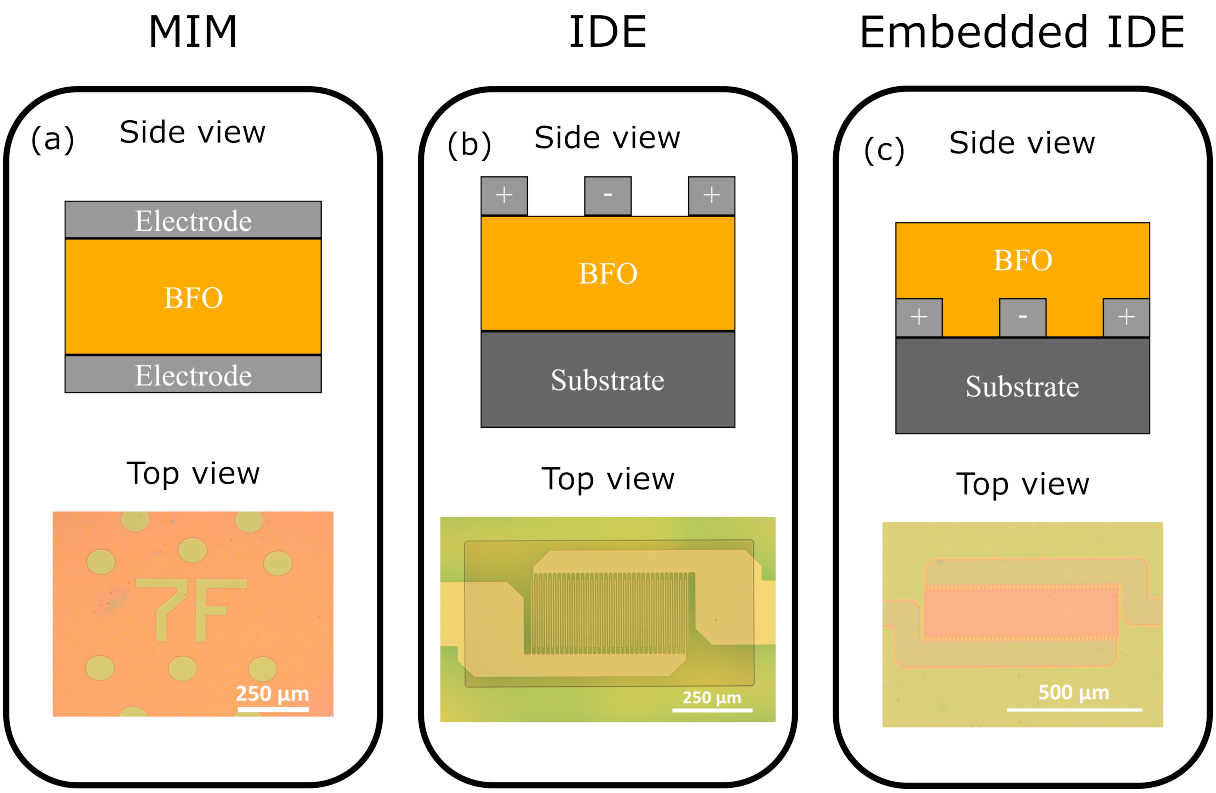

Figure 3.1: (a) Schematic of a MIM electrode configuration and top-view optical microscope image of circular platinum capacitors on $BiFeO_3$. (b) Schematic of an IDE electrode configuration and optical microscope image of a $BiFeO_3$ film with platinum interdigitated electrodes. (c) Schematic of an embedded IDE electrode configuration and optical microscope image of a $BiFeO_3$ film with an embedded FTO IDE underneath.

The samples were patterned using a bi-layer resist method. First, a polydimethylglutarimide-based resin (LOR3A, Microchem) was spin-coated. This resin is not a photoresist, but it shows a controlled dissolution rate that can be used to obtain an undercut that enables a high-quality lift-off. Then, a positive photoresist (S1813, Rohm and Hass Electronic Materials) was spin-coated on the top of the LOR3A. Exposure was performed with a maskless lithography tool (MLA 150, Heidelberg Instruments). Prior to exposure, a dosing test was performed to adapt the dose and the development time to the substrate of choice and the dimensions of the device. The development of the pattern was performed using MF-319 developer (Microposit, DOW).

Two electrode materials were used in the thesis, platinum and F:SnO_2. The second was only used in embedded IDE devices, before depositing the functional layer. Platinum was sputtered using a BALTEC MDE020 metallizer. The deposition was performed using an Ar-pressure of 3.5×10^{-2} mbar, a power of 40 W, a distance of 6 cm between the target, and the sample and for a duration of 100 s. Under these conditions, the thickness of the layer was determined to be 100 nm. F:SnO_2 (AJA International) was sputtered using an Orion-8 magnetron sputtering (AJA International). The Ar-pressure was set to 10^{-3} mbar. A power of 110 W during 20 min was used. An additional two-step annealing of the F:SnO_2 films, first at 300 °C for 20 min in air and at 600 °C for 5 min in O_2, was performed to increase conductivity and transparency. Under these conditions, the thickness of the layer was determined to be 100 nm and a conductivity of 100 S cm^{-1}.

Lift-off was performed using remover PG (Microchem). An encapsulating epoxy layer was added to the top IDE structures to prevent electrical arcs between the fingers. An epoxy-based negative photoresist (SU-8 3005, Microchem) was spin-coated on the patterned samples, exposed, developed, and cured to encapsulate the devices.

3.1.3 X-Ray techniques

To analyze the crystal structure, texture, and strain of the films shown in this thesis, $\theta/2\theta$ measurements were performed on a Bruker D8 diffractometer (Bruker, USA) using $\mathrm{Cu-K}_\alpha$ radiation (λ=1.5406 Å).

To compare the degree of orientation of a polycrystalline film, the Lotgering factor (LF) [147] for one specific Bragg reflection was calculated as:

$$LF = \frac{p - p_0}{1 - p} \tag{3.1}$$

where p is the fraction of the sum of the peak intensities corresponding to the orientation of interest to that of the sum of all diffraction peaks measured in the oriented film and p_0 is the p of a material in which the grains are randomly oriented, as shown in the powder diffraction file (PDF). The LF is 1 for perfect out-of-plane orientation and 0 for completely random orientation.

Strain measurements by X-Ray diffraction

The thermal expansion coefficient (TEC) mismatch between the film and the substrates leads to thermally induced substrate stress in the crystallized films.[148] Crystallization occurs at high temperatures. During cooling down, the film and the substrate try to contract differently due to their mismatch in TEC. However, due to clamping between the film and the substrates, the mismatch results in strained films.

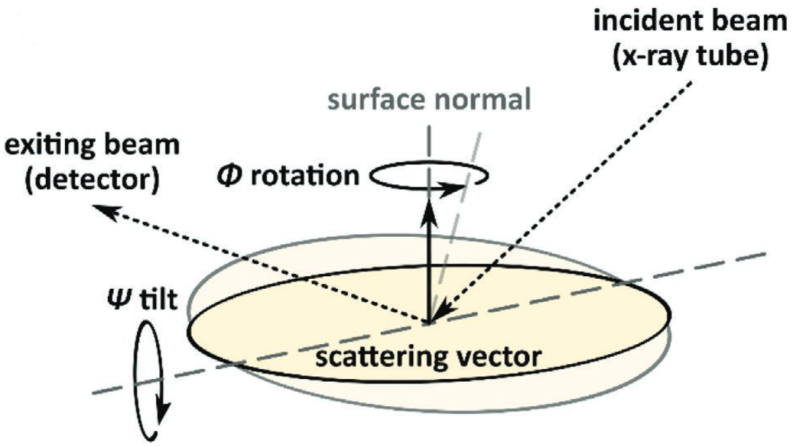

Figure 3.2: Schematic of the $\sin^2(\Psi)$ X-ray diffraction configuration. Change of the sample orientation relative to the scattering vector via Ψ tilts. Reproduced from [149].

The in-plane strain in the films was quantified using a direct strain assessment via $\sin^2(\Psi)$ X-ray diffraction as shown in Figure 3.2. The basics of the procedure are well-described in reference [149]. Some other examples can be found in [150, 151]. In this method, the XRD patterns around one diffraction peak were recorded under different tilt angles. When the tilt angle increases, the scattering vector also changes, probing the crystallographic planes that are more oblique to the film normal. For example, in tensile strained films, the interplanar spacing will be larger perpendicular to the normal of the film than parallel to the normal of the film. This translates into a linear decrease of the interplanar spacing with the $\sin^2(\Psi)$. From that linear change, the deformation can be extracted from the following relation:[149]

$$d_\Psi = \frac{(1+\nu)}{(1-\nu)}\epsilon_{11}d_0(\sin^2\Psi) + \left[1 - \frac{2\nu}{(1-\nu)}\epsilon_{11}\right]d_0 \tag{3.2}$$

where $\epsilon_{11} = \epsilon_{22}$ refers to the in-plane strain, ν is the Poisson ratio and d_0 is the bulk lattice spacing. The fitting of d_{hkl} vs $\sin^2(\Psi)$ allows the determination of ϵ_{11}.

Azimuthal scans

The $\theta/2\theta$ configuration would only provide information about the out-of-plane texture of the film. However, the growth of thin film on single crystal substrates could lead to the formation of an in-plane texture of the film. To determine the in-plane texture of a film, azimuthal scans or ϕ scans were performed. In this measurement, the tilt angle of the diffractometer is set to a constant angle Ψ, appropriate for one hk0 reflection. Then, the azimuth angle (Φ) is varied for a constant 2θ and Ψ.[152]

X-ray reflectivity

X-ray reflectivity (XRR) is an effective technique to measure the thickness, roughness, and density of thin films and multilayers. In this technique, the diffractometer is operated in the symmetric $\theta/2\theta$ configuration, but with 2θ angles between 0°and 10°.

XRR patterns of $LaNiO_3$ thin films were measured to evaluate thickness and density using a PANalytical X'Pert Pro diffractometer (PANalytical) with Cu-K_α radiation. XRR results were fitted using the free software GenX.[153]

3.1.4 Atomic and piezo-response force microscopy

Atomic Force Microscopy (AFM) is a high-resolution imaging technique that uses a sharp tip (tip radius below 10 nm) to scan the surface of a sample at the nanoscale. The probe interacts with the sample's surface, producing a map of its topography.[154] In Piezoresponse Force Microscopy (PFM) a conductive AFM tip measures the piezoelectric response of a material, providing information about its electrical and mechanical properties at the nanoscale.[155]

All the AFM and PFM images were recorded on a MFP-3D Infinity (Asylum Research). AFM images were obtained in tapping mode configuration with an AC160TS-R3 tip (Olympus). The topography was imaged recording the correspondent Z piezo displacement while maintaining the amplitude of the cantilever's first eigenmode (c. 265 kHz) constant at 70 nm. PFM measurements were conducted at the contact resonance in Dual Amplitude Resonance Tracking (DART) mode[156] with a conductive single crystal diamond AD-2.8-AS (ADAMA) with a typical cantilever stiffness of 2 N m^{-1} and resonance of 75 kHz. A 5 kHz and a 1 V amplitude sine wave signal were applied to the conductive tip, creating two sidebands around the contact resonance. The lock-in demodulation of the lowest frequency side band was used to record the PFM amplitude and phase responses. The contact resonance was found around 300 kHz.

3.1.5 Thermal analysis

Thermogravimetric analysis (TGA), which determines mass loss over a temperature range, and differential thermal analysis (DTA), which determines endo- and exothermic event temperatures, were performed to estimate the pyrolysis temperature of the $LaNiO_3$ solution.

The solution was dried overnight at 135 °C to obtain the powder. The TGA/DTA of the powder was performed on an STA409 PC thermal analyzer (Netzsch, Germany), with a heating rate of 10 °C min^{-1} under air atmosphere.

3.1.6 Scanning electron microscopy

The surface of the films deposited on conductive substrates was observed using a Helios NanoLab 650 (FEI, USA) scanning electron microscope (SEM). The images were taken at 3 kV, measuring the secondary electrons using a through-lens detector.

3.1.7 Transmission electron microscopy

Samples for transmission electron microscopy (TEM) analyses were prepared with a focused ion-beam (FEI Nanolab Helios 650 - FIB) lamella preparation procedure. TEM studies were carried out using a Jeol JEM-2100 operated at 200 kV, equipped with JED 2300 EDXS, and a probe Cs-corrected Jeol ARM 200 CF equipped with Centurio EDX system.

3.2 Electrical characterization

3.2.1 Electric field correction in interdigitated electrodes

To characterize the in-plane ferroelectric properties, the bulk photovoltaic and the electro-optic response, interdigitated electrodes (IDE) were used. In this geometry, the electric field must be corrected to account for the curvature of the electric field inside the material. Due to this curvature of the electric field, the specific geometry of the IDE is key to obtaining an effective penetration of the electric field. To estimate the equivalent area of the capacitor and the effective electrode distance required to calculate the electric field, the model discussed in [157] was used. In this approximation, the area is calculated considering that the electrodes extend along the thickness of the material as shown in Figure 3.3.

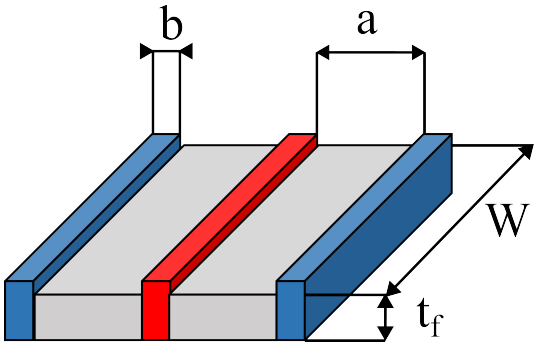

Figure 3.3: Illustration of the assumptions made with the simple model for the behavior of IDE structures. The IDE capacitor behaves like (2N – 1) parallel plate capacitors in parallel.

This approximation is valid as long as the gap between the electrodes a and the finger width b is more than one order of magnitude larger than the thickness of the film t_f. Besides, to avoid a significant contribution to the measured current of the stray field from the tip of the fingers, the finger length W must be two orders of magnitude larger than a. In this approximation, the equivalent area of the capacitor is calculated as $(2N-1)Wt_f$, with N the number of pair of fingers. To account for the curvature of the electric field, a correction factor Δa is used, where $\Delta a \approx 1.324 t_f$. The equivalent distance between electrodes is $a + \Delta a$. Consequently, the capacitance of the IDE is defined as follows:

$$C = \epsilon_0 \epsilon \frac{(2N+1)Wt_f}{a + \Delta a} \tag{3.3}$$

A detailed description of the available models for IDEs' characterization can be found in [158].

3.2.2 Ferroelectric characterization

The characterization of the electrical properties of ferroelectric and dielectric materials, e.g., polarization and zero-field permittivity, is key to assessing the material quality and its suitability for applications. Ferroelectric thin film Analyzer 2000 (aixACCT) was used to perform all these measurements. For each sample, electrical measurements were performed on several electrodes to ensure repeatability.

Small signal capacitance measurements

The zero-field permittivity was extracted from the capacitance values, which were derived from the AC small signal current response of the capacitors upon the application of an AC electric field of 1 kV cm^{-1}.

Polarization measurements

Several measurement methods are available to measure the ferroelectric polarization. The basics of the measurements rely on measuring the current response of a ferroelectric capacitor upon the application of a triangular electric field signal as shown in Figure 3.4.

The measured polarization for an ideal non-leaky capacitor can be expressed as:

$$\Delta P = P(\Delta t) - P(0) = \int_0^{\Delta t} j(t) dt \tag{3.4}$$

where ΔP is the change in polarization over time (Δt) and j the switching current density.

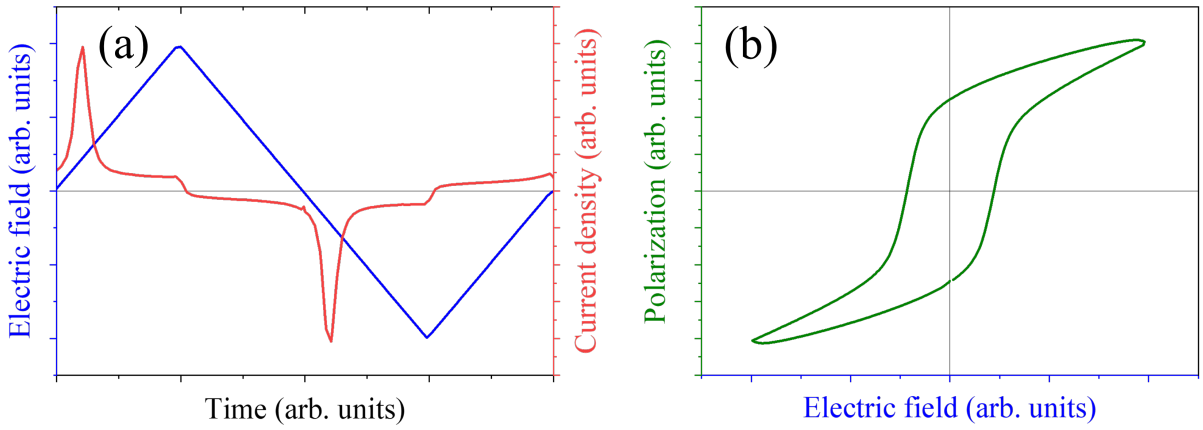

Figure 3.4: (a) Example of the applied electric field waveform and current density response of a $BiFeO_3$ capacitor used for the measurement of polarization hysteresis loops. (b) Typical resulting polarization hysteresis loop.

When measuring the current response of a ferroelectric capacitor, one must take into account parasitic capacitance and other set-up-dependent contributions to the measured signal.[159] In this thesis, the virtual ground method, implemented in the Ferroelectric thin film Analyzer 2000 (aixACCT, Germany), was used to measure the hysteresis loops. This method is especially helpful for small capacitors as it eliminates the parasitic capacitance from cables. In this method, an operational amplifier that has its inverting input connected to the output of a current-to-voltage converter through a feedback resistor and to the ground is used. The voltage is measured as the difference between the operational amplifier's output and the ground. Ideally, the voltage difference between the inverting and non-inverting inputs is zero or minimal, allowing the capacitor being measured to be connected to a virtual ground.[160]

A more complicated situation occurs when leaky capacitors are used. In that case, the electric displacement (D) can be separated into a ferroelectric polarization contribution P^{FE} and a leakage polarization contribution P^{LK}:[137]

$$D = \epsilon E + P^{FE} + P^{LK} \tag{3.5}$$

where the leakage contribution can be written as:

$$P^{LK}(t) = \int_0^t j(\tau)\, d\tau = \dot{E}^{-1} \int_{E(\tau=0)}^{E(\tau=t)} j(E)\, dE \tag{3.6}$$

The electric field of a triangular signal can be written as:

$$E(t) = \begin{cases} 4tfE^{max} & \text{for } 0 \leq t \leq \frac{1}{4f} \\ 2(1-2tf)E^{max} & \text{for } \frac{1}{4f} \leq t \leq \frac{3}{4f} \\ 4(tf-1)E^{max} & \text{for } \frac{3}{4f} \leq t \leq \frac{1}{f} \end{cases} \tag{3.7}$$

where f is the cycling frequency. After integration:

$$P^{LK} = \frac{1}{4fE^{max}} \begin{cases} \int_0^{E^{max}} j(E)dE & \text{for } 0 \leq t \leq \frac{1}{4f} \\ P^{LK}\left(\frac{1}{4f}\right) - \int_{E^{max}}^{-E^{max}} j(E)dE & \text{for } \frac{1}{4f} \leq t \leq \frac{3}{4f} \\ P^{LK}\left(\frac{3}{4f}\right) - \int_{-E^{max}}^{0} j(E)dE & \text{for } \frac{3}{4f} \leq t \leq \frac{1}{f} \end{cases}. \tag{3.8}$$

Assuming that j depends explicitly only on E during the measurement, after one full triangular signal:

$$P^{LK}\left(\frac{1}{f}\right) = \frac{1}{2fE^{max}} \int_{-E_{max}}^{E^{max}} j(E)dE; \tag{3.9}$$

the leakage contribution to the measured polarization is inversely proportional to the frequency and tends to zero at high frequency. If the hysteresis loop is saturated, the D should be linear in $1/\mathrm{f}$, and the y-axis intercept is the remanent ferroelectric polarization.

3.2.3 Dielectric spectroscopy

Dielectric and impedance spectroscopy studies[161–163] of the $BiFeO_3$ film with IDE were performed using a Novocontrol Concept 40 dielectric spectrometer system. Measurements were performed at different temperatures between −50 °C and 150 °C. At each temperature step, the conductivity was recorded using an AC field amplitude of 0.2 V (rms) in the frequency range of 1 mHz ≤ f ≤ 50 kHz.

3.2.4 Optoelectronic characterization

Electrical measurements under light were recorded using a source-meter (Keysight, model B2901A). The current-voltage and current-time curves were measured in the dark and under illumination. Illumination was performed using a 455 nm LED (Thorlabs, model M455L4 Series) that was focused on the IDEs. The direction of the light is kept perpendicular to the surface of the film in all the measurements.

Light-polarization-dependent measurements were obtained using a wire-grid polarizer (Thorlabs, model WP25M-VIS). The intensity of the light was measured using a photodiode (Thorlabs, model S121C). The illuminated area is defined as the spacing between the interdigitated electrode fingers.

3.3 Optical and electro-optical characterization

3.3.1 Prism coupling technique

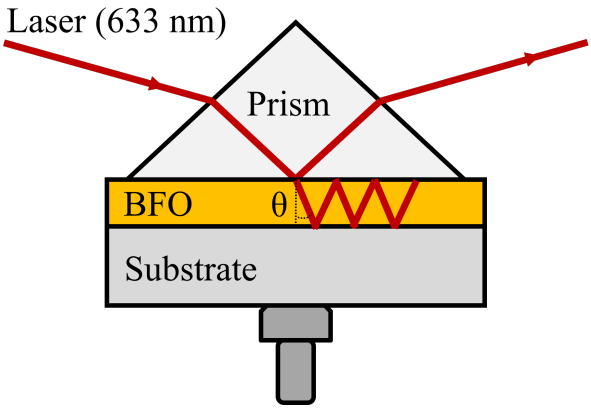

Figure 3.5: Schematic of the prism coupling method. The incident laser beam is reflected at the bottom surface of the prism. A drop in the reflected intensity is observed when a waveguide mode is excited.

The thickness and refractive index of the $BiFeO_3$ thin films were measured using an attenuated total reflectance prism coupling technique. The theoretical description of the technique can be found in [164–167].

A schematic of the technique is shown in Figure 3.5. The technique is based on the principle of light wave coupling through evanescent fields to the mode of thin-film waveguides. In this technique, a high refractive index prism is brought into contact with a thin film so that a low refractive index air gap ($\approx 100\,\text{nm}$) separates the film and the prism. A laser beam (633 nm) strikes the base of the prism and it is reflected to a photo-detector. The light waves in the prism and the film are coupled through their evanescent fields in the gap. At certain angles of incidence, a waveguide mode is excited, resulting in a drop in the reflected intensity. For a given substrate, the modes' positions are linked to the thickness and the refractive index of the film. The mode equation can be written as:[168]

$$\frac{2\pi}{\lambda}\, n\cos(\theta)\; t_f + \;\Psi_{10} + \Psi_{12} = m\pi \;\; (m = 0,\; 1,\; 2\ldots) \tag{3.10}$$

where λ is the wavelength of the laser, n is the film index, t_f is the film thickness Ψ_{10} and Ψ_{12} are the Fresnel phase shifts at the BFO/air and BFO/substrate interfaces, respectively. To perform the measurement, a commercial Metricon model 2010 prism coupler (Metricon, USA) with a GaP prism (Metricon, Prism 200-P-6-GaP) is used.

3.3.2 Teng-Man technique

The electro-optic coefficients in thin films can be determined by measuring the change in the refractive index when an electric field is applied. Three measurement techniques[169] are typically used to measure electro-optic coefficients in thin films: the Mach-Zehnder interferometric technique,[170, 171] the prism coupling technique,[166] and the Teng-Man (TM) technique.[172] This thesis focuses on the Teng-Man method instead of the other aforementioned methods. The prism coupling technique is not compatible with interdigitated electrodes due to the need for close contact between the film and the prism. The Mach-Zehnder interferometric method requires angular scans using both s- and p-polarized light, which makes it more time-consuming. Additionally, the signal is more sensitive to the mechanical vibrations of the optical components.

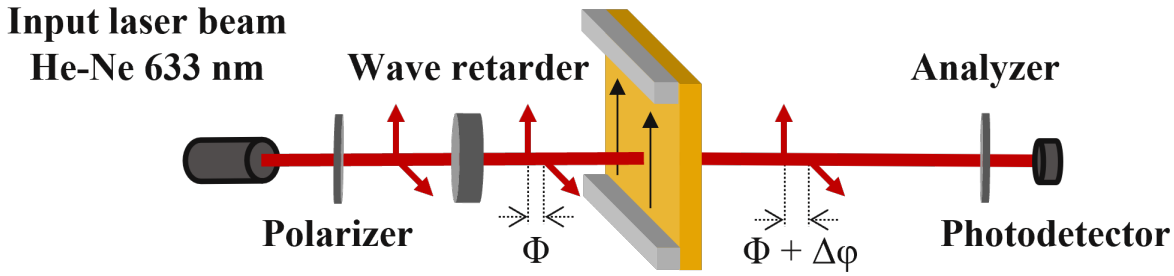

Figure 3.6: Schematic of the Teng-Man set-up in transmission geometry. The signal change at the photodetector when an AC electric field is applied to the interdigitated electrodes is monitored using a lock-in amplifier.

The TM technique is based on the measurement of the electric-field-induced phase shift between two beam components with mutually perpendicular light polarization. A schematic of the Teng-Man measurement set-up is shown in Figure 3.6. The EO coefficients were measured using an in-house built set-up, consisting of a He-Ne laser with a wavelength of 633 nm (Thorlabs, HRS015B), two wire grid polarizers (Thorlabs, WP25M-VIS), a liquid crystal wave retarder (Thorlabs, LCC1423-A) coupled to a liquid crystal controller (Thorlabs, LCC25) and a lock-in amplifier (Zurich Instruments, HF2LI 50 MHz).

A linearly polarized laser beam oriented at 45° with respect to the IDE fingers is focused on the device. The polarized light undergoes a controlled phase shift (Φ) in the liquid crystal wave retarder. The slow axis of the liquid crystal wave retarder is aligned with the IDE fingers. This allows to shift the phase of

the orthogonal components of the 45° linearly polarized light, inducing a phase shift from 0 to 2π. Then, an extra phase shift is induced in the poled polycrystalline $BiFeO_3$. The preferential orientation of the optical axis of individual grains after poling creates a birefringence in the film. This phase shift will be modulated using a unipolar AC field, allowing the extraction of the electric field-induced index change in the film. The total change of phase is converted into an intensity modulation by placing a polarizer oriented at 90° with respect to the first polarizer and a photodetector. The mathematical description was adapted from [134, 173]. The light electric field after going through the different polarizers can be written in a Jones formalism as:

$$\mathbf{E}_{\text{out}} = \frac{1}{2}\begin{pmatrix} +1 & -1 \\ -1 & +1 \end{pmatrix}\begin{pmatrix} t_{\parallel} & 0 \\ 0 & t_{\perp} \end{pmatrix}\begin{pmatrix} e^{i\Phi_{\text{LCC}}} & 0 \\ 0 & 1 \end{pmatrix}\begin{pmatrix} 1 \\ 1 \end{pmatrix}\frac{E_0}{2\sqrt{2}} \tag{3.11}$$

where $t_{\parallel}$ and $t_{\perp}$ are the complex transmission coefficients of the samples for waves with polarization parallel and perpendicular to the direction of the ferroelectric polarization, Φ_{LCC} is the phase shift between $\parallel$ and $\perp$ waves produced by the liquid crystal wave retarder and E_0 is the electric-field amplitude of the incident beam. The voltage generated by the photodiode (V_{PD}) is given by:

$$V_{\text{PD}} = V_0\left[\tau_{\parallel}^2 + \tau_{\perp}^2 - 2\tau_{\parallel}\tau_{\perp}\cos\left(\Phi_{\text{LCC}} + \Phi_{\parallel} - \Phi_{\perp}\right)\right] \tag{3.12}$$

where $\tau_{\parallel,\perp}$ and $\Phi_{\parallel,\perp}$ are the modulus and argument of the transmission coefficients. Assuming that $\tau_{\parallel,\perp}$ are independent of the applied electric field when an electric field (E_{elec}) with an amplitude A is applied to the film, the corresponding voltage modulation (V_{LI}) detected by the lock-in amplifier is given by:

$$V_{\text{LI}} = A \times \frac{\delta V_{\text{PD}}}{\delta E_{\text{elec}}} \tag{3.13}$$

$$V_{\text{LI}} = AV_0\left(2\tau_{\parallel}\tau_{\perp}\frac{\delta(\Phi_{\parallel} - \Phi_{\perp})}{\delta E_{\text{elec}}}\sin\left(\Phi_{\text{LCC}} + \Phi_{\parallel} - \Phi_{\perp}\right)\right). \tag{3.14}$$

The change of phase shift between $\parallel$ and $\perp$ waves when an electric field is applied to the material can be written as:

$$\frac{\delta(\Phi_{\parallel} - \Phi_{\perp})}{\delta E_{\text{elec}}} = \frac{\pi}{\lambda}n_e^3\left(r_{33} - \frac{r_{13}n_0^3}{n_e^3}\right)L_{\text{BFO}} \tag{3.15}$$

where L_{BFO} is the thickness of the $BiFeO_3$ layer affected by the electric field, and n_o and n_e are the ordinary and extraordinary index of $BiFeO_3$, respectively. From equations 3.12, 3.14 and 3.15, the phase change produced by the applied electric field can be expressed as a function of the amplitude of the V_{PD} and V_{LI} curves and r_{eff} can be written as:

$$r_{\mathrm{eff}} = r_{33} - r_{13}\frac{n_o^3}{n_e^3} = \frac{\lambda V_{\mathrm{LI}}^0}{\pi n_e^3 L_{\mathrm{BFO}} A V_{\mathrm{PD}}^0} \tag{3.16}$$

V_{PD} is obtained by measuring the voltage generated by the photodiode without applying an electric field to the sample. The dependence of V_{PD} on the phase shift induced by the liquid crystal wave retarder is measured. The maximum of this V_{PD} curve corresponds to $\Phi + \Delta\varphi = \pi/2$ and the minimum to $\Phi + \Delta\varphi = \pi$. Then, a unipolar sinusoidal AC signal is applied to the interdigitated electrodes, changing the refractive index of $BiFeO_3$, and modifying the change of phase $\Delta\varphi$ that modulates the signal of the photodiode. The change in amplitude and the phase of the signal is recorded by a lock-in technique due to the low signal-to-noise ratio of the induced change. V_{LI} is recorded as a function of the phase shift induced by the liquid crystal wave retarder.

Several assumptions have been considered to measure r_{eff}. First, in this mathematical description, the experimental error resulting from the reflections at the SU8/film and film/substrate interface has not been included. Indeed, a more accurate determination of the EO coefficients requires numerical calculations that involve the anisotropic Fresnel equation for a multilayer film stack. In addition, the description assumes that the absorption coefficient of $BiFeO_3$ at these wavelengths does not change with the applied electric field. This assumption seems reasonable since the wavelength under study is far from the bandgap of $BiFeO_3$, where the largest electrochromic effect is expected.[174]

3.3.3 UV–visible spectrophotometry

The transmittance of the FTO-embedded IDEs was measured using an optical microscope (Olympus BX51) coupled to a spectrophotometer (Andor Kymera 328i-C) through an optical fiber. A halogen lamp was used as the light source.

Chapter 4

New strategies towards high-quality polycrystalline $BiFeO_3$ films

4.1 Motivation

Solution-processing or sol-gel techniques are low-cost alternatives to vacuum-based techniques for the fabrication of ferroelectric thin films. However, extensive optimization of the solution chemistry and the processing conditions is needed to obtain films with high quality.

In this chapter, the structural and electrical characterization of solution-processed films fabricated following different strategies is discussed. The control of texture, doping, and different electrode configurations is used to fabricate $BiFeO_3$ films with electrical properties that rival those obtained by vacuum-based techniques. The chapter targets the development of a prototypical $BiFeO_3$ system, where optically induced functionalities such as the bulk photovoltaic effect or the electro-optic effect can be studied. The latest is key for the physical investigations performed during this Ph.D. thesis.

As discussed in Section 2.4.1, $BiFeO_3$ suffers from high leakage currents, which make the fabrication of high-quality thin films challenging. The first objective of the present work is the development of solution-processed $BiFeO_3$ films with low leakage currents. Several processing parameters, such as crystallization temperature, solution Bi-excess, or thickness, were optimized to obtain high-quality films. Therefore, in this chapter, only the key and distinctive achievements toward the development of $BiFeO_3$ films with electrical properties rivaling those measured in epitaxial films are described.

First, the strategies that were followed to control the texture of polycrystalline $BiFeO_3$ are discussed. Then, the focus is shifted to the influence of doping, particularly Ti^{4+} and Mn^{x+}, on the charge transport properties of $BiFeO_3$. The chapter finishes with a discussion of new electrode configurations with increased fatigue and temperature resistance using transparent conductive oxides.

4.2 Control of texture using seed layers

The properties of noncentrosymmetric oxide crystals are anisotropic. Therefore, engineering the orientation of the crystal or the texture in polycrystalline films is key for thin film applications. For example, in $BiFeO_3$ the ferroelectric fatigue properties can be enhanced by orienting the film towards the $[100]_{pc}$ or $[110]_{pc}$ direction.[98] Besides, an out-of-plane orientation that does not match the polarization axis of the ferroelectric allows for easier engineering of the domain structure. This can be used to optimize properties that depend on the domain structure, such as the conductivity[126] or the extrinsic contributions to the piezoelectric effect, as demonstrated in domain-engineered $BaTiO_3$.[175, 176]

Several strategies have been discussed in the literature to control the orientation of $BiFeO_3$ using solution deposition methods. The most straightforward strategy to fabricate oriented films is the use of single crystal substrates such as (100) $SrTiO_3$.[141, 142] However, the use of expensive single-crystal perovskite oxide substrates is not compatible with industrial manufacturing. On the other hand, silicon is the most important substrate for applications, but it shows a large lattice mismatch with the perovskite structure of $BiFeO_3$. To orientate perovskites in substrates without crystallographic matching, seed layers between the substrate and the functional layer are commonly used. In $BiFeO_3$, using textured perovskite back electrodes such as (111)-oriented $SrRuO_3$[120] or (100)-oriented $LaNiO_3$[107, 177, 178] and depositing seed layers such as (100)-oriented Bi_2O_3,[116] PbO,[179] and $Ca_2Nb_3O_{10}$.[180] were demonstrated to be an effective strategy to obtain well-oriented films. However, all these $BiFeO_3$ films showed leaky ferroelectric loops or the electrical properties were only recorded at high frequencies (100 kHz), where the large switching current (frequency-dependent) hinders the leakage currents.

Three strategies to engineer the orientation of $BiFeO_3$ are presented in this section. First, the main strategy used in the thesis will be discussed, the use of a $PbTiO_3$ seed layer. The superior electrical properties of $BiFeO_3$ films on $PbTiO_3$ combined with the industrial scalability of the process makes it the system of choice for physical investigations. Other strategies such as the use of highly oriented $LaNiO_3$ bottom electrodes and $LaAlO_3$ single crystal substrates are also discussed.

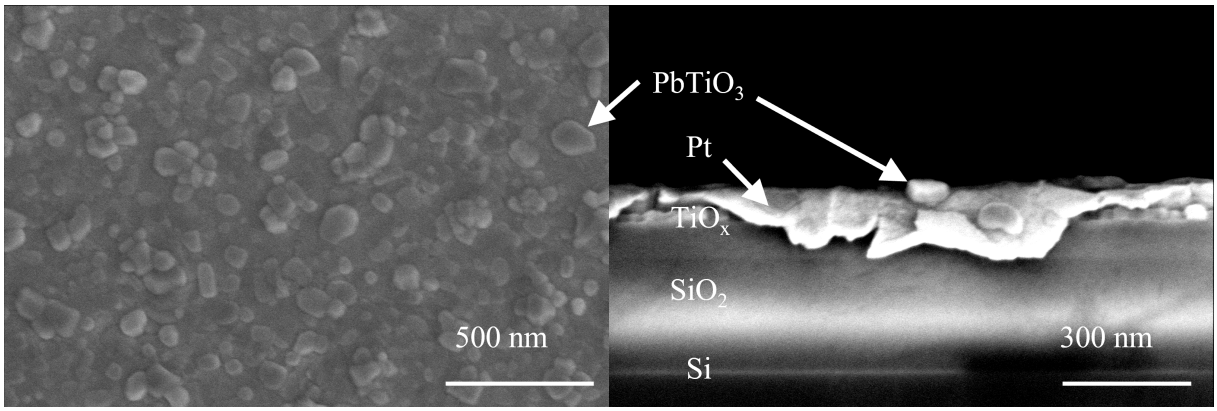

Figure 4.1: (a) Top-view SEM micrographs of the $PbTiO_3$ seed layer deposited on platinized silicon substrates. (b) Cross-section.

4.2.1 $PbTiO_3$ seed layer

The first approach to tune the orientation of $BiFeO_3$ is the use of a $(100)_{pc}$-oriented $PbTiO_3$ seed layer. Godard et al.[136] developed a process to synthesize highly oriented $PbTiO_3$ seed layer using 1-methoxy-2-propanol as a solvent. This highly oriented seed layer was proved to induce a high orientation towards the $(100)_{pc}$ in $PbTi_{0.52}Zr_{0.48}O_3$ thin films. A SEM micrograph of the seed layer can be found in Figure 4.1. They display nanocrystal clusters of $PbTiO_3$ with well-defined facets.

$BiFe_{0.93}Mn_{0.05}Ti_{0.02}O_3$ thin films with different thicknesses with and without $PbTiO_3$ seed layer were synthesized on commercial platinized silicon substrates as described in Section 3.1.1. The crystallographic structure of the films with and without seed layer was characterized via X-ray diffraction (XRD). The XRD patterns of the films with a thickness of 50 nm, 100 nm and 200 nm, with and without $PbTiO_3$ seed layer are depicted in Figure 4.2. The Miller indices for a pseudocubic notation system were used to name

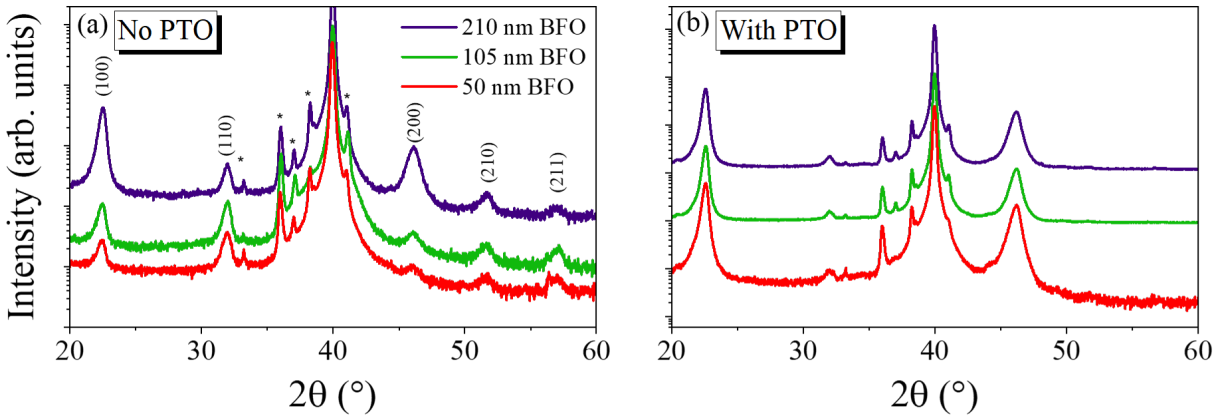

Figure 4.2: (a) XRD patterns of $BiFeO_3$ thin films without the $PbTiO_3$ seed layer. (b) with the seed layer (*: refers to the platinized silicon substrate peaks)

the peaks. The pattern indicates polycrystalline $BiFeO_3$ with no secondary phases according to its PDF card (# 00-066-0439).[181] No splitting of the $(110)_{pc}$ peak is observed due to the modification of the lattice parameters induced by Mn-doping.[120]

The different relative intensity between the $(100)_{pc}$ and the $(110)_{pc}$ reflections indicates different out-of-plane textures between the films. The degree of texturing was quantified using the Lotgering factor (LF) as described in Section 3.1.3. For the non-seeded samples, the LF is 0.19 for a 50 nm film, 0.32 for a 100 nm film, and 0.81 for a 200 nm. For the samples with a PTO seed layer, the calculated LF is 0.98 for a 50 nm film, 0.97 for a 100 nm film, and 0.96 for films with a thickness of 200 nm. The increased degree of orientation of the non-seeded films with thickness indicates that the crystallization of $BiFeO_3$ on $(100)_{pc}$ planes is energetically favored. The highly oriented $PbTiO_3$ favors heterogeneous nucleation of $BiFeO_3$ on the seed layer, inducing an orientation of the out-of-plane direction of the film towards the $[100]_{pc}$ direction.

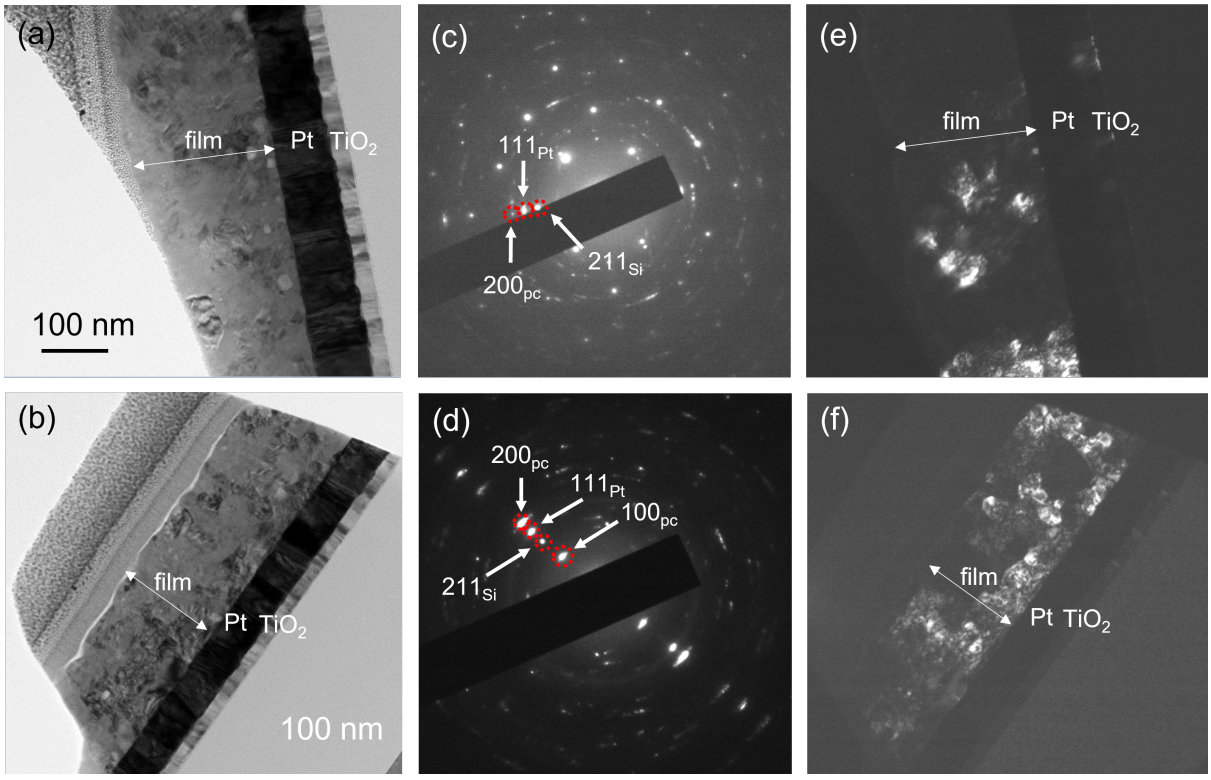

Figure 4.3: Bright-field (BF) TEM micrographs, selected area electron diffraction (SAED) diffractograms and dark-field (DF) TEM micrographs of $BiFeO_3$ films without seed layer (up) and with seed layer (down).

Figure 4.3 (a) and (b) shows the bright-field TEM cross-sections for the $BiFeO_3$ films with a thickness of (200 ± 20) nm without and with seed layer respectively. Both films show a granular morphology. Interestingly, no columnar structure, i.e., grain extending along the whole thickness, is observed in the highly oriented samples. A columnar structure usually appears in polycrystalline films with such a high degree of orientation.[67, 179]

The increased degree of texture in the film with seed layers can also be observed in the selected area electron diffraction (SAED) micrographs for the sample with seed layer (Figure 4.3 (d)) compared to the sample without (Figure 4.3 (c)) seed layer. The SAED diffractogram of the sample with the seed layer does not show the characteristic diffraction rings that usually appear in randomly oriented ceramics.[182] Instead, it displays an elongated shape of the $[100]_{pc}$ and $[200]_{pc}$ reflections indicating that the films are $[100]_{pc}$-oriented when the seed layer is used. The $[100]_{pc}$ orientation of the perovskite coincides with the [111] orientation of the platinum bottom electrode, suggesting that the highly-oriented platinum substrate plays a role in the orientation of the perovskite. When the seed layer is used, the grains are $[100]_{pc}$-oriented as $[100]_{BFO} \| [100]_{PTO} \| [111]$Pt. On the other hand, the film without a seed layer does not show a crystallographic orientation matching between the oriented Pt and the film (Figure 4.3 (f)).

The dark-field (DF) image of the $(100)_{pc}$ reflection of the $BiFeO_3$ film with seed layer (Figure 4.3 (f)) displays a high concentration of $(100)_{pc}$ grains (brighter grains) close to the BFO/Pt interface. On the other hand, far from the BFO/Pt interface, the concentration of $(100)_{pc}$-oriented grains is lower, in agreement with the slight reduction of the LF with thickness in the seeded samples. The DF micrograph of the films without the seed layer (Figure 4.3 (e)) displays a random distribution of $(100)_{pc}$-oriented grains across the film.

The influence of the seed layer on the surface morphology of the $BiFeO_3$ films is shown in Figure 4.4 (a)-(b). The grain size was measured using ImageJ software. The grain size values are (70 ± 30) nm for the non-seeded film and (140 ± 80) nm for the seeded films. The influence of the seed layer on the cross-sectional morphology was observed by SEM in Figure 4.4 (c)-(d) and in the annular dark-field (ADF) scanning TEM micrographs in Figure 4.4 (e)-(f). The films show similar morphology. Larger grains are observed in the films with seed layer (40 nm to 150 nm) compared to the films without the seed layer (40 nm to 100 nm).

To study the influence of the seed layer on the ferroelectric and electrical properties, Pt/BFO/Pt MIM capacitors were prepared as described in Section 3.1.2. The zero-field relative permittivity at a frequency of 5 kHz and an AC field of 10 kV cm^{-1} was (150 ± 5) and (175 ± 5) before and after poling, respectively, for the four films. The permittivity increases upon poling of the capacitor. $\tan(\delta)$ has a value of 0.1 with and without the seed layer and does not change with poling.

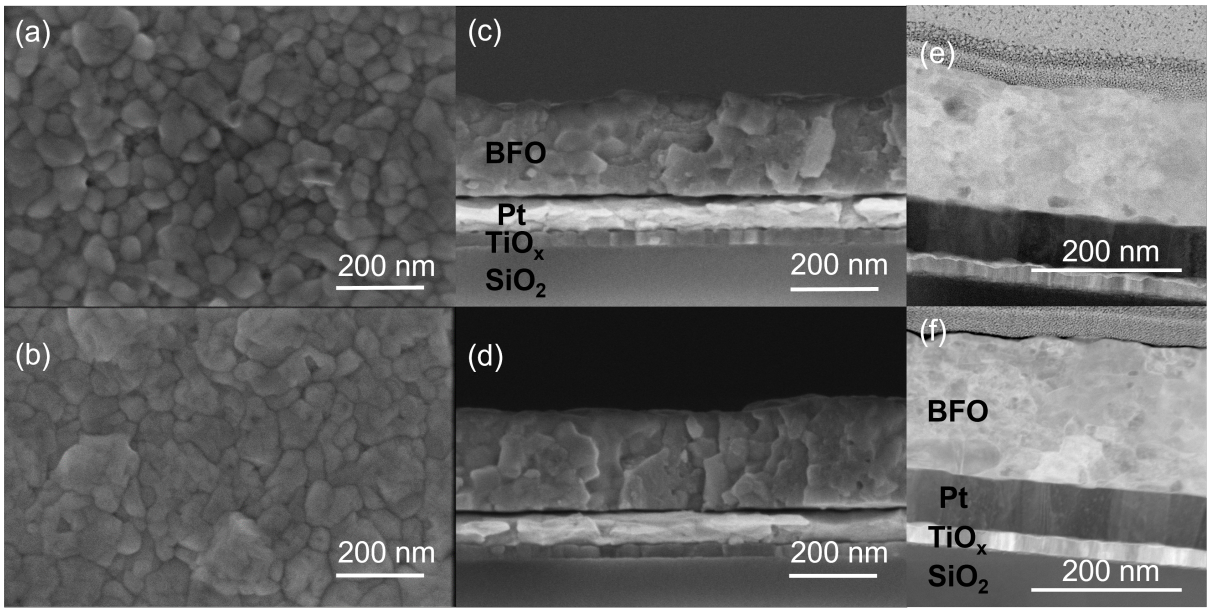

Figure 4.4: (a) SEM surface micrograph of a 200 nm $BiFeO_3$ film without seed layer and (b) with seed layer. (c) Cross-sectional micrograph of a 200 nm without seed layer and (d) with seed layer. (e) Annular dark-field (ADF) scanning TEM (STEM) micrographs of cross-sections of $BiFeO_3$ films without a seed layer and (f) with a seed layer.

The influence of the seed layer on the ferroelectric properties of $BiFeO_3$ is shown in Figure 4.5. The films with a seed layer and larger thickness (200 nm) show sharper P(E) loops with substantially lower leakage. The reduction of leakage current is particularly clear at high electric fields as demonstrated by the transient current density curves. Two hypotheses appear plausible for the reduction of leakage current: the larger grain size when the seed layer is used, i.e., grain boundaries act as conductive pathways, or the different degree of orientation of the film.

To better understand the ferroelectric switching in the seeded $BiFeO_3$ films, frequency- and electric-field-dependent ferroelectric hysteresis loops were recorded. An example of this measurement is demonstrated in Figure 4.6 (a)-(d) for the 200 nm thick $BiFeO_3$ film with $PbTiO_3$ seed layer. Ferroelectric loops with low leakage contribution are measured even when low frequencies (300 Hz) are used. When the cycling electric field is increased, the P(E) loops saturate, but leakage contribution to the measured polarization increases. Special care must be taken in separating the switching contribution and leakage contribution to the measured polarization. According to Equation 3.9 in Section 3.2.2, the leakage contribution to the measured dielectric displacement in the measured frequency range (100 Hz to 5000 Hz) is inversely proportional to the frequency and tends to zero at high frequencies if the P(E) loop is saturated. In this

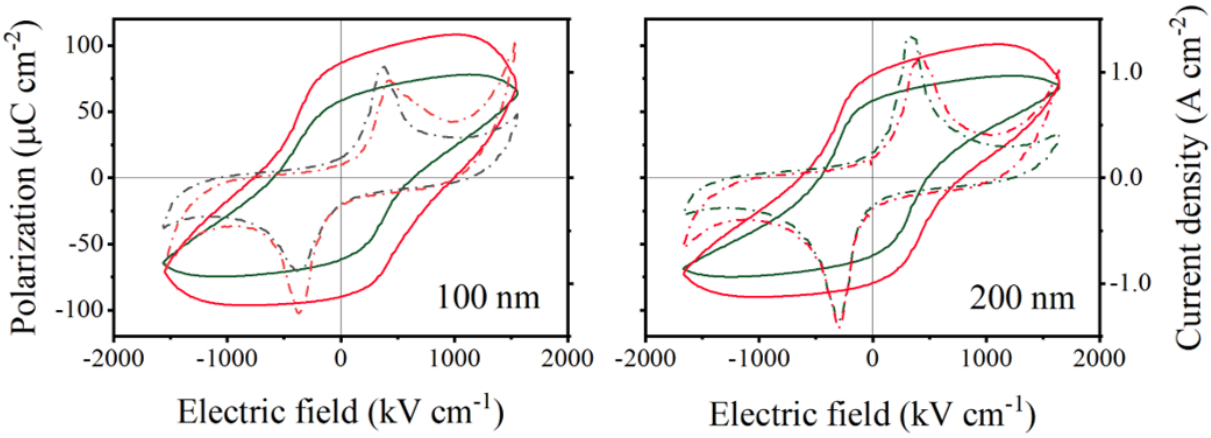

Figure 4.5: Polarization hysteresis loops (solid line) and the current density curves (dashed line) of $BiFeO_3$ thin films in metal-insulator-metal configuration for films with a thickness of 100 nm and 200 nm. The loops were recorded at 1 kHz. Red: Without seed layer. Green: With seed layer.

condition, the remanent ferroelectric polarization can be extracted from the y-axis intercept. Here, the leakage contributions to the remanent polarization plus the real remanent polarization are labeled as apparent remanent polarization (P^{app}).

The values of P^{app} were plotted as a function of the inverse of the frequency in Figure 4.6 (e)-(h). When low cycling electric fields are used, P^{app} shows a non-linear increase with the inverse of the frequency due to the lack of saturation in the hysteresis loops. When the frequency is decreased, the switching and the leakage contributions to the polarization change, giving rise to the non-linear behavior observed at $1400\,kV\,cm^{-1}$ and $1100\,kV\,cm^{-1}$. On the other hand, at high cycling electric fields ($1900\,kV\,cm^{-1}$), the ferroelectric loops start saturating and the leakage current is the only frequency-dependent contribution. At high electric fields, a linear behavior between P^{app} and the inverse of the frequency is obtained. The measured remanent polarization values are summarized in Table 4.1.

	P_r ($\mu C\,cm^{-2}$)	E_c ($kV\,cm^{-1}$)	E_{Break} ($kV\,cm^{-1}$)
No seed layer (200 nm)	49 ± 1	550 ± 30	1800 ± 200
No seed layer (100 nm)	49 ± 1	670 ± 30	1800 ± 200
With seed layer (200 nm)	51 ± 1	500 ± 30	2200 ± 200
With seed layer (100 nm)	50 ± 1	600 ± 40	2000 ± 200

Table 4.1: Calculated P_r, E_c, and E_{Break} for each configuration.

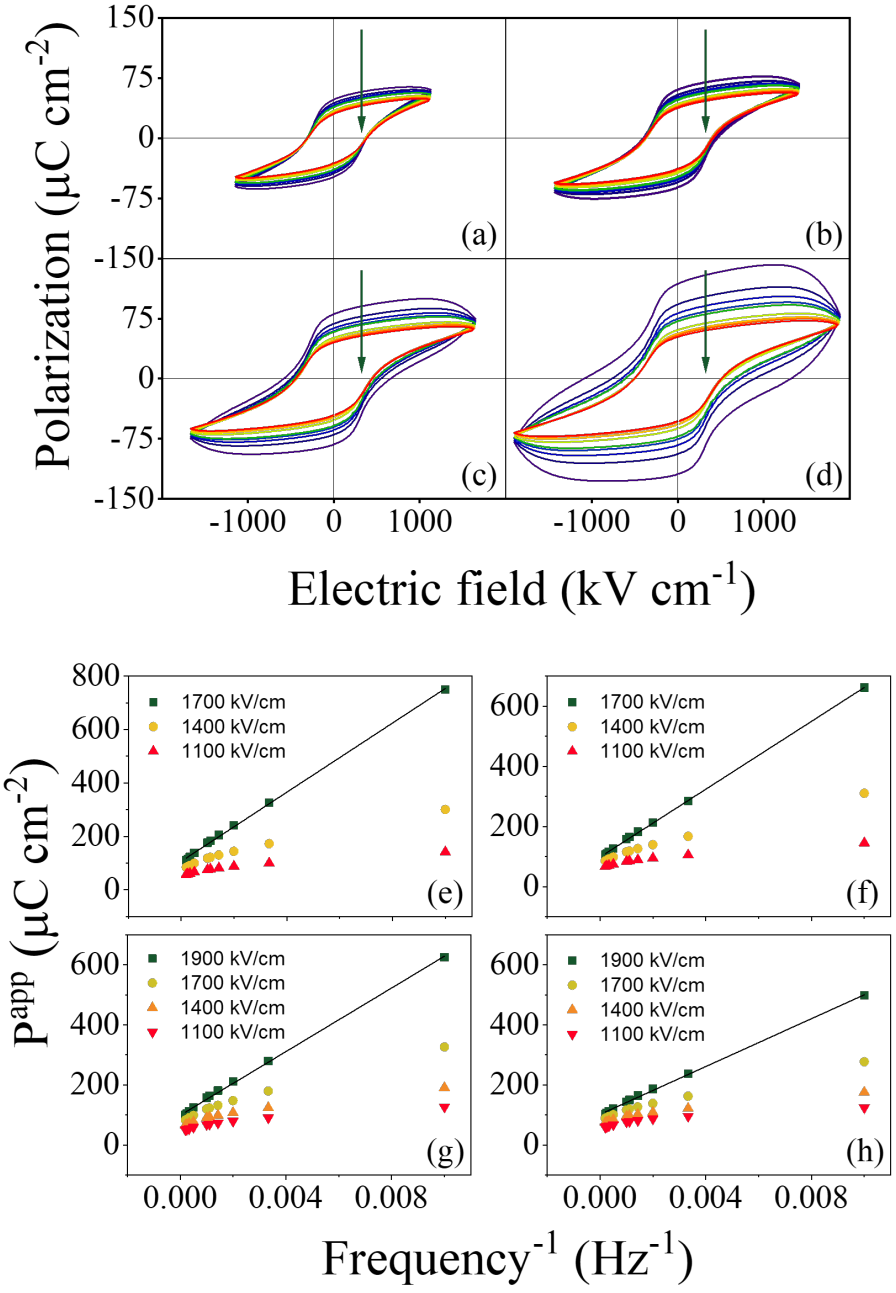

Figure 4.6: (a-d) Ferroelectric hysteresis loops measured at frequencies ranging from 300 Hz and 5 kHz in the $BiFeO_3$ film with $PbTiO_3$ seed layer and a thickness of 200 nm. The cycling electric fields were (a) 1100 kV cm^{-1}, (b) 1400 kV cm^{-1}, (c) 1700 kV cm^{-1}, and (d) 1900 kV cm^{-1}. The arrow indicates increasing frequency. (e-h) P^{app} as a function of the inverse of the frequency in the $BiFeO_3$ capacitors for (e) 100 nm film without seed layer (f) 200 nm film without seed layer (g) 100 nm film with seed layer (h) 200 nm film with seed layer.

Similar P_r values are obtained in the films with and without the seed layer. The P_r values, around $50\,\mu C\,cm^{-2}$, are close to the maximum polarization for a $(100)_{pc}$-oriented film: the polarization is oriented along the $(111)_{pc}$ axis of the $BiFeO_3$ unit cell and has a value of $100\,\mu C\,cm^{-2}$.[98] On the other hand, the coercive field decreases with the use of the $PbTiO_3$ seed layer. This can be explained by the formation of a dielectric material with increased permittivity ($\epsilon_{PTO} \approx 300$) at the Pt-$PbTiO_3$-$BiFeO_3$ interface, which increases the effective electric field that is applied to the $BiFeO_3$ layer and decreases the measured coercive field. When the electric field is applied, the voltage drop is produced in the layer with lower permittivity, which in this case is the $BiFeO_3$ film, resulting in lower values of the coercive field. Additionally, the breakdown electric field of the films increases when the seed layer is used.

The observed P_r and leakage characteristics are similar to those reported for $(100)_{pc}$-oriented epitaxial thin films, processed by PLD[98] and solution-processing.[141] The coercive field values are significantly larger than in epitaxial thin films ($E_c \approx 100\,kVcm^{-1}$). The main origin of the larger E_c may be the granular microstructure, i.e., larger fields are needed to overcome the depolarizing electric fields and mechanical stresses at the grain boundaries. The increase in the coercive field may lead to a more stable domain structure once poling is achieved.

In-plane vs out-of-plane switching

Low leakage ferroelectric loops were obtained in the films deposited on platinized silicon substrates using MIM capacitors in the out-of-plane configuration. However, to study the in-plane ferroelectric properties the films need to be deposited on insulating substrates, e.g., fused silica, sapphire, or MgO.

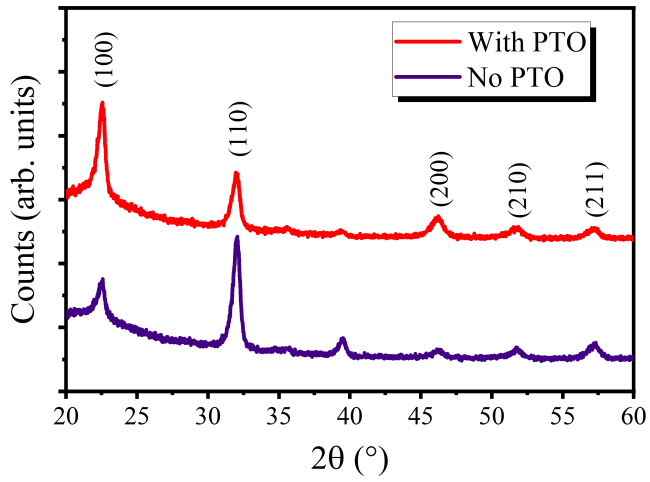

Figure 4.7: XRD patterns of 200 nm thick Mn^{x+} and Ti^{4+} co-doped $BiFeO_3$ thin films on fused silica, with and without seed layer.

$PbTiO_3$ also acts as a seed layer to induce a $(100)_{pc}$ orientation to the $BiFeO_3$ thin films on other substrates without the highly (111)-oriented Pt back electrode. 200 nm thick Mn^{x+} and Ti^{4+} co-doped $BiFeO_3$ thin films were deposited on fused silica substrates following the procedure described in Section 3.1.1. Figure 4.7 shows the XRD patterns of the thin films on fused silica with and without $PbTiO_3$ seed layer. When the seed layer is not used, the films are randomly oriented while the samples with $PbTiO_3$ seed layer are (100)-textured with a LF of 0.65.

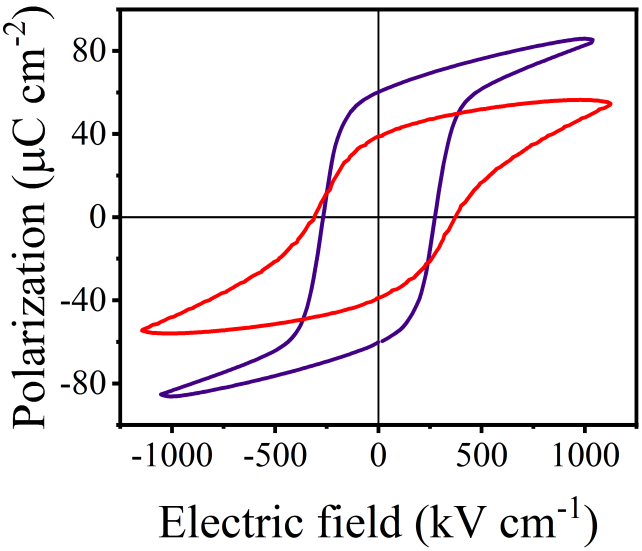

Figure 4.8: Polarization hysteresis loops of 200 nm thick Mn^{x+} and Ti^{4+} co-doped $BiFeO_3$ thin films in out-of-plane (red) vs in-plane configuration (blue).

To study the in-plane ferroelectric properties of films deposited on fused silica substrates, platinum interdigitated electrodes were patterned as described in Section 3.1.2. The IDEs consist of 50 pairs of fingers with an effective length of 370 μm. The width of the fingers is (4.6 ± 0.5) μm, and the space between fingers is (2.5 ± 0.5) μm.

The P(E) loops in both geometries are compared in Figure 4.8. As shown in Figure 4.6, the films cycled at 1000 kV cm^{-1} and 1 kHz in MIM geometry are not saturated, resulting in lower P_r. On the other hand, at the same electric fields, the hysteresis loop in the IDE geometry is saturated. Electric fields larger than 1200 kV cm^{-1} lead to the breakdown of the IDE capacitors. The coercive field is larger in the samples in MIM geometry. The origin of the increase may be due to either the presence of dissimilar interfaces or the presence of chemical gradients within the individual layers. Additionally, sharper P(E) loops are obtained in IDE geometry.

4.2.2 $LaNiO_3$ seed layer

Another strategy to induce a preferential orientation to solution-processed $BiFeO_3$ thin films is the use of a highly-oriented $LaNiO_3$ back electrode on platinized silicon substrates. $LaNiO_3$ is a cubic perovskite with a lattice parameter of 3.84 Å. It has a metallic character at room temperature with a conductivity of $10^4\,\Omega^{-1}\,m^{-1}$. Several reports have shown the possibility to use $LaNiO_3$ to induce a texture to ferroelectric perovskites such as PZT[140, 183] or BTO[184] showing excellent fatigue properties. Moreover, the non-epitaxial growth of (100)-oriented $LaNiO_3$ can be favored under specific processing conditions by techniques such as sputtering[184] or chemical solution deposition.[140, 183]

$LaNiO_3$ thin film were grown as described in Section 3.1.1. Following the procedure discussed by Miyazaki et al.[140] pyrolysis was initially performed at 350 °C for 3 min.

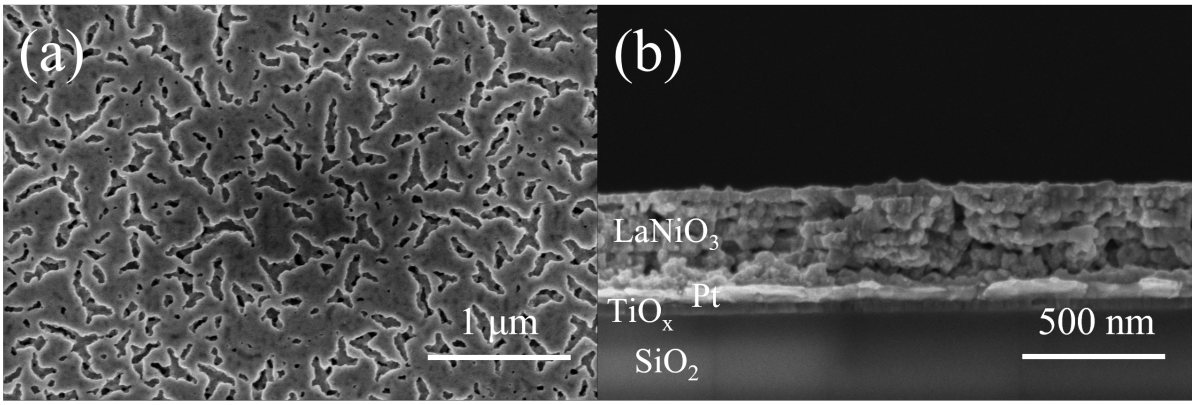

Figure 4.9: SEM micrographs of a $LaNiO_3$ thin film on a platinized silicon substrate, fabricated following the conditions discussed in [140]. (a) Surface morphology and (b) cross-section of the film.

Figure 4.9 shows the morphology of the as-deposited $LaNiO_3$ films. A porous microstructure was obtained. The presence of a porous microstructure is often due to the incomplete pyrolysis of the organic components of the solution.

Figure 4.10 (a) shows the DTA/TGA analysis of the dried solution. The sample was prepared as stated in Section 3.1.5. Three main exothermic peaks were observed in the DTA analysis. The two first peaks, around 270 °C and 450 °C are linked with a reduction of the mass of the sample, which indicate the pyrolysis of the organic compounds. A third peak around 650 °C, without mass loss, indicates the crystallization temperature of $LaNiO_3$. The chosen pyrolysis temperature of 350 °C is not enough to remove the organics of the solution. Therefore, pyrolysis at higher temperatures and longer times was performed to obtain films with lower porosity.

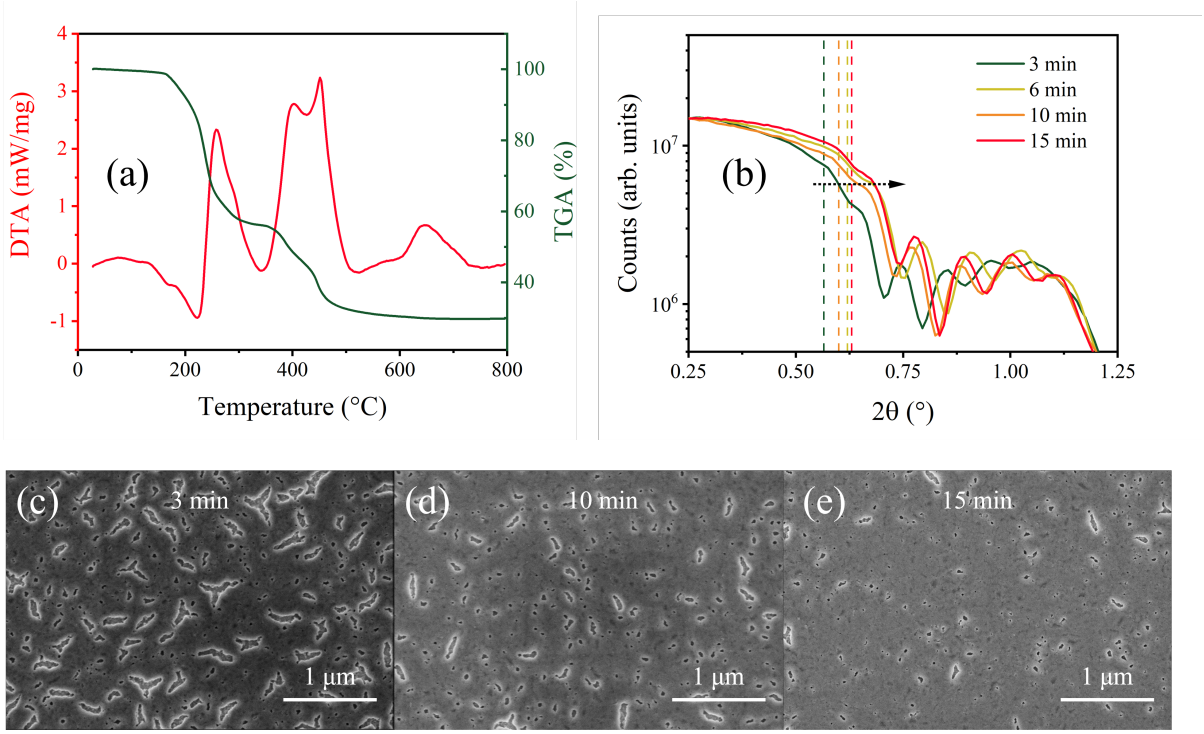

Figure 4.10: (a) DTA/TGA analysis of the $LaNiO_3$ dried solution. (b) XRR intensity pattern and (c) SEM micrographs of $LaNiO_3$ films processed using different pyrolysis times. The arrow in (b) shows the shift of the XRR density edge, indicating the increased density of the film with pyrolysis time.

Following the DTA/TGA results, the pyrolysis temperature was set to 450 °C and the pyrolysis time was varied to reduce the porosity of the film. The porosity of a film is directly linked to its density. For the same material, the higher the density of the material is, the lower the porosity. XRR was used to compare the density of the film pyrolyzed during different times. Figure 4.10 (b) display the XRR pattern of $LaNiO_3$ with different pyrolysis times. The density edge was defined as the half-maximum of the XRR intensity. The density edge of the films is shifted to larger 2θ angles as the pyrolysis time is increased, indicating that the porosity of the film is reduced when the pyrolysis time is increased. The same trend is observed in the SEM images in Figure 4.10 (c). The thickness of the optimized films was (49 ± 3) nm and the roughness (RMS) (3.0 ± 0.5) nm as obtained from the XRR fits.

After the optimization of the $LaNiO_3$ films, $BiFeO_3$ films with a thickness of 50 nm were grown on the $LaNiO_3$ film. The crystallographic structure of the films with and without $LaNiO_3$ was characterized via XRD. The XRD patterns of the $LaNiO_3$ film and the $BiFeO_3$ films with and without $LaNiO_3$ seed layer are depicted in Figure 4.11. No secondary phases are observed. Highly $(100)_{pc}$-oriented $LaNiO_3$ are obtained. The different relative intensity between the $(100)_{pc}$ and the $(110)_{pc}$ in the $BiFeO_3$ films with and without $LaNiO_3$ seed layer indicates different out-of-plane texture of the film. To quantify the degree

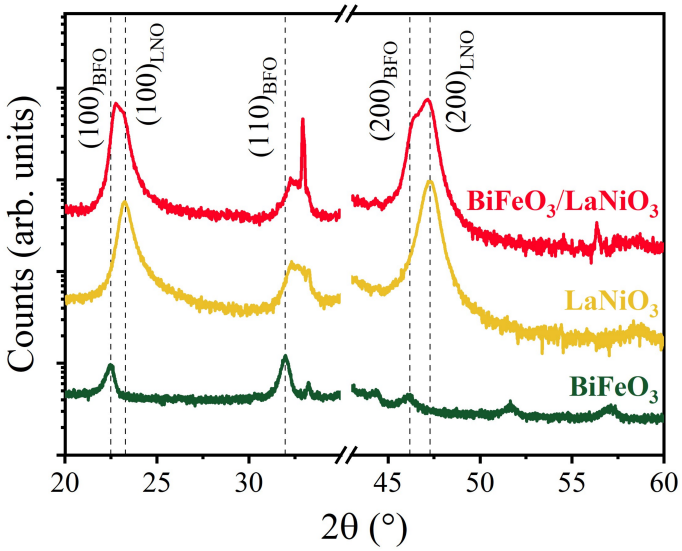

Figure 4.11: XRD patterns of $LaNiO_3$, $BiFeO_3$ and $BiFeO_3/LaNiO_3$ thin films after optimization of the processing parameter.

of texturing, the LF was calculated as described in Section 3.1.3. When the $LaNiO_3$ seed layer is used, the calculated LF of $BiFeO_3$ is increased from 0.19 to 0.87, compared to 0.98 of the $BiFeO_3$ with $PbTiO_3$ seed layer. Additionally, based on the data collected during the optimization of the $LaNiO_3$ seed layer, it was found that low heating rates during the crystallization step are key to achieving such a high degree of orientation.

To study the influence of $LaNiO_3$ in the ferroelectric and electrical properties, Pt/BFO/LNO/Pt capacitors were prepared as described in Section 3.1.2. However, all the measured capacitors in the film were short-circuited. To better understand the shorting of the $BiFeO_3$ capacitors upon deposition on $LaNiO_3$, the chemical composition across the thickness of the film was determined using SIMS.

Figure 4.12 (a) displays the SIMS profile of the $BiFeO_3/LaNiO_3$ stack. The ^{209}Bi extends along the whole thickness of $LaNiO_3$ indicating the presence of $BiFeO_3$ inside the film and therefore the formation of a composite between $BiFeO_3/LaNiO_3$ instead of two independent films. From Figure 4.12 (b), a change in the morphology is observed in the bottom part of the film, which is linked to a reduction of the intensity of ^{139}La. During the deposition of $BiFeO_3$, the solution infiltrates into the porous $LaNiO_3$, forming a composite instead of a sharp interface. The development of high quality $BiFeO_3/LaNiO_3$ requires the reduction of the porosity in the $LaNiO_3$. In this specific case, the modification of the solution chemistry may be the best strategy to reduce the porosity of the film.

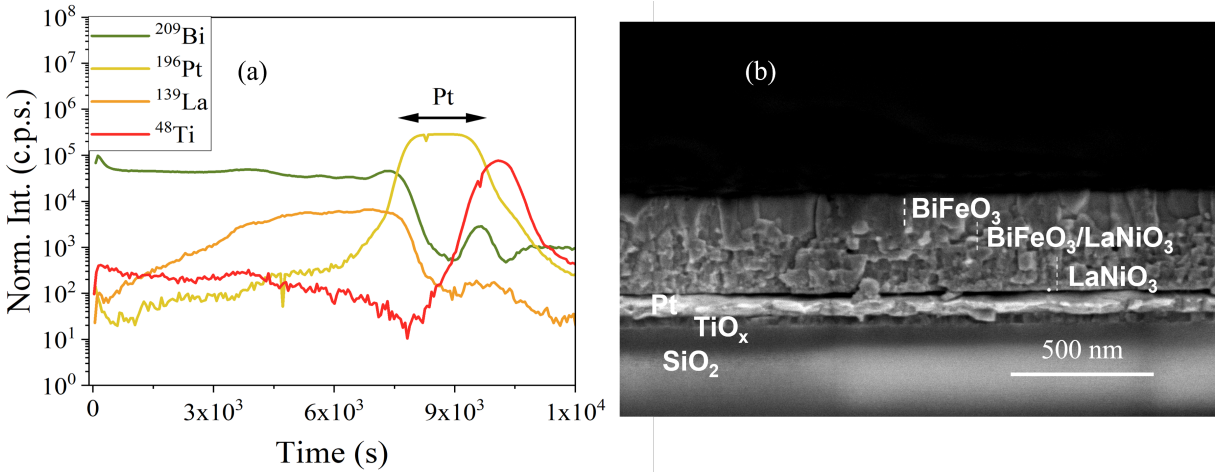

Figure 4.12: (a) SIMS depth profile of the $BiFeO_3/LaNiO_3$ stack. The ^{139}La and ^{209}Bi profiles do not show a sharp interface, which indicates the mixing between $BiFeO_3$ and $LaNiO_3$ layers. The ^{196}Pt and ^{48}Ti peaks under the film correspond to the Pt electrode and the TiO_x adhesion layer. (b) SEM cross-section micrograph of the $BiFeO_3/LaNiO_3$ stack.

This approach was not further pursued in this Ph.D. thesis due to the limitations of the $LaNiO_3$ seed layer. The conductive nature of the seed layer made it incompatible with IDE configuration, key for the physical investigations performed in this thesis. In addition, in MIM configuration, $LaNiO_3$ shows lower conductivity than platinum.

4.2.3 Quasi-epitaxial thin films using single crystal substrates

Traditionally, the most efficient strategy to induce a preferential orientation to a perovskite thin film is to grow the film on a single crystal of the perovskite structure type with matching lattice parameters that allow an epitaxial growth.[185] Additionally, epitaxial thin films allow the measurements of the in-plane tensor components of the bulk photovoltaic effect or the electro-optic effect that do not follow the direction of ferroelectric polarization.

Different single crystals, such as $DyScO_3$,[186, 187] $SrTiO_3$,[188] LSAT,[189] are typically used to grow $BiFeO_3$. However, most of the crystals are perovskites with high dielectric permittivity, e.g., $SrTiO_3$ shows $\epsilon_r = 10^2 - 10^3$. In IDE geometry, a substrate with high permittivity would create a high displacement current that will not allow the study of ferroelectric switching in the perovskite. Between the perovskites that are traditionally used to grow $BiFeO_3$, $LaAlO_3$ show one of the lowest dielectric permittivities, $\epsilon_r = 20$,[190] which is in the same order of magnitude as other substrates that are typically used in interdigitated electrode system, e.g., MgO, $\epsilon_r = 10$, Al_2O_3, $\epsilon_r = 10$. The lattice parameter misfit between $LaAlO_3$ and $BiFeO_3$ is 4.3%. In solution-processed films, epitaxial strain relaxation through the forma-

tion of dislocation or grains is expected. Consequently, the growth of $BiFeO_3$ on single crystal $LaAlO_3$ was attempted. Solution-processed $BiFeO_3$ were fabricated on $(100)_{pc}$ $LaAlO_3$ substrates following the procedure described in Section 3.1.1.

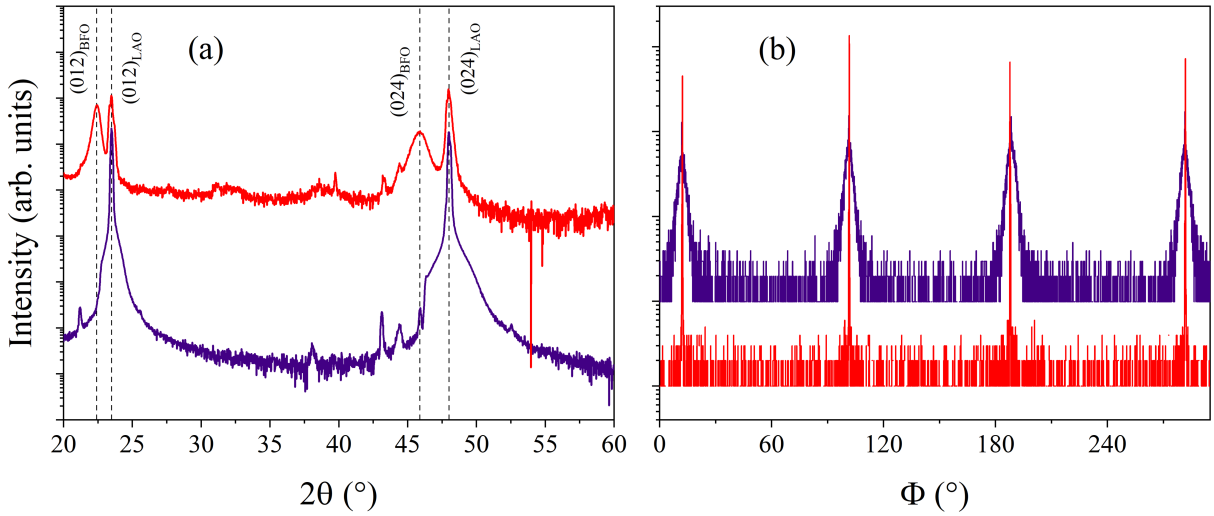

Figure 4.13: (a)$\theta/2\theta$ scans of the BFO/LAO (red) and LAO (blue) structures. (b) Φ scan of the (104) reflections of BFO (blue) and LAO (red) in the BFO/LAO structure.

Figure 4.13 (a) shows the $\theta/2\theta$ scan of a 50 nm $BiFeO_3$ film deposited on $LaAlO_3$. The films show perfect out-of-plane orientation towards the [012] direction, [100] in pseudocubic notation. The in-plane texture of the film was analyzed by performing Φ scans of the (104) reflection of $BiFeO_3$ with respect to the (104) reflections of $LaAlO_3$. The Φ scans are displayed in Figure 4.13 (b). Four peaks separated by 90° indicate the in-plane texture of the film. The broadening of the (104) reflections in $BiFeO_3$ indicates lower film crystalline quality than $LaAlO_3$. These results give the following epitaxial relations: (100)pc $BiFeO_3$||(100)pc $LaAlO_3$.

Figure 4.14 shows the AFM surface topography of the film. The images indicate the presence of pores in the microstructure, indicating incomplete pyrolysis of the organics within the pyrolysis step. In contrast to the films deposited on other substrates, the deposition of the film on a single crystal substrate may reduce the crystallization temperature of the film, resulting in an overlap between the complete pyrolysis of the film and the crystallization of the film. Besides, a closer look at the microstructure reveals the formation of grains, indicating that, despite the in-plane texture of the film, different in-plane oriented grains are formed.

Further optimization of the growth of solution-processed $BiFeO_3$ films on single crystalline substrates is needed to achieve high-quality films. The optimization of the deposition parameters as well as the electrical characterization of the films was not feasible during this thesis due to time constraints. Nonetheless,

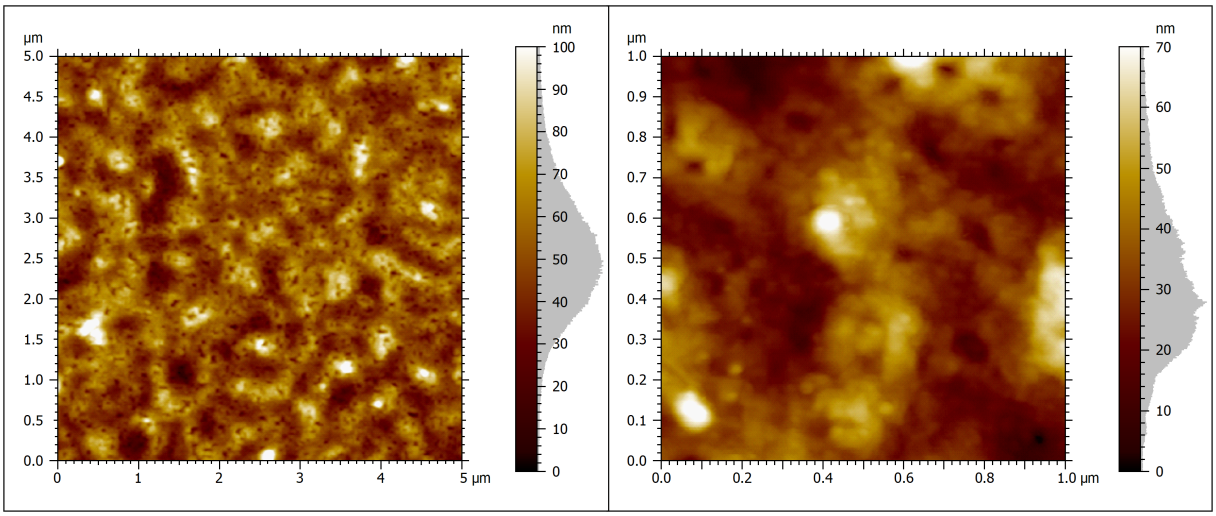

Figure 4.14: Topography AFM images of a solution-processed $BiFeO_3$ film on $LaAlO_3$ showing a porous microstructure.

the fabrication of epitaxial oxide perovskites using solution-deposition methods was further investigated during this thesis on the example of $PbZrO_3$. The detailed fabrication and characterization of epitaxial $PbZrO_3$ by CSD are discussed in Appendix A.

4.3 Influence of doping in the charge transport properties

As discussed in Section 2.4.1, the doping of $BiFeO_3$ with Mn^{x+} and Ti^{4+} substantially reduces the leakage properties in polycrystalline $BiFeO_3$. However, no systematic study on the influence of Mn^{x+} and Ti^{4+} doping in the low field and high field charge transport properties can be found in the literature. Consequently, the influence of doping on the ferroelectric switching and the charge transport properties was studied both in MIM and IDE configuration.

As outlined in Section 3.1.2, in MIM configuration the field is applied out-of-plane while in IDE configuration the field is applied in-plane. Several differences have to be taken into account:

1. In sol-gel films the formation of out-of-plane chemical gradients is common due to the volatility of some elements that leads to the formation of dissimilar interfaces.[191]

2. The bottom and top electrodes are different, during crystallization the bottom electrode is exposed to high temperatures that can lead to the formation of secondary phases in the interface, such as BiPt or PbPt alloys,[192] while the top electrode is not exposed to the high crystallization temperatures.

3. Texture may play a role in the charge transport mechanism. In MIM, charge transport is mainly along the (100) direction, whereas in IDE, it is a random combination of all orientations.

In that regard, even if the MIM configuration is more interesting for most applications, the complexity induced by the differences stated above makes the IDE configuration simpler to understand the intrinsic charge transport properties of the material.

Polycrystalline $BiFeO_3$ thin films were prepared by chemical solution deposition methods as described in Section 3.1.1. Four $BiFeO_3$ precursor solutions were prepared: $BiFeO_3$ (BFO), $BiFe_{0.95}Mn_{0.05}O_3$ (BFMO), $BiFe_{0.98}Ti_{0.02}O_3$ (BFTO), and $BiFe_{0.93}Mn_{0.05}Ti_{0.02}O_3$ (BFMTO). For the MIM structures, the samples were deposited on platinized silicon substrates. For the IDE structures, the samples were deposited on fused silica substrates.

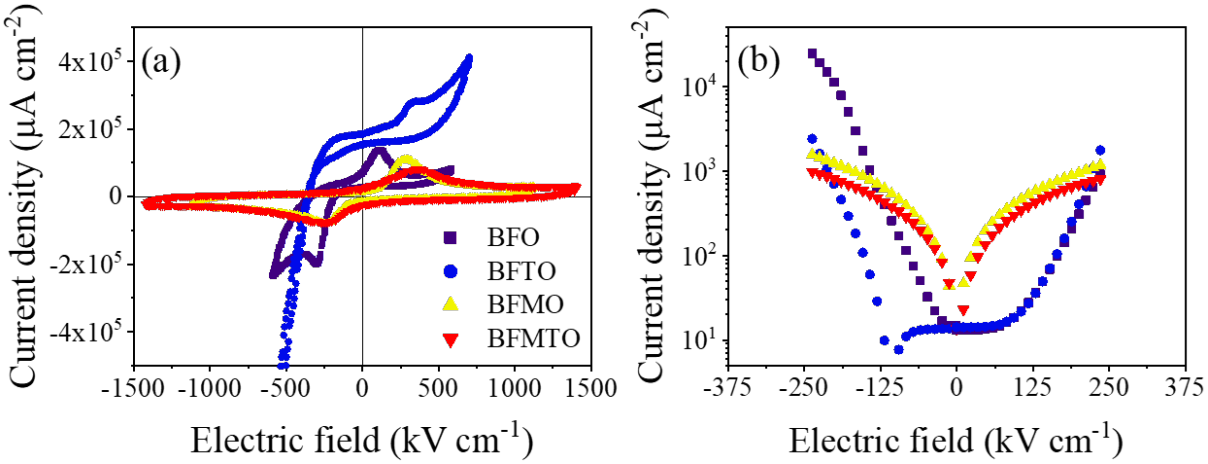

Figure 4.15: (a) j(E) transient loops recorded at 5 kHz and (b) DC j(E) leakage current measurement under different doping conditions. The measurements were performed in MIM capacitors.

The transient current density j(E) loops and the DC j(E) curves of 200 nm-thick $BiFeO_3$ films in MIM configuration were recorded for the four doping concentrations as depicted in Figure 4.15. The transient current density j(E) loops in Figure 4.15 (a) display a reduction of the high field conductivity in the BFMO and BFMTO systems compared to BFO and BFTO. The coercive field (E_c) also increases with the addition of Mn^{x+} or Ti^{4+}, as observed in the shift of the switching current peaks. The BFO and BFTO regularly broke down at cycling voltages higher than 750 kV cm^{-1}.

The asymmetry between the positive and negative sides in BFO and BFTO highlights the accumulation of defective layers at the interface, which makes the separation between the intrinsic material properties and interface effects difficult. The low leakage currents at high fields in the BFMTO system allow for an efficient poling of the film, which is required to exploit its bulk photovoltaic and linear electro-optical properties.

The picture is different for the low field leakage properties as reflected in the DC j(E) curves in Figure 4.15 (b). At low electric fields, the conductivity in BFO and BFTO is lower than in BFMO and BFMTO. However, the leakage curves in BFO and BFTO quickly outpace the BFMO and BFMTO above 100 kV cm^{-1}. On the other hand, a linear increase (ohmic behavior) is observed in BFMO and BFMTO, suggesting a change in the conduction mechanism when Mn^{x+} is introduced in the system.

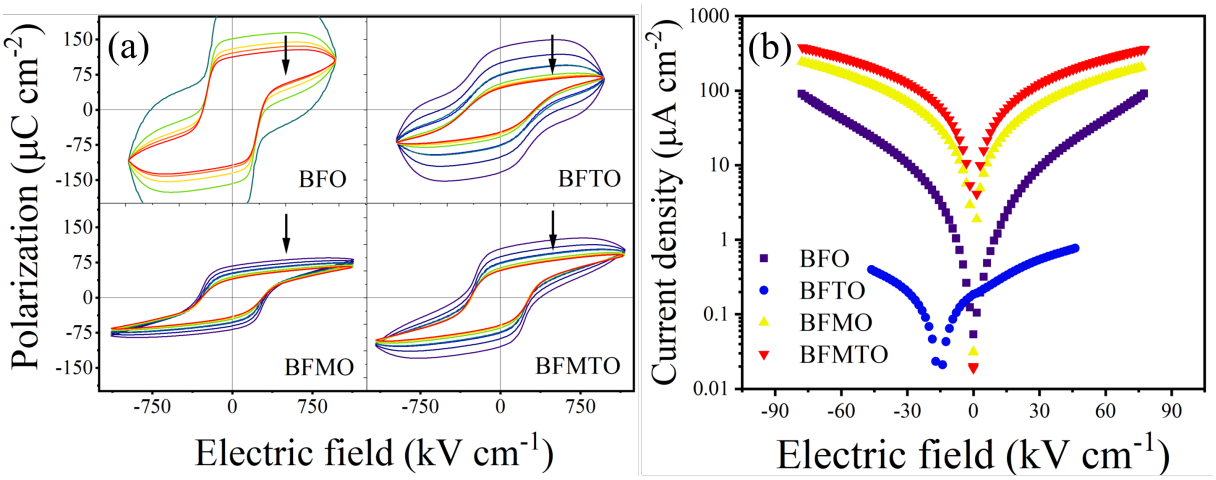

Figure 4.16: (a) Frequency-dependent P(E) loops and (b) DC j(E) leakage current measurements of films with different dopants deposited on fused silica. The measurement was performed using IDE capacitors. The arrows in (a) indicate increasing frequency.

To separate the contributions that arise from interface effects, the same analysis was performed in IDE configuration. The P(E) loops at different cycling frequencies recorded for different doping configurations are shown in Figure 4.16 (a). The high conductivity at high field in the BFO system leads to a strong contribution of leakage to the measured polarization, even at high frequencies. The addition of 2% Ti^{4+} doping reduces the high-field leakage current contribution at high frequency, but leaky polarization hysteresis loops remain at low frequency. Both BFMO and BFMTO show reduced leakage currents in the whole studied frequency range, supporting the use of a co-doped system to achieve a high degree of poling. Both the addition of Ti^{4+} and Mn^{x+} reduce the high field conductivity. The situation is different in the DC density-electric field characteristics. (Figure 4.16 (b)) The measurements were restricted to 90 kV cm^{-1} due to the breakdown of the capacitor at higher DC electric fields. When Mn^{x+} is introduced in the system, the low field conductivity increases. Moreover, the j-E behaviors shift from an exponential increase in BFO to an ohmic behavior when Mn^{x+} is introduced, suggesting a change in the conduction mechanism of the film. On the other hand, Ti^{4+} reduces the conductivity of BFO both at low field and at high field. A clear influence of the doping on the charge transport properties of $BiFeO_3$ is evidenced by the electrical measurements.

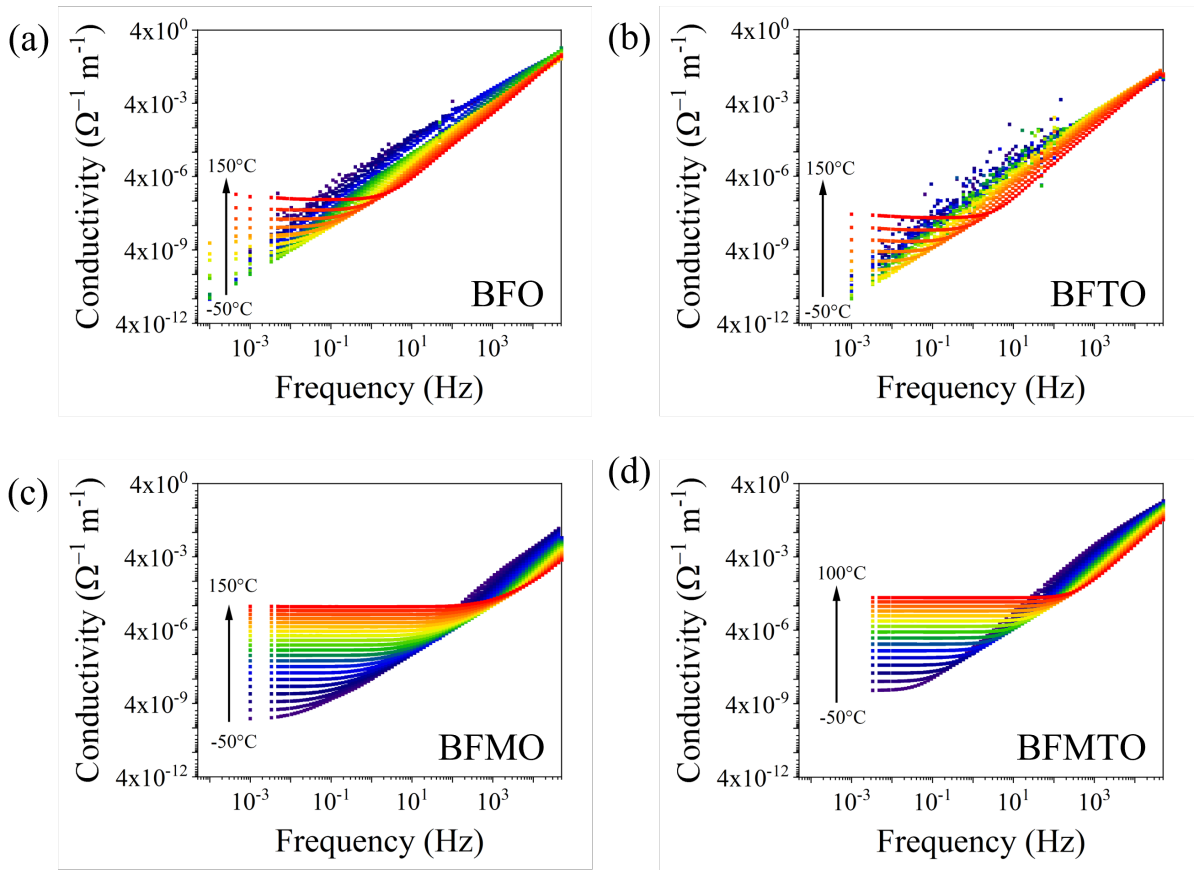

Figure 4.17: AC conductivity as a function of frequency for temperatures from −50 °C to 150 °C of the (a) BFO, (b) BFTO, (c) BFMO and (d) BFMTO IDE capacitors. The arrows indicate increasing temperature.

To better understand the mechanism behind this improvement, dielectric spectroscopy studies were carried out on the IDE capacitors. AC conductivity as a function of frequency plots in a wide range of temperatures is seen in Figure 4.17 (a)-(d). At low frequencies the samples exhibit a resistor behavior, the conductivity does not depend on the frequency, while at high frequencies the samples show a capacitor behavior as described by:

$$\sigma = \sigma_{DC} + B\omega^n, \tag{4.1}$$

where σ_{DC} is the conductivity under constant field, and $B\omega^n$ express the conductivity under alternating field. B is a constant for a particular temperature, and n defines an exponent subjected to temperature and frequency.

The conductivity in the Mn-doped $BiFeO_3$ at room temperature is two orders of magnitude larger than in BFO. The conductivity in BFTO is one order of magnitude lower than in BFO, in agreement with the DC j(E) curves. (Figure 4.16) The low field conductivity as a function of doping follows $\sigma_{\text{BFTO}} < \sigma_{\text{BFO}} < \sigma_{\text{BFMO}} \leq \sigma_{\text{BFMTO}}$.

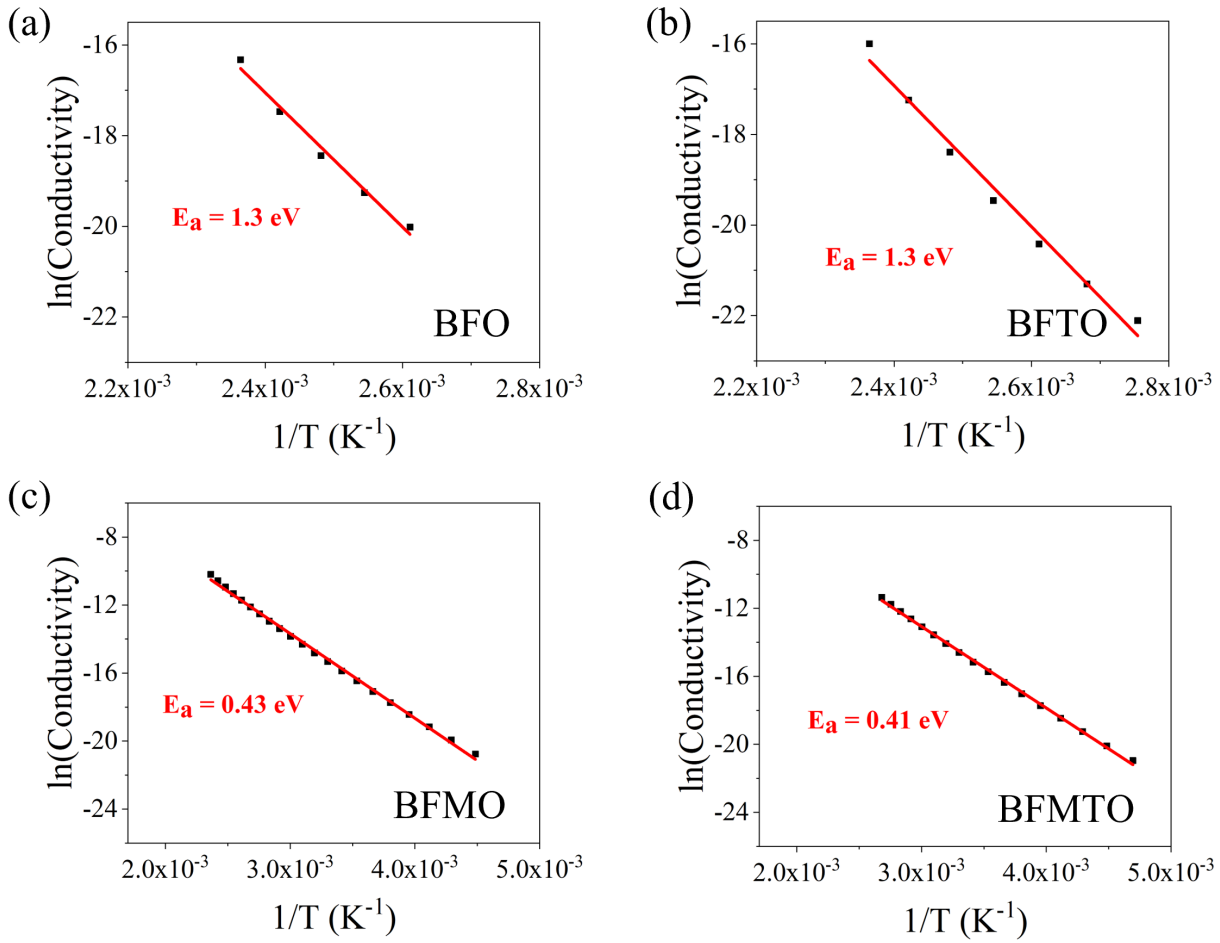

Figure 4.18: Arrhenius plots of the frequency independent AC conductivity (σ_{DC}) vs temperature of the (a) BFO, (b) BFTO, (c) BFMO, and (d) BFMTO IDE capacitors. The point represents the experimentally measured conductivity values while the lines display the linear fit following Equation 4.2.

The influence of doping in the predominant charge transport mechanism at low fields can be extracted from the Arrhenius plots of the frequency-independent conductivity and temperature. The σ_{DC} can be described by a thermally activated behavior following an Arrhenius function:

$$\sigma_{DC} = \sigma_0 \exp \frac{-E_a}{k_B T} \tag{4.2}$$

where k_B is Boltzmann's constant, σ_0 is the attempt conductivity, which represents the temperature-independent conductivity, and E_a is the activation energy. As indicated by Equation 4.2, E_a can be extracted from the linear fit of the natural logarithm of the frequency independent AC conductivity against 1/T.

The plots are shown in Figure 4.18. Unfortunately, for BFO and BFTO the frequency-independent conductivity region can only be accessed at high temperatures, leading to a reduced number of data points available for the Arrhenius plot. At low temperatures, the frequency-independent term is drowned out by the frequency-dependent term. The conductivity data show temperature ranges that can be fitted by a straight line. The extracted activation energy values, together with the DC conductivity values at 100 °C are summarized in Table 4.2.

	E_a (eV)	σ_{DC} ($\Omega^{-1}m^{-1}$)
$BiFeO_3$	1.3 ± 0.2	$(7.5 \pm 0.5) \times 10^{-9}$
$BiFe_{0.98}Ti_{0.02}O_3$	1.3 ± 0.3	$(5.5 \pm 0.5) \times 10^{-10}$
$BiFe_{0.95}Mn_{0.05}O_3$	0.4 ± 0.1	$(5.5 \pm 0.5) \times 10^{-6}$
$BiFe_{0.93}Mn_{0.05}Ti_{0.02}O_3$	0.4 ± 0.1	$(8.5 \pm 0.5) \times 10^{-5}$

Table 4.2: Extracted E_a and σ_{DC} at 100 °C for the BFO, BFTO, BFMO and BFMTO IDE capacitors.

The E_a values are similar in BFO and BFTO systems. However, when Mn^{x+} is added, the E_a is drastically reduced, indicating a different charge transport mechanism. In BFO, the high concentration of V_O is responsible for the high conductivity.[193, 194] During the crystallization step at high temperatures (e.g. 600 °C), oxygen loss in the film is accelerated, leading to the formation of oxygen vacancies. This process can be described by the Kröger-Vink notation as follows:

$$O_O^x \rightarrow V_O + \frac{1}{2}O_2, \tag{4.3}$$

where O_O^x is O^{2-} on the O site. Conduction electrons can be released from neutralized oxygen vacancies by a first ionization and a second ionization step as follows:

$$V_O \rightarrow V_O^{\cdot} + e' \rightarrow V_O^{\cdot\cdot} + 2e'. \tag{4.4}$$

The E_a values for BFO and BFTO correlate with the activation energy for oxygen vacancy (V_O) migration.[111, 195] At low fields, they are relatively immobile, leading to low conductivity at low electric fields, but at high electric fields, they become delocalized, causing high conductivity. In the case of BFTO, the lower conductivity can be attributed to the introduction of an donor dopant. Ti^{4+} lowers the concentration of $V_O^{\cdot\cdot}$ to compensate for the charge balance according to:

$$4TiO_2 + 2V_O^{\cdot\cdot} \rightarrow 4Ti_{Fe}^{\cdot} + 2O_O^{x} + 3O_2. \tag{4.5}$$

The reduction of E_a in the BFMO and BFMTO systems suggests a change in the charge transport mechanism. First-principles calculations show that Mn^{x+} introduces intra-bandgap defects whose energy depends on the oxidation state of Mn^{x+}. The calculated energy difference between the valence band and the Mn^{2+} levels is 0.6 eV and between the Mn^{2+} and the Mn^{3+} is 0.3 eV.[196]

The low energy difference between these energy levels and the reduction of the E_a suggests that the conductivity in the BFMO and BFMTO may be dominated by hole injection in the valence band or electron hopping between the Mn^{3+} and Mn^{2+} levels. At low field, these are more easily excited than the V_O, leading to high low-field dark conductivity. Additionally, first-principle calculations show that Mn^{3+} can act as an effective trap for V_O,[118] explaining the reduced high-field conductivity in the BFMO and BFMTO systems.

4.4 Transparent embedded interdigitated electrodes

Ferroelectric properties rivaling those obtained in high-quality epitaxial thin films can be achieved by careful tuning of the microstructure using a $PbTiO_3$ seed layer and precise doping with Ti^{4+} and Mn^{x+}. Particularly, the high-quality properties obtained in the BFMTO system with IDE configuration will be used as a reference system to study the bulk photovoltaic effect and the electro-optic effect in polycrystalline $BiFeO_3$.

However, the system shows several limitations that could negatively impact some applications:

1. The epoxy-based encapsulating (SU8) layer prevents electric arcs between the IDEs at switching electric fields. This SU8 layer cannot withstand temperatures higher than 300 °C, limiting the temperature application range of the device.[197]

2. The devices show poor fatigue properties: after 10^4 switching cycles, electrical arcs between the IDE fingers due to the deterioration of the SU8 layer during switching or the breakdown of the material lead to the breakdown of the devices. This limits applications that require continuous switching of the material.

3. Current applications of ferroelectric oxides require transparency, e.g., the integration of haptic devices in screens or the integration of electro-optic windows, which involves substituting the Pt electrodes with transparent electrodes.

To increase the application temperature range of the devices, embedded IDEs were developed. In this configuration, IDEs were patterned on an insulating substrate by lift-off photolithography and Pt sputtering. Then, $BiFeO_3$ was deposited on the IDE structure. The IDEs are sandwiched between the substrate (with higher permittivity than air) and the $BiFeO_3$ film. Therefore, effective switching of the $BiFeO_3$ was possible in the whole temperature range, only limited by the increased leakage currents at high temperatures. However, the large difference between the TEC of the metal and $BiFeO_3$ induces high strain in the IDEs during the high-temperature annealing that typically results in cracked electrodes with similar breakdown properties of the standard IDE devices as well as the same lack of transparency.

In ferroelectric oxides, the accumulation of oxygen vacancies at the ferroelectric-metal interface is associated with the pinning of domain walls, and phase decomposition that prevents the switching of the domains and leads to material breakdown.[30, 198] To overcome these limitations, it is widely accepted that conductive oxides act as an efficient sink for oxygen vacancies that emigrate from the ferroelectric oxide upon switching, suppressing oxygen vacancy accumulation at the interface and leading to increased fatigue resistance. Several metallic conductive oxides such as $LaNiO_3$[199] or LSMO[167] are typically used as oxide electrodes to reduce ferroelectric fatigue. However, these oxides are not transparent.

An alternative to these metallic oxides is the use of degenerate semiconductors, where the high doping levels lead to high conductivity while being transparent (Transparent conductive oxides, TCOs).[200] Typical TCOs often used for transparent devices are Al:ZnO,[201] In:SnO_2[202] or F:SnO_2.[203] However, the transparency and conductivity of the material are very sensitive to the annealing conditions, most of them are not good conductors at temperatures above 200 °C.[204] The most temperature-resistant TCO is F:SnO_2 (FTO), often used as a back contact for solar cells.[205] Good conductivity and transparency have been achieved after annealing around 600 °C,[206] very close to the crystallization temperature of the process used for $BiFeO_3$.

FTO IDEs were patterned by lift-off photolithography and sputtering on an insulating substrate. In this configuration, sapphire was chosen as an insulating substrate because its TEC is very similar to the TEC of $BiFeO_3$ and FTO. When a substrate such as fused silica, with very low TEC, is used, the high internal

stresses between the substrate, IDEs, and film lead to cracking of the structure when large structures are patterned. Special attention needs to be paid to the lift-off process, which requires an ultra-sonification treatment to lift-off the devices. Then, FTO films were grown as described in Section 3.1.2. Then, $BiFeO_3$ was deposited according to the standard process described in Section 3.1.1.

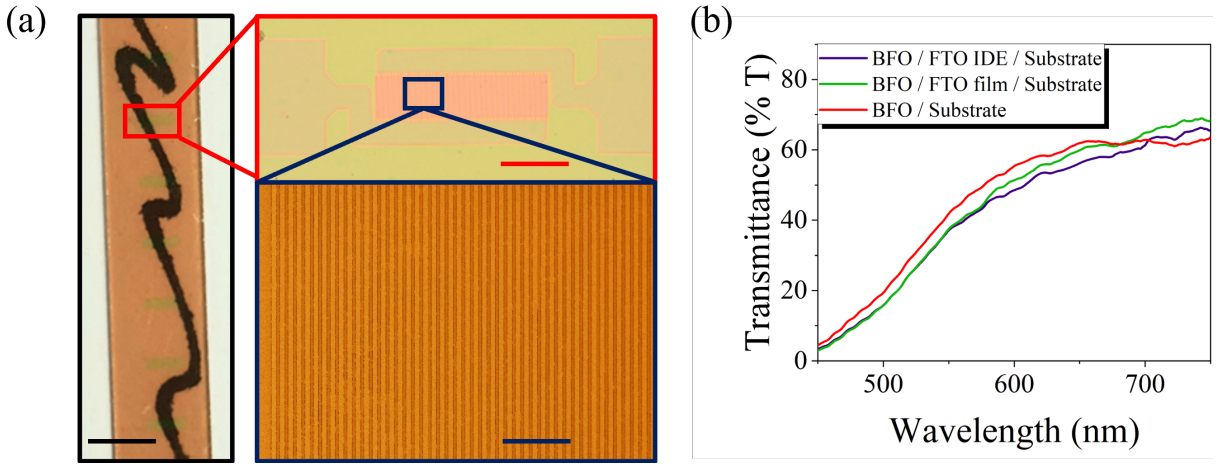

Figure 4.19: (a) Photograph and optical microscope micrographs of the transparent embedded FTO IDEs. The black line in the photograph was drawn below the sample. The black bar refers to 5 mm. The red bar refers to 500 µm. The blue bar refers to 100 µm. (b) Local transmittance spectra recorded at different regions of the device.

A detail of the final device deposited on sapphire is illustrated in Figure 4.19 (a). Upon a closer look, small shades can be observed where the IDE structure was patterned. The orange color is produced by the $BiFeO_3$ film. To quantify the transparency of the embedded FTO IDEs, local transmittance spectra were recorded at different regions of the device. (Figure 4.19 (b)) The similar spectra between the BFO/Substrate and the BFO/FTO IDE/Substrate regions highlight that the drop in transmittance is produced by the $BiFeO_3$ film and not by the embedded FTO IDE. The substitution of $BiFeO_3$ by a more transparent ferroelectric, such as PZT, could dramatically enhance the transmittance of the device.

The deposition of $BiFeO_3$ on the IDEs leads to the formation of small bumps on the fingers and valleys between the finger. To quantify the roughness of the $BiFeO_3$, the topography of a previously poled film was studied by AFM. The topography image in Figure 4.20 shows that the fingers create a 20 nm bump. The deposition of thicker films would result in a reduction of these bumps. In addition, in-plane DART PFM images of poled films show a brighter contrast between the fingers, which indicates that the field distribution is confined between the fingers. The opposite phase contrast in each direction of the finger indicates the polarity of the poling. The embedded FTO IDEs allow for an efficient in-plane poling of the $BiFeO_3$.

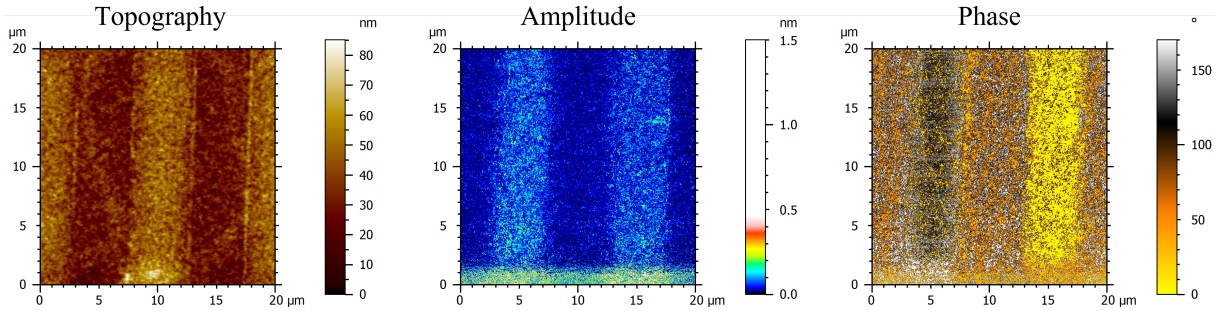

Figure 4.20: AFM and in-plane DART PFM images of the embedded FTO IDEs after ex-situ electrical poling. Electrical poling was performed using a two-step poling procedure. In a first step, the P(E) loops were woken-up using 10^3 bipolar triangular pulses at 1000 kV cm^{-1} and 1 kHz. Then, three unipolar triangular pulses using the same frequency and 1200 kV cm^{-1} were applied.

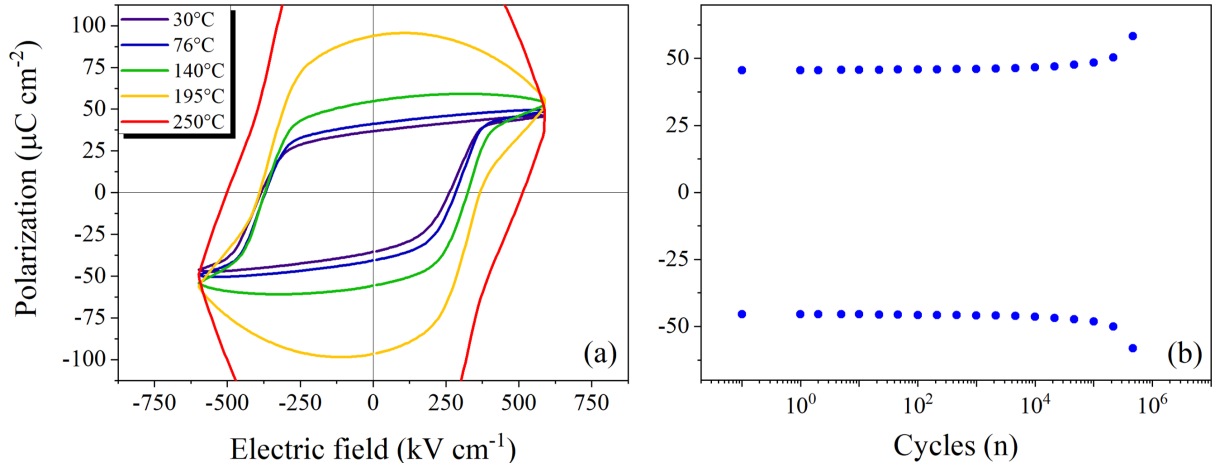

Figure 4.21: (a) Ferroelectric hysteresis loops of the embedded FTO IDEs on fused silica recorded at 1 kHz between 30 °C and 250 °C (b) Fatigue behavior up to 10^6 cycles and a frequency of 100 Hz at room temperature.

The device was exposed to temperatures as high as 600 °C without any detrimental effect on the ferroelectric properties, fatigue, or transparency. Figure 4.21 (a) shows the temperature-dependent ferroelectric hysteresis loops of the device. Low-leakage P(E) loops are obtained even at low frequencies (100 Hz). The measured remanent polarization assuming the same approximation as for classical IDEs was 40 µC cm^{-2}. The device shows excellent ferroelectric switching up to 140 °C. Even if the device remains operational at higher temperatures, the higher leakage currents of the ferroelectric film above 200 °C lead to rounded P(E) loops. Further optimization of the ferroelectric film or the substitution of the ferroelectric is needed to reduce the high-temperature leakage. Besides, the substitution of the Pt IDEs by the embedded FTO IDEs also results in a reduction of ferroelectric fatigue. The devices were able to sustain more than 10^6 switching cycles without breakdown.

The embedded FTO IDEs are an elegant solution to fabricate a temperature-resistant and transparent ferroelectric device with excellent ferroelectric properties and increased fatigue behavior. This device can be used for piezoelectric actuators such as haptic devices.[207] This device will be used in Section 6.3 to study the electro-optic properties $BiFeO_3$ under switching electric fields.

4.5 Outlook

In this chapter, $BiFeO_3$ films with excellent ferroelectric properties were prepared using low-cost solution processes. Highly $(100)_{pc}$-oriented films were obtained using seed layers. Particularly, the $PbTiO_3$ seed layer leads to a strong texture and outstanding ferroelectric properties. It could be argued that the use of Pb in the seed layer could be detrimental to lead-free applications. However, the lead content of a 200 nm-thick $BiFeO_3$ film lies below the EU limits for lead-free materials, which are fixed to less than 0.1% for electrical and electronic products.[208] Additionally, functional properties were demonstrated in photonic annealed $BiFeO_3$, as discussed in Appendix B.

The quasi-epitaxial growth of solution-processed $BiFeO_3$ films on $LaAlO_3$ is demonstrated. Further optimization is needed to obtain films with a quality that is comparable to those obtained by vacuum-based techniques. Some applications require single-crystal films, for example, waveguides in polycrystalline films, would be subjected to additional losses due to the scattering of light at the grain boundaries or the rough surfaces. In that context, the recent developments in silicon epitaxy could boost the integration of epitaxial solution-processed films on technology-oriented substrates, such as silicon. Strategies such as domain-matched epitaxy,[209] incorporating buffer layers such as TiN[210, 211] to overcome the large lattice parameter misfit between silicon and oxide perovskites or the use of $SrTiO_3$-buffered silicon substrates[212] could bridge the gap to use epitaxial solution-processed film for integrated silicon photonics.

The conductivity of $BiFeO_3$ films was engineered using Mn^{x+} and Ti^{4+} doping. Ti^{4+} reduces the conductivity by decreasing V_O concentration, and Mn^{x+} strongly modifies the dominating conduction mechanism in the films. The origin of this modification is only speculative at this point. X-ray absorption spectroscopy studies,[213] would allow for the determination of the oxidation state of manganese, titanium, and iron. Additionally, to unveil the majority carrier sign and concentration, temperature-dependent Hall measurements,[214] could be performed. Both techniques would help to understand the physical origin of the reduced leakage current in the doped films. However, the excellent ferroelectric properties obtained in the BFMTO films highlight that co-doping is a key strategy for ferroelectric switching applications.

The fabrication of embedded FTO-based IDE circumvents the limitations of standard IDEs. Fully transparent devices operating in a wide temperature range were prepared. Additionally, the use of oxide-based electrodes leads to excellent fatigue properties, with no electrical degradation up to 10^6 cycles.

These results provide a system to study the bulk photovoltaic and electro-optic effects in polycrystalline $BiFeO_3$ film and are the starting point of the physical investigations performed in the following chapters.

Chapter 5

Bulk photovoltaic effect in polycrystalline $BiFeO_3$ films

5.1 Motivation

The anomalous or bulk photovoltaic (BPV) effect in noncentrosymmetric materials allows for the generation of electrically switchable photovoltages that are not limited by the bandgap of the material.[2, 7] In contrast to an interface-driven photovoltaic (PV) effect, where the open-circuit voltage (V_{OC}) is limited by the quasi-Fermi energy level splitting,[38, 39] values of thousands of volts have been measured in homogeneous ferroelectric single crystals.[4] In the last decade, $BiFeO_3$ has received a strong focus as a prototype material to engineer the BPV response due to the high remanent polarization, low bandgap, and control of the conductivity through domain engineering.[10, 126] However, all the fundamental studies are focused on epitaxial single-crystal films. In low-cost polycrystalline materials, more suitable for applications, the photovoltaic response is typically dominated by interface effects such as the formation of Schottky barriers at the metal-ferroelectric interface.

In this chapter, co-planar interdigitated electrodes are used to measure the photovoltaic effect in polycrystalline $BiFeO_3$ thin films and demonstrate the observation of BPV charge transport fingerprints in a poled polycrystalline ferroelectric film. The role of Mn^{x+} and Ti^{4+} doping in the BPV effect is discussed. Additionally, the dependence of the BPV effect on strain is studied.

5.2 Origin of the photovoltaic effect in polycrystalline $BiFeO_3$

As discussed in Section 2.2, the separation between interface-driven PV effect and BPV can be a challenging task. The formation of Schottky diodes at the metal-ferroelectric interfaces with different barrier heights, ϕ_B, leads to an interface-driven light-induced charge transport.[44]

Two electrode geometries are available to measure the photovoltaic effect: metal-insulator-metal (MIM) capacitors and IDE. As discussed in Section 4.3, in MIM capacitors it is not possible to obtain fully symmetric structures: the top electrode and the bottom electrode are processed differently.[191] Therefore, to avoid interface effects in the charge transport properties of $BiFeO_3$, symmetrical co-planar IDE structures were proposed to characterize the BPV properties of polycrystalline $BiFeO_3$ films deposited on insulating substrates.

The devices were fabricated on HfO_2-buffered fused silica substrates. 5% Mn^{x+} and 2% Ti^{4+} co-doped $BiFeO_3$ films were chosen as a reference system due to the superior ferroelectric properties, as discussed in Section 4.3. Additionally, previous reports have demonstrated an increased absorption, driven by the addition of defect levels in the bandgap, upon doping with Mn^{x+} and Ti^{4+}.[129, 215] $PbTiO_3$ was used as a seed layer to obtain high-quality (100)-oriented films.[137] The thickness was kept constant at (200 ± 10) nm. To characterize the electrical and optoelectronic properties, IDEs were patterned as described in Section 3.1.2. The spacing between fingers used to study the light-induced charge transport is (2.5 ± 0.5) µm unless otherwise specified.

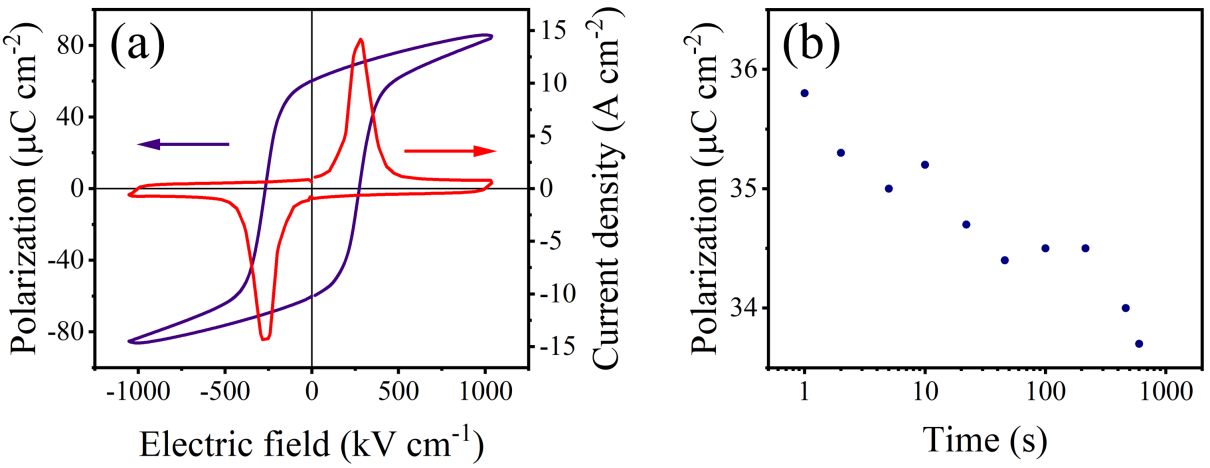

Figure 5.1: (a) Polarization hysteresis loops and switching current density curves and (b) evolution of the retained polarization with time of the 5% Mn^{x+} and 2% Ti^{4+} co-doped $BiFeO_3$ IDE capacitor.

In the pristine films, the polycrystalline microstructure leads to a random in-plane orientation of the ferroelectric domain. Therefore, poling is key to measuring a BPV current. A two-step poling procedure was used. In a first step, the P(E) loops were woken-up using 10^3 bipolar triangular pulses at 1000 kV cm^{-1}

and 1 kHz. Then, three unipolar triangular pulses using the same frequency and 1200 kV cm^{-1} were applied. As depicted in Figure 5.1 (a), dynamic hysteresis measurement of the films exhibit a P_r of (60 ± 2) μC cm^{-2} and a E_c of (270 ± 50) kV cm^{-1}. However, due to the formation of depolarizing fields between the grains and the internal stresses between ferroelastic domains, back-switching reduces the remaining polarization in the sample after poling. Retained polarization measurements shown in Figure 5.1 (b) reveal that the retained polarization in the sample is around (36 ± 2) μC cm^{-2} and decreases to (34 ± 2) μC cm^{-2} after 1000 s. No measurable back-switching is observed after illumination. Dielectric spectroscopy measurements discussed in Section 4.3 reveal a DC room temperature dark conductivity of 2×10^{-7} Ω^{-1} m^{-1}, comparable to the reported values of high-quality epitaxial films, in the order of 10^{-8} Ω^{-1} m^{-1} at 25 °C.[126]

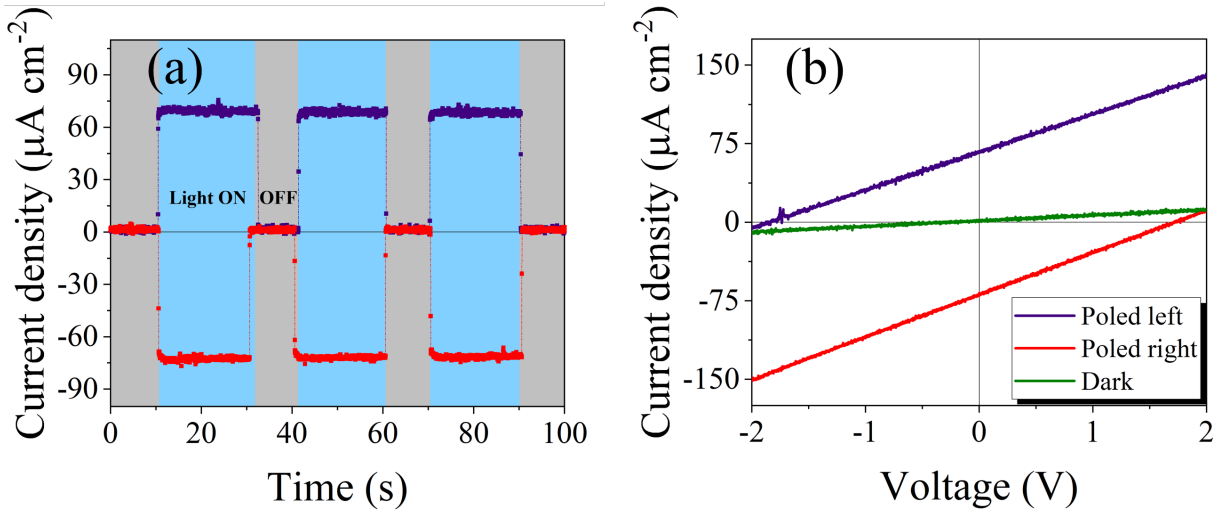

Figure 5.2: (a) j_{SC} values of the $BiFeO_3$ device in the dark and under illumination under two opposite poling directions. The change in the sign of j_{SC} shows the characteristic switchable photovoltaic effect. (b) j-V curve of the $BiFeO_3$ device in the dark and under illumination with different poling conditions. A 455 nm LED with an intensity of 0.48 W cm^{-2} was used to illuminate the device.

The optoelectronic characterization was performed as explained in Section 3.2.4. Figure 5.2 (a) shows the light ON/light OFF j_{SC} curves as a function of time with positive and negative poling. Under illumination, a steady photocurrent is produced. The device shows a perfectly symmetrical switchable photocurrent when the direction of the ferroelectric polarization is reversed. The photocurrent is steady during 1000 s with a slight decrease of 2%, expected from the slight reduction in the retained polarization over time.

The j-V curves in the dark and under illumination for both poling conditions are displayed in Figure 5.2 (b). No change in the dark j-V characteristics is observed under different poling conditions. A dark conductivity (σ_d) of 2×10^{-7} Ω^{-1} m^{-1} can be calculated from the slope of the dark j-V curve. This value is similar to that obtained by dielectric spectroscopy, as described in Section 4.3. Under illumination, perfectly switch-

able j-V curves are measured. The linear relation suggests the absence of interface-driven PV contribution. The device show and open-circuit voltage (V_{OC}) i.e., x-intercept, of 1.9 V and a j_{SC} i.e., y-intercept, of $(70 \pm 2)\ \mu Acm^{-2}$. The photoconductivity (σ_{ph}) i.e., slope of the j-V curve, under this light intensity, has a value of $1.6 \times 10^{-6}\ \Omega^{-1}\ m^{-1}$, one order of magnitude larger than σ_d.

As discussed in Section 2.2, the most distinctive fingerprint of a BPV charge transport mechanism is the reversal of the direction of the photocurrent with light polarization for a specific crystallographic orientation. This can only be observed in ferroelectric crystals where β_{331}, in which the photocurrent direction is perpendicular to the ferroelectric polarization and the light polarization, and β_{131}, in which the current direction and the light polarization are perpendicular to the ferroelectric polarization, show opposite sign. In IDE devices, the photocurrent can only be measured in the direction of the ferroelectric polarization. With this restriction, four conditions must be met to attribute the effect to a BPV charge transport mechanism: reversal of the direction of j_{SC} with reversal of the ferroelectric polarization; linear dependence of j_{SC} on the light intensity; linear dependence of V_{OC} on the spacing between electrodes; tensorial nature of j_{SC} with the light polarization.

The first indication of a BPV charge transport mechanism is illustrated in the symmetric switchable j_{SC} and the lack of rectification behavior in the j-V characteristic. The dependence of the j-V curves on the light intensity, for light intensities values where $\sigma_d \ll \sigma_{ph}$, is shown in Figure 5.3 (a). j_{SC} and σ_{ph} increase linearly with intensity as indicated in Figure 5.3 (b). In contrast, V_{OC} remains constant with light intensity. At lower light intensities, when σ_{ph} is comparable to σ_d, both the j_{SC} and V_{OC} depend on the light intensity. This is expected for a BPV charge transport mechanism.

Figure 5.3 (c) shows the influence of electrode spacing in the j-V characteristics. The lower values of j_{SC} and V_{OC} originate from the lower poling field compared to Figure 5.2 (b): due to limitations of the voltage source used in this study, (400 V) the devices discussed in Figure 5.3 (c) were poled at $900\ kV\ cm^{-1}$, instead of $1200\ kV\ cm^{-1}$. The linear increase of V_{OC} with the electrode spacing agrees with a BPV charge transport mechanism. While j_{SC} should remain constant with the electrode spacing, a slight increase of j_{SC} with electrode spacing is observed. This increase can be associated with a possible influence of the out-of-plane poling at the edges of the IDE fingers due to the curvature of the electric field during poling.

The tensorial nature of j_{SC} with the light polarization is demonstrated in Figure 5.3 (d). In IDE geometry, two components of the BPV tensor can be calculated: β_{311}, in which the light polarization is perpendicular to the ferroelectric polarization and the current direction, and β_{333} where the light polarization, the ferroelectric polarization, and the current direction are aligned. j_{SC} shows a pronounced variation of 5% with light polarization. However, j_{SC} does not show any directional change upon light polarization. At perpendicular light incidence, only two reasons can account for the changes in the photocurrent: the anisotropy

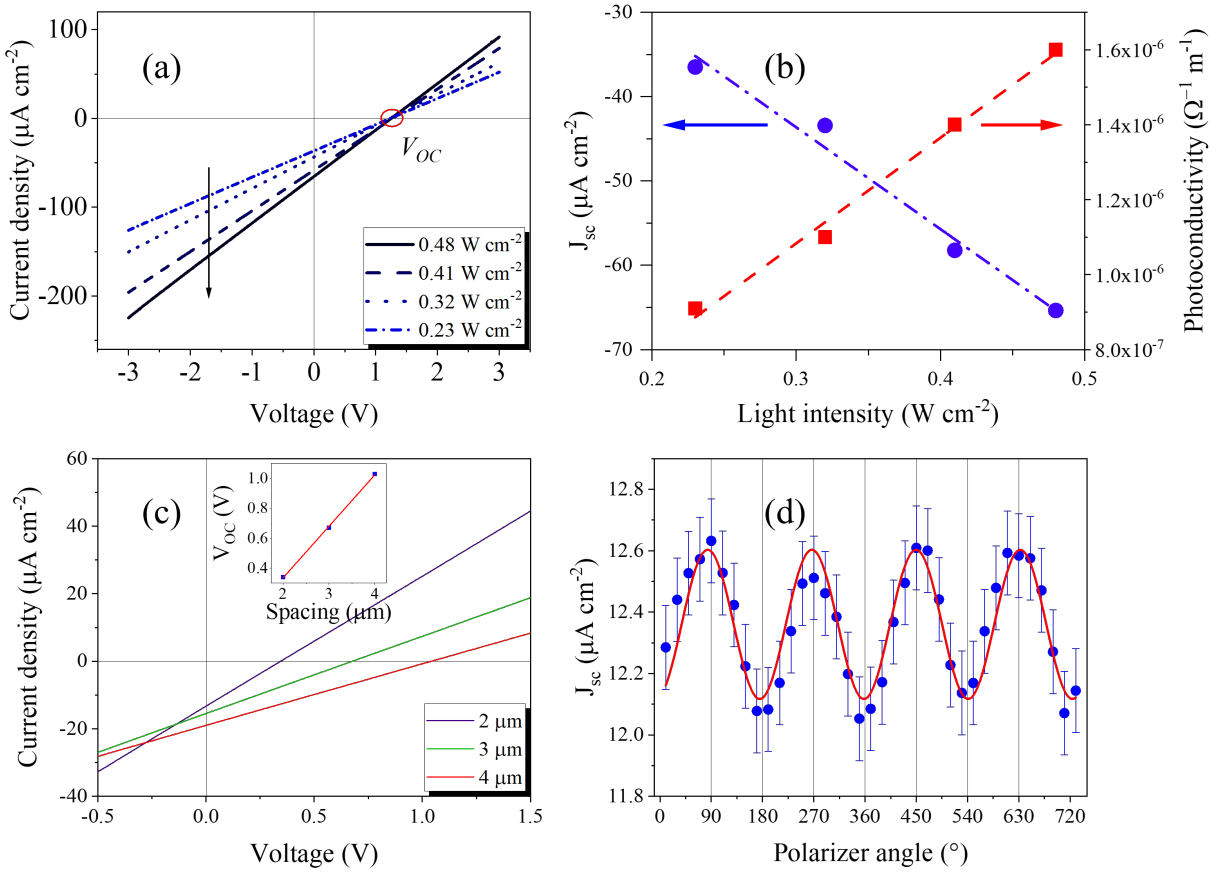

Figure 5.3: (a) j-V curves of the $BiFeO_3$ device with increasing light intensities. The arrow indicates increasing intensity. (b) j_{SC} and $\sigma_p h$ at different light intensities. (c) j-V curves for different electrode spacing. Inset shows the linear dependence of V_{OC} with electrode spacing (d) Light-polarization-dependent j_{SC} at a light intensity of 0.1 W cm^{-2}. 0° denotes the light electric field direction parallel to the poling direction.

of the absorption coefficient (α) after poling or the anisotropy of the hopping of non-thermalized carriers. The anisotropy of the j_{SC} may also be observed in interface-driven PV systems where absorbers with highly anisotropic α are used. However, the four conditions for a BPV charge transport are fulfilled (see Section 2.2.2, showing evidence that the charge transport is dominated by the BPV.

The maximum j_{SC} is measured when the light electric field direction is aligned perpendicular to the direction of the ferroelectric domain structure: $\beta_{311} > \beta_{333}$. This observation agrees with the reported BPV tensors in epitaxial Mn-doped $BiFeO_3$ thin film. [128, 196] The obtained tensor values are 30% of the values typically obtained in epitaxial thin films. Several reasons can account for the lower β_{311} and β_{333} values. First, the incomplete poling of the domains in polycrystalline materials can reduce the degree of

Dark Conductivity (σ_d)	$2 \times 10^{-7}\,\Omega^{-1}\,m^{-1}$
Normalized photoconductivity (at 455 nm)	$3.3 \times 10^{-8}\,\Omega^{-1}\,W^{-1}\,cm$
β_{333}	$0.53 \times 10^{-5}\,V^{-1}$
β_{311}	$0.55 \times 10^{-5}\,V^{-1}$

Table 5.1: Values of dark conductivity, normalized photoconductivity, and BPV tensor values of $BiFeO_3$ deposited on fused silica at 25 °C.

noncentrosymmetry: the retained polarization is about 50% of the maximum remanent polarization for a $(100)_{pc}$-oriented $BiFeO_3$ thin film. Also, grain boundaries can act as scattering and recombination centers for photo-generated non-thermalized carriers.

5.3 Doping and light-induced charge transport properties

In the previous section, 5% Mn^{x+} and 2% Ti^{4+} co-doped $BiFeO_3$ films were used as a model to show evidence of the BPV effect in polycrystalline films. However, as discussed by [128, 196], doping has a key role in the BPV effect of $BiFeO_3$. To compare the influence of doping on the BPV characteristics, the j-V characteristics of the BFO, BFTO and BFMO systems were studied.

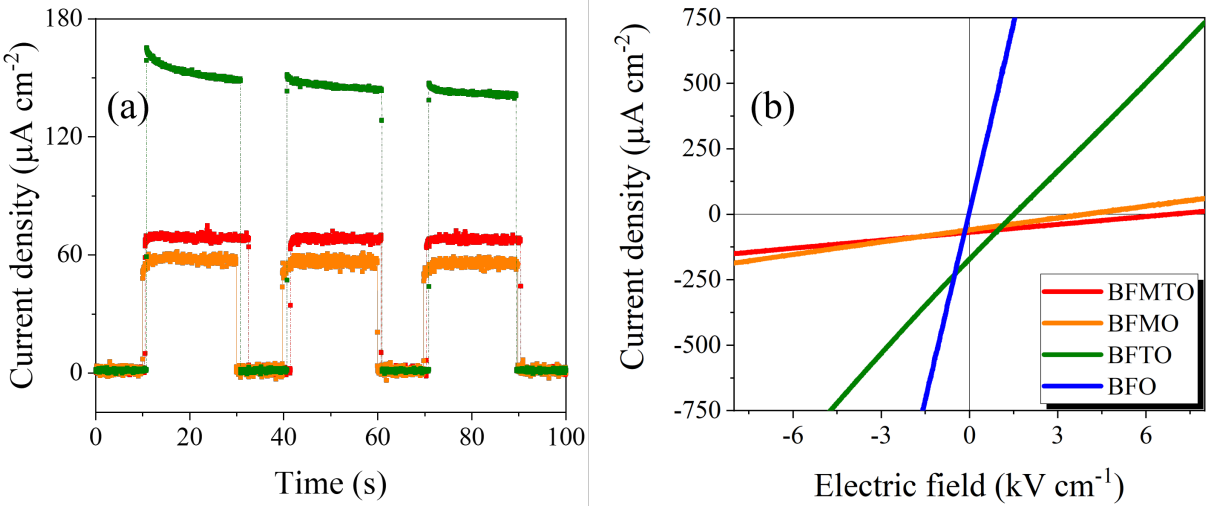

Figure 5.4: (a) j_{SC} values of the $BiFeO_3$ device with different doping conditions in the dark and under illumination.(b) Current density vs electric field curves under light for $BiFeO_3$ IDE capacitors with different doping conditions. A 455 nm LED with an intensity of 0.48 W cm^{-2} was used to illuminate the device.

Figure 5.4 shows the ON/OFF j_{SC} and j-E curves under light for the films with different doping. The BFO system shows the highest photoconductivity but does not show a measurable j_{SC}. The high conductivity may be associated with the light-induced ionization of the V_O levels. The lack of j_{SC} may be explained by the larger bandgap of $BiFeO_3$, which prevents the formation of non-thermalized carriers upon illumination with 455 nm light. (2.72 eV) Wavelength-dependent studies are required to unveil the lack of j_{SC} in the un-doped system. The BFTO system shows lower photoconductivity values than BFO. This can be explained by the reduction of the concentration of V_O as discussed in Section 4.3. Additionally, it shows the highest j_{SC}, but the high photoconductivity reduces the E_{OC}.

The BFMO and the BFMTO systems show lower j_{SC}, but also lower σ_{ph} resulting in high E_{OC}. As discussed in Section 4.3, Mn^{x+} doping plays a key role in the charge transport properties of $BiFeO_3$. Doping with Mn^{x+} introduces intra-bandgap states that modify the dominant charge transport mechanism to hole injection in the valence band or electron hopping between the Mn^{3+} and Mn^{2+} levels. The reduction in the j_{SC} and σ_{ph} may be explained by considering that the Mn^{x+} levels immediately trap the charges excited from the V_O, reducing the photoconductivity.

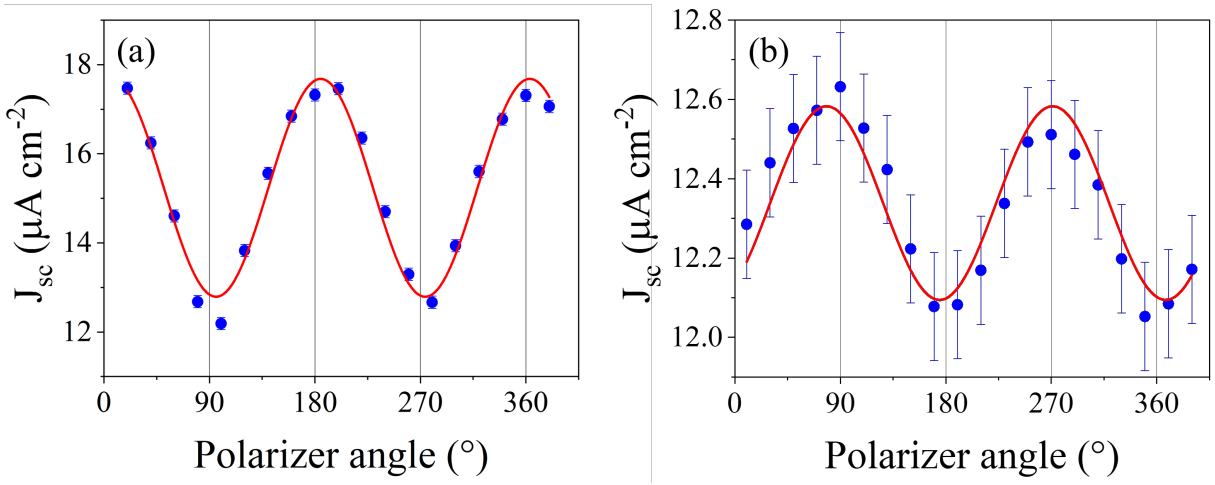

Figure 5.5: Light-polarization dependent photocurrent in the (a) BFTO and the (b) BFMTO IDE capacitors. The points represent the experimentally measured j_{SC} values, while the lines display a sinusoidal fit.

Additionally, as previously discussed by Matsuo et al.[196], the addition of Mn^{x+} has a strong impact on the sign of the BPV tensors, which supports the strong influence of Mn^{x+} doping in the microscopic BPV mechanism of BFO. Light-polarization dependent j_{SC} measurements of the BFTO and BFMTO are depicted in Figure 5.5. They reveal a stronger anisotropy of the j_{SC} in the BFTO, with changes of up to 50% in the j_{SC} against the 5% change observed in the BFMTO system. Besides, in BFTO j_{SC} shows a maximum when light polarization is oriented parallel to the ferroelectric domain structure. ($\beta_{333} > \beta_{311}$), opposite to what is observed in the BFMTO system.

The normalized photoconductivity, saturated photoinduced electric fields, and BPV tensors for the different doping conditions are summarized in Table 5.2.

	σ_{ph} ($\Omega^{-1}W^{-1}cm$)	E_{Ph} ($kVcm^{-1}$)	β_{333} (V^{-1})	β_{311} (V^{-1})
$BiFeO_3$	4.8×10^{-7}	-	-	-
$BiFe_{0.98}Ti_{0.02}O_3$	1.2×10^{-7}	1.6	1.68×10^{-5}	1.06×10^{-5}
$BiFe_{0.95}Mn_{0.05}O_3$	5.1×10^{-8}	4.1	0.44×10^{-5}	0.46×10^{-5}
$BiFe_{0.93}Mn_{0.05}Ti_{0.02}O_3$	3.3×10^{-8}	6.9	0.53×10^{-5}	0.55×10^{-5}

Table 5.2: Calculated σ_{ph}, E_{Ph}, β_{333} and β_{311} for the BFO, BFTO, BFMO, and BFMTO IDE capacitors.

5.4 Piezo-photovoltaic effect in polycrystalline $BiFeO_3$

To study the influence of stress in the BPV response, films with different thermal stress values (σ_{th}) were fabricated. Thermal stress arises from different coefficients of thermal expansion for substrate (α_s) and film (α_f). When the $BiFeO_3$ films crystallize during the annealing step at 600 °C, the film is clamped to the substrate. During cooling, the atoms are less mobile, and both substrate and film contract at a different relative value. The resulting film stress σ_{th} can be expressed as:[216]

$$\sigma_{th} = \frac{Y_f}{1-\nu_f}\epsilon_{th} = \frac{Y_f}{1-\nu_f}(\alpha_s - \alpha_f)(T - T_i) \tag{5.1}$$

where Y_f and ν_f are the Young's modulus and Poisson ratio of the film. ϵ_{th} is the thermal strain. T and T_i denote the temperature and the crystallization temperature.

BFMTO films were deposited on three substrates with different TEC: fused silica, c-cut sapphire, and (100) MgO. The samples were named BFO/FS, BFO/Sap, and BFO/MgO, respectively. Assuming a linear TEC of 11.3×10^{-6} K^{-1} for $BiFeO_3$,[217] both the TEC of fused silica at 0.5×10^{-6} K^{-1} and of c-cut sapphire at 7×10^{-6} K^{-1} are lower than the TEC of $BiFeO_3$ and should induce tensile residual stress in the film. On the other hand, MgO with a larger TEC of 13×10^{-6} K^{-1} should create compressive stress in the films.

Figure 5.6 (a) shows the XRD patterns of BFO/FS, BFO/Sap, and BFO/MgO. No secondary phases are observed in any film. All the films show an out-of-plane $[100]_{pc}$ texture induced by the $PbTiO_3$ seed layer. The calculated Lotgering factors are 0.65, 0.85, and 0.75 for BFO/FS, BFO/Sap, and BFO/MgO, respectively.

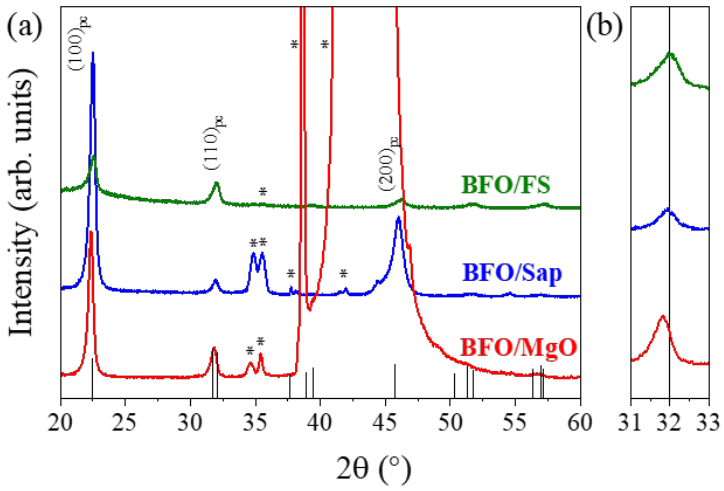

Figure 5.6: (a) XRD pattern of the $BiFeO_3$ films under different stress values. (b) Detail of the (110) peak shift under stress. The peaks marked with * refer to substrate peaks and the non-ferroelectric HfO_2 that acts as a barrier layer between $BiFeO_3$ and the substrate.

A detail of the influence of the substrate-induced thermal stress can be observed in Figure 5.6 (b). The compressive biaxial stress of the films deposited on MgO induces an increase of the out-of-plane lattice parameter, which results in a shift of the $(110)_{pc}$ towards lower 2θ.

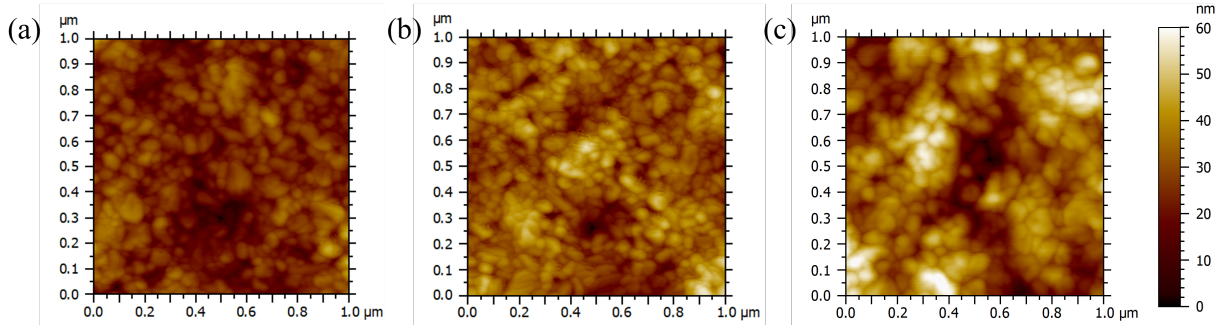

Figure 5.7: AFM topography images of $BiFeO_3$ films deposited on (a) fused silica (b) sapphire (c) magnesium oxide.

AFM topography images are illustrated in Figure 5.7. The films show polycrystalline morphology with a grain diameter of (46 ± 15) nm, (46 ± 16) nm and (55 ± 16) nm for BFO/FS, BFO/Sap and BFO/MgO, respectively. Similar roughness was observed in all the films: (6 ± 1) nm for BFO/FS, (8 ± 2) nm for BFO/Sap and (9 ± 3) nm for BFO/MgO.

$Sin^2\Psi$ measurements were performed to quantify the residual thermal strain in the films deposited on different substrates. The measurements were performed as described in Section 3.1.3. Figure 5.8 (a) - (c) shows the XRD patterns of the $(110)_{pc}$ peak recorded under different tilt angles, a shift towards lower 2θ

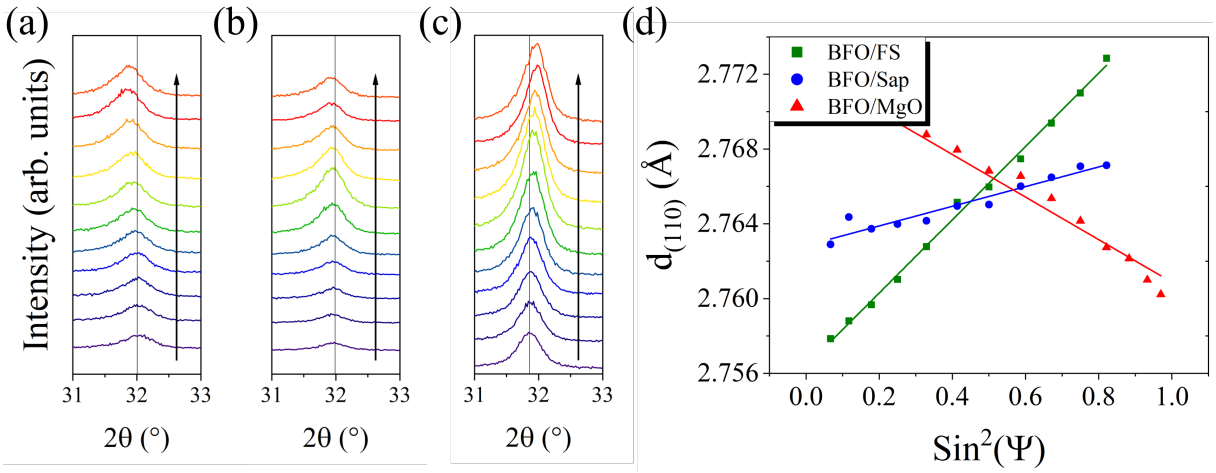

Figure 5.8: (a) XRD pattern of the $(110)_{pc}$ peak at different tilt angles for BFO/FS (b) BFO/Sap (c) BFO/MgO. The increase of the tilt angle (Ψ) from 15° to 65° is indicated by the arrow. (d) $d_{(110)}$ vs $\sin^2\Psi$.

indicates higher $d_{(110)}$ of the planes that are parallel to the normal of the film, indicating residual tensile stress in the film. The opposite indicates compressive stress. The linear relation between $d_{(110)}$ and $\sin^2\Psi$ is shown in Figure 5.8 (d): the positive slope in BFO/FS and BFO/Sap indicates tensile stress and the negative slope in BFO/MgO indicates compressive stress. The in-plane residual strain of the BFO films is 0.38%, 0.1%, and -0.22% for BFO/FS, BFO/Sap, and BFO/MgO, respectively, using a Poisson ratio value of $\nu = 0.3$.[218] The in-plane tensile stress was calculated based on Young's modulus of 170 GPa for $BiFeO_3$.[219] The in-plane tensile stress is 0.93 GPa, 0.25 GPa, and −0.54 GPa for BFO/FS, BFO/Sap, and BFO/MgO, respectively. The measured values of strain in the film agree with the expectations based on the thermal expansion coefficients.

Figure 5.9 (a) show the P(E) loops of $BiFeO_3$ films under different strain values. The films show a remanent polarization (P_r) of $(60 \pm 2)\,\mu C\,cm^{-2}$ for BFO/FS, $(56 \pm 2)\,\mu C\,cm^{-2}$ for BFO/Sap and $(53 \pm 2)\,\mu C\,cm^{-2}$ for BFO/MgO and an average coercive field E_c of $(250 \pm 50)\,kV\,cm^{-1}$. A slight reduction of P_r is observed when stress changes from tensile to compressive. The domain structure of a strongly $(100)_{pc}$-oriented film with a rhombohedral symmetry should show little domain preference with stress, as all eight possible domain variants are energetically equivalent under the present strain values.[220] The higher remanent polarization under higher tensile stress can be explained through local changes in the reduced rhombohedral unit cell. Under higher tensile stress the unit cell is distorted towards a higher a/c lattice parameter ratio. Extrapolating the linear relation in Figure 5.8 (d), the a/c lattice parameter ratio is 1.007, 1.002, and 0.996 for BFO/FS, BFO/Sap, and BFO/MgO, respectively. The in-plane projection of the polarization vector is increased with tensile stress, increasing the measured remanent polarization.

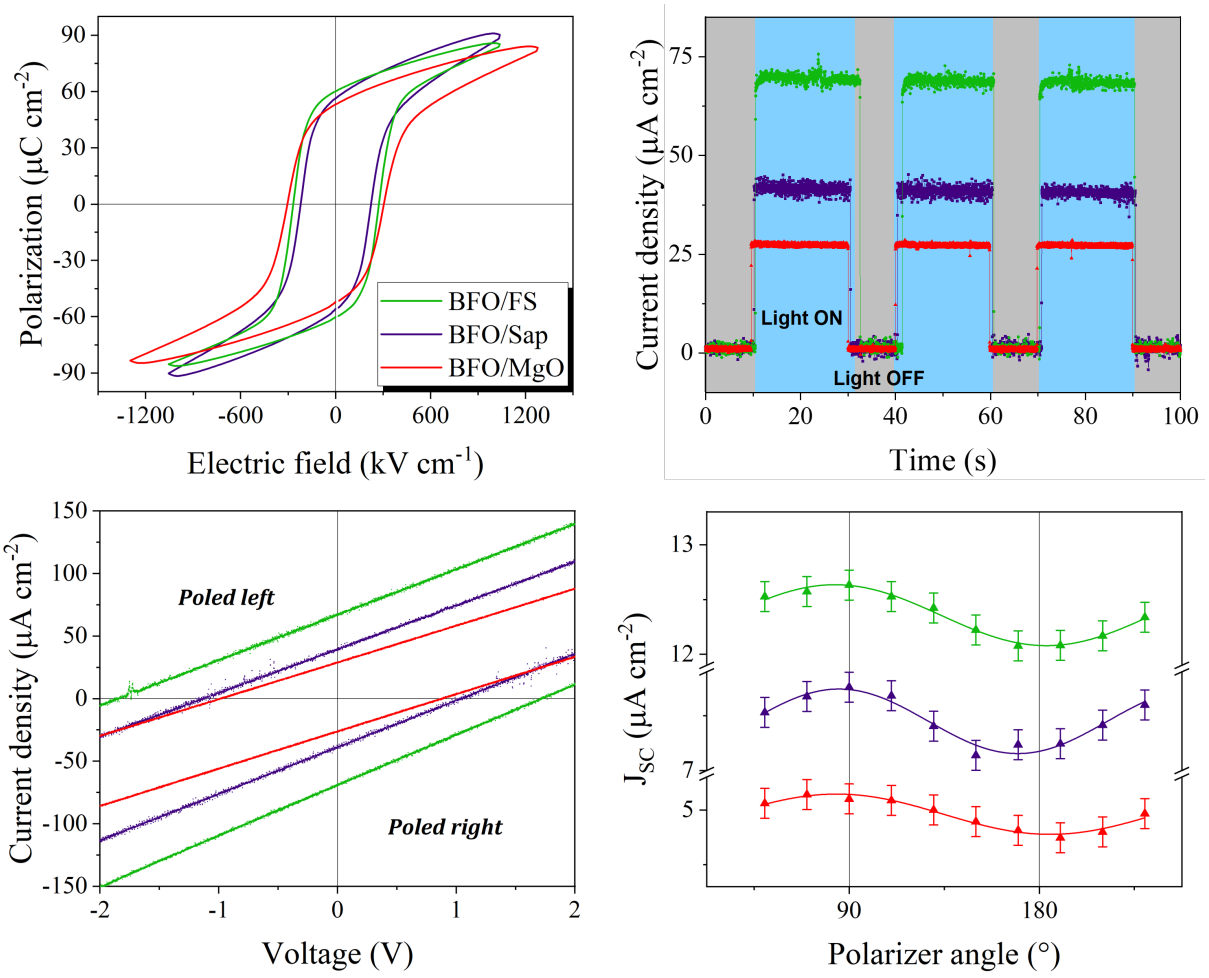

Figure 5.9: (a) P(E) loops of $BiFeO_3$ IDE capacitors deposited on different substrates that induce different stress conditions to the film. (b) ON/OFF j_{SC} values and (c) j-V curves of $BiFeO_3$ thin films deposited on different substrates. The structures were illuminated with a 455 nm nm LED with an intensity of 0.48 W cm^{-2}. (d) Influence of stress and light polarization on the j_{SC}. In the three cases, j_{SC} has a maximum for an angle of 90°/270° with respect to the ferroelectric polarization, representing the BPV tensor component β_{311}, and a minimum for an angle of 0°/180°, representing the BPV tensor component β_{333}.

Figure 5.9 (b) shows the j_{SC} as a function of time for $BiFeO_3$ films under different residual stress values for one poling direction. The j_{SC} values are (70 ± 2) μA cm^{-2} for BFO/FS, (42 ± 2) μA cm^{-2} for BFO/Sap and (27 ± 1) μA cm^{-2} for BFO/MgO. j_{SC} increases by 150% from compressive to tensile stress. Figure 5.9 (c) shows the j-V curves of the devices under illumination for the two different poling conditions. Similar normalized photoconductivity values are measured in all the films. The symmetric switchable effect, expected from a BPV character, also indicates that the photocurrent is not influenced by extrinsic effects that do not depend on the direction of ferroelectric polarization, such as potential flexo-photovoltaic effect, arising from possible strain gradients through the film thickness.

The dependence of the j_{SC} on the light electric field direction for all the samples are shown in Figure 5.9 (d). A sinusoidal variation of j_{SC} with the angle between light polarization and ferroelectric polarization direction is observed in all the samples. This is expected for BPV behavior. The relative variation, i.e., the difference between the photovoltaic coefficients β_{311} and β_{333} is about 8% in BFO/FS and BFO/Sap, but only 4% in BFO/MgO. The normalized photoconductivity, saturated photoinduced electric fields, and BPV tensors for the different doping conditions are summarized in Table 5.3.

	ϵ_{th}	σ_{Ph} ($\Omega^{-1}\,\mathrm{W}^{-1}\,\mathrm{cm}$)	$\mathrm{E_{Ph}}$ ($\mathrm{kV\,cm^{-1}}$)	β_{333} (V^{-1})	β_{311} (V^{-1})
BFO/FS	0.38%	3.3×10^{-8}	6.9	0.53×10^{-5}	0.55×10^{-5}
BFO/Sap	0.1%	3.2×10^{-8}	4.2	0.32×10^{-5}	0.33×10^{-5}
BFO/MgO	-0.22%	2.8×10^{-8}	3.5	0.21×10^{-5}	0.22×10^{-5}

Table 5.3: Calculated σ_{ph}, $\mathrm{E_{Ph}}$, β_{333} and β_{311} for the BFMTO films under different strain values.

The increase in the photocurrent can be explained by taking into account extrinsic effects, e.g., changes in the microstructure or domain structure, or intrinsic effects, i.e., modifications in the local crystallographic structure. All the films show similar microstructure, with similar texture and grain sizes that cannot account for the changes in the photocurrent. The main difference between the films lies in the different residual stress conditions. It may be argued that the interplay between the piezoelectric effect and stress may generate internal electric fields that may influence the light-induced charge transport. However, with a dark resistivity of $5 \times 10^6\,\Omega\,\mathrm{m}$, and a permittivity of $\epsilon = 200$, any such field will be screened by mobile charges with an exponential decay time of $\tau = \rho * \epsilon * \epsilon_0 = 10^{-2} s$, i.e., shorter than the time resolution of the measurement.

Another extrinsic effect to consider is a stress-induced modification of the domain structure. Figure 5.10 shows the out-of-plane DART piezo-response force microscopy (PFM) images of unpoled $BiFeO_3$ under different stress values.

To evaluate changes in domain structure, the domain wall-to-grain boundary ratio was evaluated using the line profile analysis of the topography images (accounting for grain boundaries) and the amplitude images (accounting for grain boundaries and domain walls). In the amplitude images, grain boundaries and domain walls are defined by a minimum in the amplitude, while in the topography image, the grain boundary is defined as a minimum in the topography signal. The ratio of domain wall length on grain boundary length is 1.4, 1.6, and 1.5 for BFO/FS, BFO/Sap, and BFO/MgO, respectively. Values higher than one indicate that some grains show domain walls. The films show similar domain wall densities, indicating that stress does not strongly modify the domain structure.

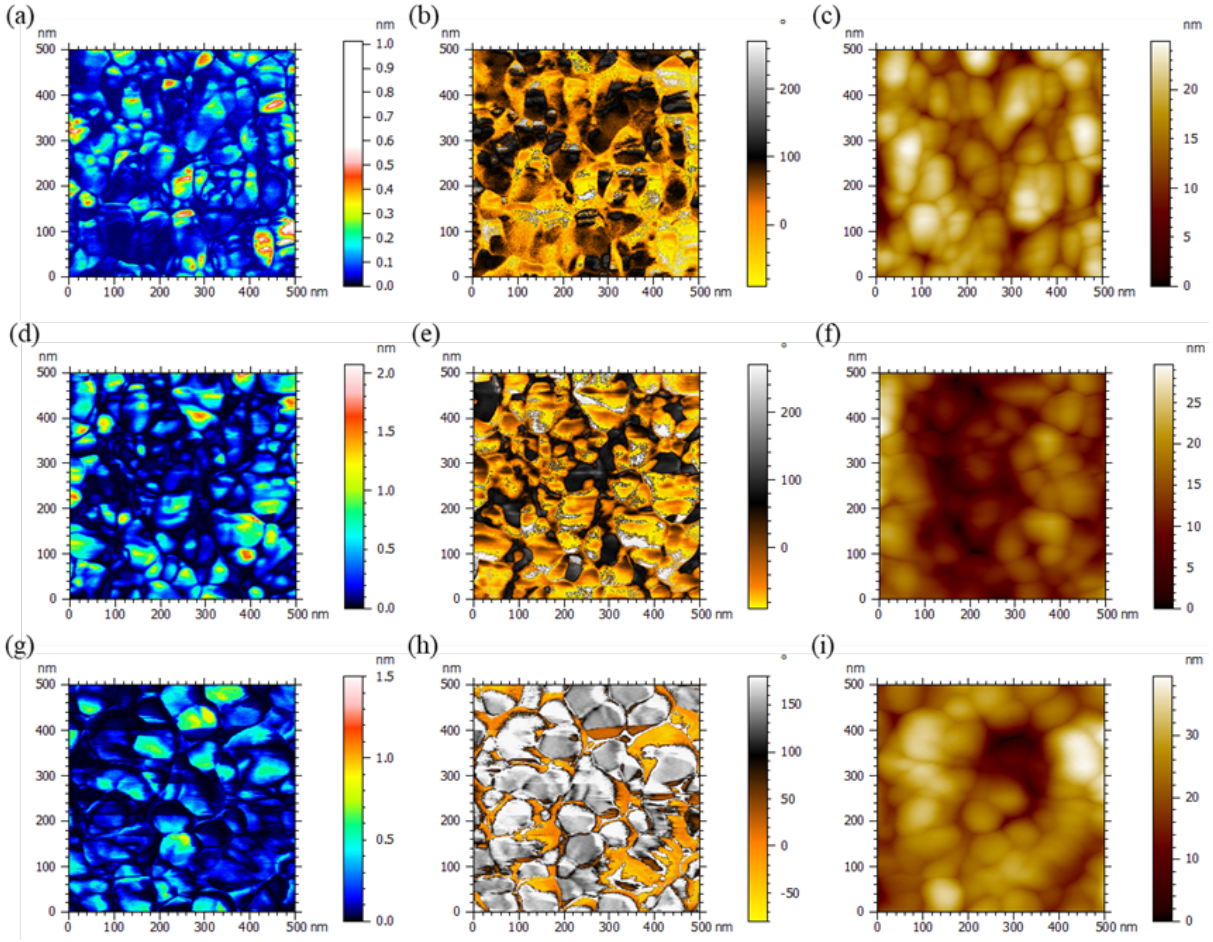

Figure 5.10: Out-of-plane DART PFM amplitude (left column), phase (middle column) and topography (right column) images of the unpoled $BiFeO_3$ films on (a)-(c) fused silica, (d)-(f) sapphire, (g)-(i) magnesium oxide.

Modifications in the domain structure of $BiFeO_3$ should have a strong influence on the photoconductivity of the films, due to the large difference between the bulk and domain wall conductivity.[124, 221] In the present case, the photoconductivity does not show a strong dependence on the strain, with modifications of only 15% that do not account for a strong modification of the domain structure. Besides, contrary to the current observations, strongly different domain structures should have a clear influence on the P(E) loops. This agrees with the expectation that the P(E) loops of a ferroelectric with rhombohedral symmetry should show little domain preference with stress when the electric field is applied along the $(100)_{pc}$, as all eight possible domain variants are energetically equivalent.

Since the possible extrinsic contributions to the BPV effect have been ruled out, the increased j_{SC} under tensile stress is likely a result of an intrinsic piezo-photovoltaic effect. The local crystallographic structure is distorted by stress. Under high tensile stress, the noncentrosymmetric character of $BiFeO_3$ is

enhanced. The exact microscopic origin of the piezo-photovoltaic effect in $BiFeO_3$ would require more in-depth studies, e.g., the time-dependence of the current under pulsed illumination or of the electronic states by Electron Paramagnetic Resonance, that are beyond the scope of this Ph.D. thesis. However, based on literature results, two mechanisms appear as plausible explanations of the enhancement: the modification of non-thermalized hopping of photo-excited charge carriers or the strain modification of the shift current.

The first proposed mechanism is in line with the results on the piezo-photovoltaic effect in Fe:$LiNbO_3$.[25] In Fe:$LiNbO_3$ a change in the interatomic distances under stress lead to changes in the photo-excitation and propagation of non-thermalized charge carriers, modifying the BPV response. In contrast to Fe:$LiNbO_3$, where an increase of the j_{SC} was observed under uniaxial compressive stress, j_{SC} increases under biaxial tensile stress in Mn^{x+} and Ti^{4+} co-doped $BiFeO_3$. In Fe:$LiNbO_3$ the origin of the BPV effect relies on the non-thermalized hopping of electrons between polaronic Nb^{4+} sites after excitation from A-site Fe^{2+} defects.[222] In that direction, the reduction of the hopping distances enhances the BPV effect. In Mn^{x+} and Ti^{4+} co-doped $BiFeO_3$ a similar mechanism may occur. The BPV effect may be dominated by the hopping between the Mn^{2+} and Mn^{3+} states to the Fe^{3+} ions.[129] The excitation probability from the Mn^{2+} and Mn^{3+} states to the Fe^{3+} surrounding ions will depend on the interatomic distances. In that case, the enhancement in the photocurrent can be reasonably ascribed to the increase in the non-thermalized hopping.

The second possible mechanism is associated with the shift current mechanism. Rappe et al. proposed that the main component of the BPV effect in $BiFeO_3$ and other ferroelectric perovskites is the shift current.[60, 61] Theoretical calculations have demonstrated that strain can modify the magnitude of the shift current in transition-metal dichalcogenide MoS_2.[70] However, no theoretical calculations on the influence of strain on the shift current component of the BPV effect can be found for $BiFeO_3$.

5.5 Outlook

In summary, this chapter proves that the BPV effect is the main mechanism for light-induced charge carrier separation in polycrystalline $BiFeO_3$. Additionally, it illustrates the strategy to be followed to identify the dominating light-induced charge transport: the study of the dependence of the j-V curves with the poling state, light intensity, light polarization, and distance between electrodes is key to identifying a BPV effect.

Doping plays a key role in the BPV effect, not only increasing absorption,[129] but also controlling key parameters such as photoconductivity. Crystals with low conductivity typically result in a large photoinduced electric field at the expense of a slower response under illumination. Doping with donor dopants such as Ti^{4+} to control the oxygen vacancy concentration allows for the reduction of the photoconductivity. On the other hand, Mn^{x+} doping traps the charges excited from the V_O, reducing the photoconductivity.

The existence of a piezo-photovoltaic effect in $BiFeO_3$ is demonstrated: the photocurrent is enhanced by 150% from the films under compressive stress to the films under tensile stress. In polycrystalline films on rigid substrates, strains larger than 0.5% cannot be achieved due to the cracking of the material under large strain values. An interesting strategy to tune the BPV effect is the direct epitaxial growth on a single crystalline substrate, where strains in the order of 3% can be achieved.[223, 224] One step further would be fabrication of free-standing films.[225, 226] The transfer of epitaxial thin films to polymeric substrates produces flexible membranes withstanding unprecedented large strains (up to 10% in $BaTiO_3$).[227] These large strain values have a great potential to engineer the BPV effect in $BiFeO_3$.

Applications of the BPV, such as photostriction or photorefraction, require the formation of large photoinduced electric fields. The performance of materials exhibiting the BPV effect is usually reported through the BPV tensor. However, a better figure of merit should include the values of photoconductivity, the key to obtaining large photoinduced electric fields. Unfortunately, most literature reports on the BPV effect of $BiFeO_3$ focus on anomalously large photovoltages without discussing the distance with the electrodes, which is key to comparing the photoinduced electric fields.

In conclusion, low-cost polycrystalline materials have a strong potential for the development of photoinduced functionalities. The reduction in the BPV tensor to 35% the values reported in $BiFeO_3$ epitaxial films[196] is compensated by the lower cost of solution-processed films.

Chapter 6

Electro-optic effect of polycrystalline $BiFeO_3$ films

6.1 Motivation

With their linear electro-optic (EO) effect, i.e., a linear change of refractive index as a function on an applied electric field, ferroelectric thin films are crucial for the fabrication of optical modulators in integrated photonic circuits.[94, 95]

$BiFeO_3$ has recently been studied as a multiferroic optical material,[134] in which the optical properties can be tuned by the application of an electric field, i.e., EO effect, the application of a magnetic field, i.e., magneto-optic effect, or light, i.e., photorefraction, opening new exciting possibilities to control its optical properties. $BiFeO_3$ is also a very interesting material for high-temperature applications: not only its T_C is much higher than for $BaTiO_3$ or $PbZr_xTi_{1-x}O_3$, but in addition, mode softening is much weaker in general due to the more complex nature of the ferroelectric transition in $BiFeO_3$, which result in the lower temperature dependence of the functional properties.[131, 132]

Additionally, the massive birefringence of $BiFeO_3$ of 0.15-0.31,[133, 174] allows for refractive index tuning by reorientation of the optical axis through ferroelectric domain switching, i.e., extrinsic EO effect. However, values of EO coefficients of $BiFeO_3$ can only be found for epitaxial thin films, reporting effective EO coefficients (r_{eff}) around (15 ± 5) pm V^{-1}.[134, 135] There are yet no reports on the EO coefficients of low-cost polycrystalline $BiFeO_3$, more adequate for applications, due to their compatibility with silicon technologies and roll-to-roll solution-processing.

In this chapter, the EO properties of polycrystalline $BiFeO_3$ thin films with IDEs are measured using an in-house built Teng-Man (TM) set-up in transmission geometry. $BiFeO_3$ films under different substrate-induced residual thermal stress are measured. To explore the extrinsic contributions to the EO effect, transparent embedded IDEs are used.

6.2 Pockels effect in $BiFeO_3$ films and strain dependence

To measure the EO properties of ferroelectric films, a TM set-up in transmission geometry was built. A detailed description of the measurement set-up can be found in Section 3.3.2, with the details that are needed for the measurement of the EO coefficient r_{eff} ($r_{\text{eff}} = r_{33} - r_{31}(n_o^3/n_e^3)$).

To study the Pockels effect, Mn^{x+} and Ti^{4+} co-doped $BiFeO_3$ films with a thickness of 340 nm were fabricated on three different substrates: fused silica, c-cut sapphire (both Siegert Wafer, Germany), and MgO (Biotain Crystal, PR China). The deposition of the films in different substrates results in different thermally-induced stress conditions. The deposition procedure is described in Section 3.1.1. The discussion on the residual thermal induced substrate stress is shown in Section 5.4.

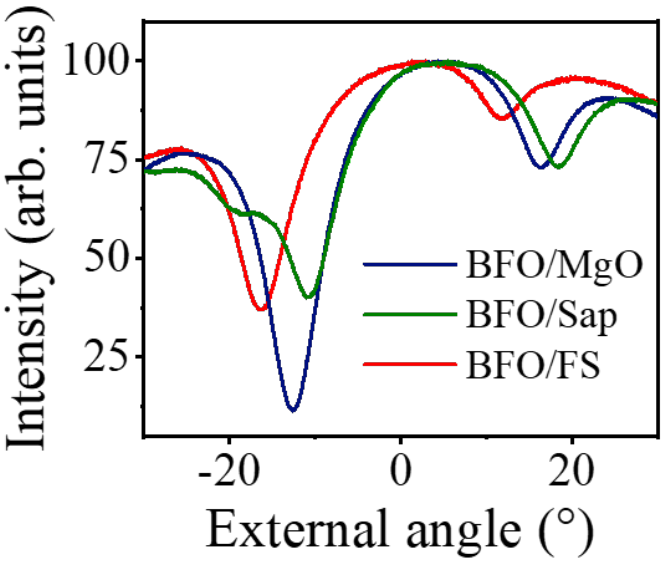

Figure 6.1: Prism coupling measured intensity vs external angle showing two waveguide modes in $BiFeO_3$ films deposited on different substrates. The two modes allow for the determination of the thickness and refractive index of the films.

The determination of r_{eff} requires a precise measurement of the thickness and the refractive index. Therefore, the refractive index and the thickness of the films were measured using the prism coupling technique. The operation principle is explained in Section 3.3.1. Figure 6.1 show the two waveguide modes, identified as a drop in the reflected light intensity as a function of the light incidence angle. The shift of

the peaks under different stress values indicates a shift in the refractive index of the film. The observation of two modes allows the determination of the thickness and refractive index of the film, solving the mode equation discussed in Section 3.3.1.

	Refractive index	**Thickness**
BFO/FS	(2.74 ± 0.01)	(339 ± 2) nm
BFO/Sap	(2.81 ± 0.01)	(340 ± 2) nm
BFO/MgO	(2.79 ± 0.01)	(342 ± 2) nm

Table 6.1: Values of thickness and refractive index of the samples deposited on different substrates.

The refractive index and thickness are summarized in Table 6.1. The refractive index values are similar to previous reports.[134, 228] A change of 2% in the refractive index is observed under different stress conditions. In agreement with [174], the refractive index of $BiFeO_3$ decreases both under compressive and tensile stress. In polycrystalline films, the refractive index is isotropic prior to poling i.e., the optical axes of the individual grains are randomly distributed, and the measured refractive index is an average between n_o and n_e. To discern between the two indices, the measurement would have to be performed on a poled sample. However, the prism coupling technique requires a high-quality contact between the prism and the surface of the film, that is not compatible with the coplanar electrodes.

To measure the r_{eff} of the $BiFeO_3$ films, co-planar IDEs were patterned on top of the films. The IDEs consist of 50 pairs of fingers with an effective length of 1.5 mm. The width of the fingers is (10.0 ± 0.5) µm and the space between the fingers is (5.0 ± 0.5) µm. The devices were fabricated as described in Section 3.1.2. Several devices from different sample batches were measured to ensure the repeatability of the obtained values. Prior to the measurement, the devices were poled. The initial poling procedure consisted of the application of a single bipolar triangular field pulse with an amplitude of 1000 kV cm^{-1} and a frequency of 1 kHz, while simultaneously recording a ferroelectric P(E) hysteresis loop of polarization as a function of the electric field. This ensures the proper electrical connection of the device. In a second step, additional poling was performed by applying a train of unipolar sinusoidal electric field pulses with an amplitude of either 800 kV cm^{-1} or 900 kV cm^{-1} and a frequency of 1 kHz during 10 s, for a total of 10,000 poling pulses.

In the Teng-Man set-up, upon alignment of the laser between the co-planar electrodes, the voltage at the photodiode, V_{PD}, was measured as a function of the phase controller phase shift. Then, a unipolar sinusoidal electrical signal with a frequency of 1 kHz of a given amplitude was applied and the demodulation voltage amplitude, V_{LI}, and phase from the lock-in amplifier was recorded as a function of the phase con-

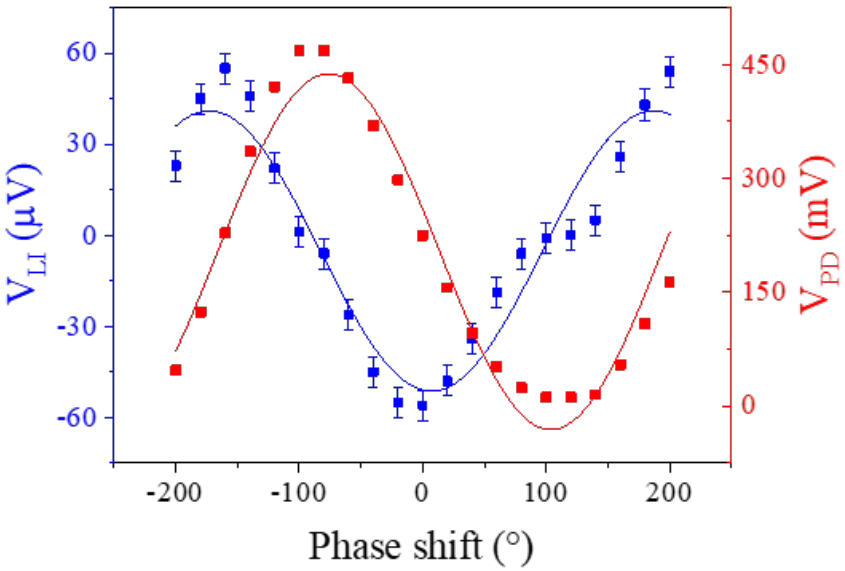

Figure 6.2: V_{LI} and V_{PD} curves for a BFO/Sap sample poled at 900 kV cm^{-1}and a driving field of 100 kV cm^{-1} for the measurement of the Pockels coefficient.

troller phase shift. An example of V_{PD} and V_{LI} as a function of the phase controller phase shift is depicted in Figure 6.2. Under these conditions $V^0{}_{PD}$ has a value of 450 mV. This corresponds to a 2π phase shift of the 45° polarized incoming light. On the other hand, $V^0{}_{LI}$ has a value of 90 μV. Using these values, r_{eff} can be calculated using the equation described in Section 3.3.2:

$$r_{\text{eff}} = r_{33} - r_{13}\frac{n_o^3}{n_e^3} = \frac{\lambda V^0_{\text{LI}}}{\pi n_e^3 L_{\text{BFO}} A V^0_{\text{PD}}}. \tag{6.1}$$

As shown in Equation 6.1, an optimal electric field penetration into the film is key for the measurement of EO coefficients in transmission geometry. Insufficient penetration of the electric field in the film would lead to an underestimation of the r_{eff}. The role of the electric field distribution in the EO coefficients is discussed in Appendix C.

To ensure complete penetration of the electric field in the film, the in-plane component of the electric field distribution was numerically simulated by the Finite Element Method with the COMSOL software package, with a voltage of 50 V applied between the co-planar electrodes. The simulation is illustrated in Figure 6.3. In the current configuration, where the distance between the electrodes is an order of magnitude larger than the thickness of the film, the electric field in the film is homogeneous. The field also extends a few micrometers into the substrate, but as none of the substrates used have linear EO properties, no extra contribution to the measured EO coefficient is expected.

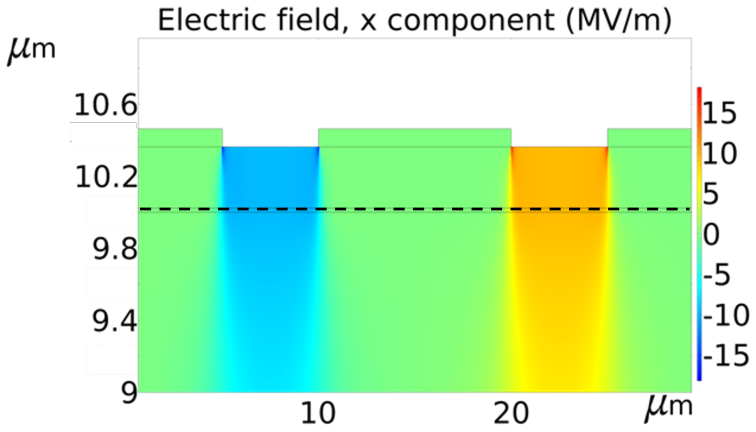

Figure 6.3: Modelling of the electric field penetration into a $BiFeO_3$ thin film.

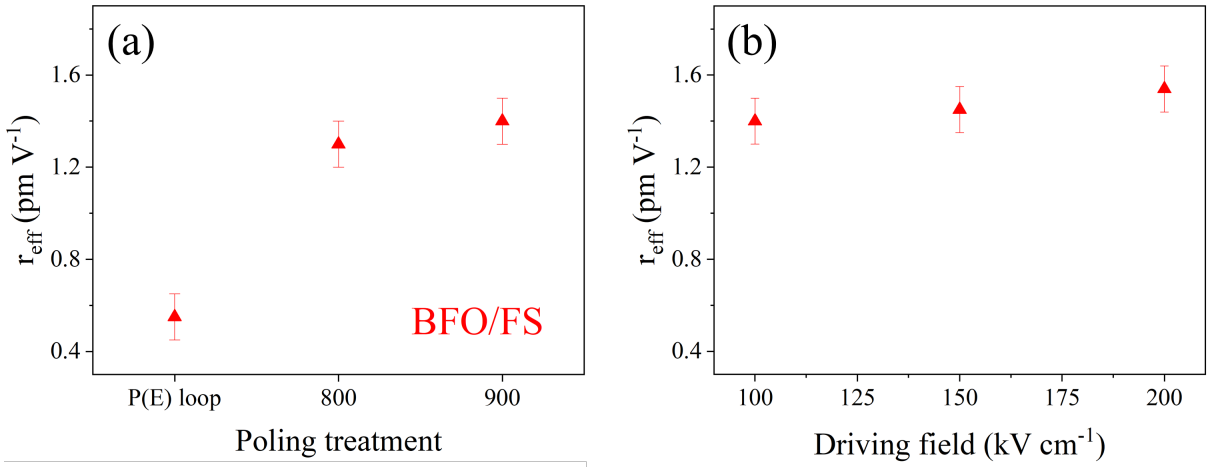

Figure 6.4: (a) Calculated EO coefficients for a $BiFeO_3$ film deposited on fused silica with different poling treatment and a driving field of 100 kV cm^{-1}. (b) Calculated EO coefficients for a $BiFeO_3$ film deposited on fused silica with different, below E_c, driving fields after poling at 900 kV cm^{-1}.

The linear EO properties of polycrystalline $BiFeO_3$ are summarized in Figure 6.4 on the example of BFO/FS. Figure 6.4 (a) shows the r_{eff} values obtained for $BiFeO_3$ films deposited on fused silica with different poling treatments and a driving field of 100 kV cm^{-1}. The unpoled samples do not present a measurable V_{LI} signal, while after poling with a single ferroelectric hysteresis loop with an amplitude of 1000 kV cm^{-1}, values of 0.55 pm V^{-1} are obtained. This value increases to 1.3 pm V^{-1} after poling with 10,000 pulses of 800 kV cm^{-1} as described above; obviously, the single hysteresis loop is insufficient to achieve poling. When poling with 10,000 pulses of 900 kV cm^{-1}, this value increases only slightly to 1.45 pm V^{-1}, indicating that a near-saturation level of poling is reached with this procedure, in agreement with earlier poling

studies.[229] Figure 6.4 (b) shows the EO coefficients as a function of the driving electric field. As expected, at driving voltages below the coercive field ($E_c = 300\,kV\,cm^{-1}$), r_{eff} does not vary with the applied electric.

It has to be noted that these values are only about 10%-15% of the values reported for single crystals.[134] This can be expected due to the polycrystalline nature of the samples: epitaxial thin films typically show better EO properties than polycrystalline ones. The individual grains cannot be fully poled due to the formation of depolarizing fields and internal stress between grains. Additionally, the lack of in-plane texture induces a misalignment between the grains. This is translated into the reduction of the EO response. The same behavior with different poling treatments and at different driving fields is observed in the samples under different stress values.

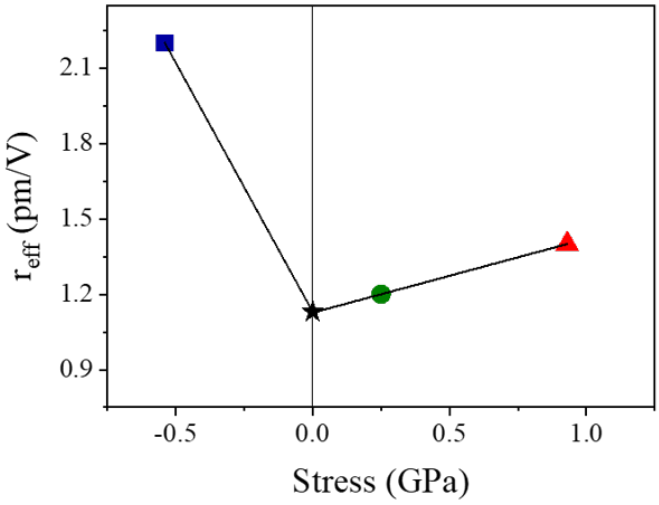

Figure 6.5: Measured EO coefficients for $BiFeO_3$ films on different substrates after poling at $900\,kV\,cm^{-1}$. The stress-free EO coefficient is extrapolated from the two samples under tensile stress assuming a linear stress dependence. Blue: BFO/MgO, Green: BFO/Sap, Red: BFO/FS.

The influence of residual thermal-induced substrate stress is shown in Figure 6.5 after poling with 10,000 pulses of $900\,kV\,cm^{-1}$, which reaches the saturation region. Under low tensile stress, (BFO/Sap) the EO coefficient has a value of $1.2\,pm\,V^{-1}$. Under higher levels of tensile stress (BFO/FS) the EO coefficient is increased up to $1.45\,pm\,V^{-1}$. A stronger enhancement of the EO response is observed in the samples under compressive stress (BFO/MgO), with values up to $2.2\,pm\,V^{-1}$. The experimental results suggest that both compressive and tensile stress increases the EO coefficients in $BiFeO_3$. Assuming that the EO coefficients increase linearly with stress, the zero-stress EO coefficient can be estimated to be 1.1 pm/V. It is understood that a linear extrapolation from two data points is to a high degree speculative, but given

the relatively low variation of r_{eff} between BFO/Sap with a stress of 0.25 GPa and BFO/FS with a stress of 0.93 GPa, the approach seems reasonable. If this approach is followed, r_{eff} increases with a piezo-EO coefficient of 0.3 pm V^{-1} GPa^{-1} 0.3 under tensile stress and 2 pm V^{-1} GPa^{-1} under compressive stress.

It may appear counterintuitive that r_{eff} increases under both tensile and compressive stress. In fact, in materials such as ZnO, first-principles calculations have predicted an increase in r_{eff} under compression and a decrease under tension.[230] However, this prediction may not hold for polyaxial perovskite-structured ferroelectrics, as it was specifically made for a uniaxial system with a wurtzite structure. In polyaxial perovskite-structured ferroelectrics, first-principles studies predict a behavior like the one observed here for $PbTiO_3$[231] (PTO) and $BaTiO_3$[232]. However, to date, none of these predictions have been experimentally confirmed. In the case of PTO, the increase in r_{eff} under tension has been attributed to the softening of the $E^{(2)}$ phonon mode during the tetragonal/monoclinic phase transition, while the increase under compression is linked to electro-mechanical coupling based on the enhanced piezo-response in tetragonal PTO. In the case of BTO, the enhancement is produced due to a strain-induced divergence in the first and second-order susceptibility. The stress levels in the $BiFeO_3$ films examined in polycrystalline $BiFeO_3$ are not sufficient to trigger any phase transition,[233, 234] making the mechanism discussed in [231] unlikely. Besides, under different degrees of stress, the poling state of the different films is very similar (see Section 5.4) in agreement with the expectations for a (001)-oriented rhombohedral perovskite. The most plausible explanation at this point is the enhancement of the EO response due to modifications in the local phonon mode structure that may lead to a mode softening, directly modifying the EO coefficients.[232]

6.3 Extrinsic contributions to the electro-optic effect

When an electric field larger than the coercive field is applied to an unpoled polycrystalline ferroelectric film, the ferroelectric domains inside the individual grains align with the direction of the electric field, creating anisotropic optical properties that depend on the poling direction. However, when the electric field is removed, some of these oriented domains will switch back, due to the strain and the depolarizing field between grains. This will induce a reduction of the degree of anisotropy of the optical properties.

As explained in Section 5.2, the retained polarization is less than 50% of the saturated polarization, which indicates that some of the domains that are oriented when the field is applied switch back when the field is turned off. The process of poling and back-switching in polycrystalline materials is illustrated in Figure 6.6. The changes in the optical properties under an electric field higher than E_c will depend on the birefringence of the material. In $BiFeO_3$, a high extrinsic response is expected due to the high birefringence of 0.3 at 633 nm.[133, 134]

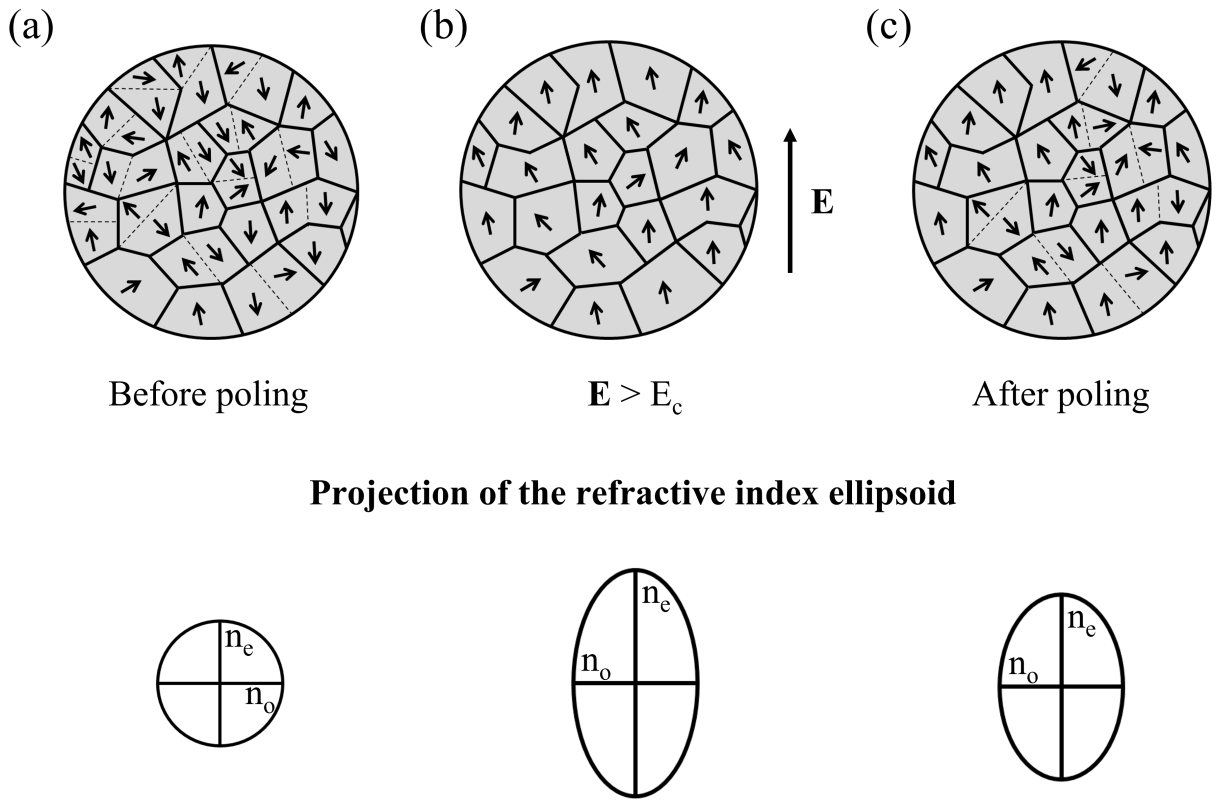

Figure 6.6: (a) Schematic showing randomly oriented domains in a polycrystalline film prior to poling. The film shows isotropic optical properties (b) Oriented domains upon the application of an electric field higher than the coercive field. The optical properties of the film are highly anisotropic (c) Poled film without an electric field. Some domains switch back, reducing the degree of anisotropy of the optical properties. The grain boundaries are illustrated by a solid line. The domain walls are represented by a discontinuous line. The arrows indicate the direction of the ferroelectric polarization. n_e and n_o refer to the extraordinary and ordinary refractive index.

However, the standard IDEs structures used to measure the linear EO properties do not survive repetitive switching. Instead, the transparent embedded IDEs, discussed in Section 4.4 were used due to their fatigue-free behavior up to 10^6 cycles and stable ferroelectric switching. The samples were prepared as explained in Section 3.1.1.

Figure 6.7 shows the values of r_{eff} as a function of the driving electric field with fields between 100 kV cm^{-1} and 900 kV cm^{-1}, below and above E_c values. As shown previously, below E_c the EO coefficient shows little dependence on the electric field, i.e., the induced phase shift increases linearly with the applied electric field. On the other hand, under switching conditions ($E > E_c$), r_{eff} increases drastically to 2.5 pm V^{-1} under electric field values just above the coercive field. This value saturates to 5.2 pm V^{-1} at electric field values at which the polarization saturates.

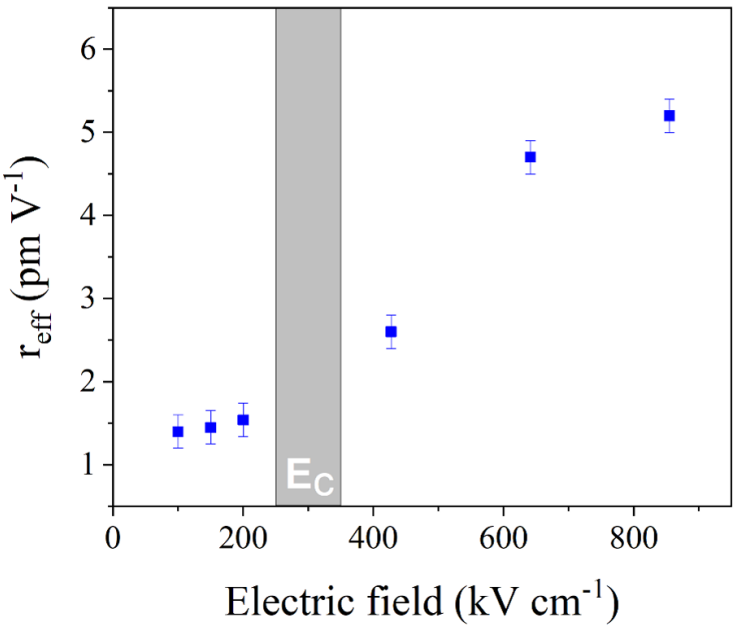

Figure 6.7: Values of r_{eff} measured in $BiFeO_3$ films with embedded F:SnO_2 IDEs at below E_c and above E_c driving fields. The values highlight the intrinsic (Pockels effect) and extrinsic (Switching) contributions to the EO effect.

The use of extrinsic contributions to the EO effect is limited by the maximum domain back-switching that is produced when the electric field is turned off. In polycrystalline materials, the maximum degree of anisotropy of a perfectly poled ceramic is limited by the misorientation of the grain. Indeed, with the current estimation of birefringence in $BiFeO_3$, of 0.31, one could obtain an effective EO coefficient of 1500 pm V^{-1} by electrically switching the optical axis of a $BiFeO_3$ single crystal by 90°.

6.4 Outlook

The Pockels effect in polycrystalline $BiFeO_3$ films was measured using a Teng-Man set-up in transmission geometry. The results show a strong increase of r_{eff} with both tensile and compressive stress. The large piezo-EO coefficient under compressive stress has a stronger potential in epitaxially strained $BiFeO_3$, where a higher degree of strain can be achieved, e.g., on $DyScO_3$ (-0.8%), $SrTiO_3$ (-1.7%), or LSAT (-2.4%).[223]. Besides, the current theoretical correlation between the divergence of the dielectric susceptibility close to a phase transition with giant EO responses[231, 232] suggests that an enhancement of the EO properties appears close to structural phase transitions. Among the strategies to drive $BiFeO_3$ close

to a structural phase transition, epitaxial strain,[174] La-doping,[235] or negative pressure through He-implantation[236] have a strong potential to enhance the Pockels effect in $BiFeO_3$ when driving $BiFeO_3$ close to a structural phase transition.

The drastic enhancement of r_{eff} at above E_c fields constitutes the first evidence of using the extrinsic contributions to the EO effect in a ferroelectric with high birefringence. In classical single-domain ferroelectrics, stretching or compression of the optical indicatrix occurs under a field. However, in analogy with liquid crystals, a more significant change of the optical properties occurs from the additional extrinsic contributions resulting from the rotation of the individual optical indicatrix of grains, polar regions, or domains. The high potential of extrinsic contributions to the EO effect can be evidenced in the giant EO effect of relaxor ferroelectrics.[90] At zero field, the polar nanoregions are randomly oriented, leading to a nearly isotropic optical indicatrix. Under an electric field, the polar nanoregions align with the electric field, resulting in a strong change in the optical indicatrix.

The results obtained in this chapter encourage the design of materials in which the transient rotation of the individual optical indicatrix is used to achieve giant EO coefficients in a highly birefringent material e.g., $BiFeO_3$. The combination of classical intrinsic and extrinsic effects is key for the fabrication of high-performance EO modulators for integrated silicon photonics.

Chapter 7

Conclusion and perspectives

This thesis provides new routes towards the fabrication of low-cost solution-processed $BiFeO_3$ films with excellent ferroelectric properties. The use of a $PbTiO_3$ or a $LaNiO_3$ seed layer is an effective strategy to fabricate $(100)_{pc}$-oriented $BiFeO_3$ films using solution-deposition methods. Doping is key to controlling the film's charge transport properties. A donor dopant, such as Ti^{4+}, reduces the oxygen vacancy concentration. On the other hand, doping with Mn^{x+} modifies the conduction mechanism, increasing the conductivity at low fields but reducing the conductivity at switching fields. In addition, oxide-based embedded IDEs lead to superior ferroelectric fatigue properties compared to the standard IDEs.

Some applications require single-crystal films. For example, the misalignment between grains in polycrystalline films reduces the Pockels coefficients compared to single-crystal $BiFeO_3$ films. Additionally, the relatively high roughness of polycrystalline films would lead to significant optical losses. The results obtained in the epitaxial growth of $BiFeO_3$ and $PbZrO_3$ encourage the fabrication of epitaxial films on silicon. This would bridge the gap between low-cost solution-processed and vacuum-processed films. Among the different strategies that could be followed, incorporating buffer layers such as TiN[210, 211] to overcome the large lattice parameter misfit between silicon and oxide perovskites is an exciting approach to pursue since it is compatible with low-cost silicon-based processes.

The BPV effect is proven to be the driving mechanism of light-induced charge-carrier separation. Photoinduced electric fields up to $10\,kV\,cm^{-1}$ are obtained in Mn^{x+} and Ti^{4+} co-doped films under tensile stress. Strain and doping are key parameters to engineer the BPV effect. The strain-engineering of the BPV effect has an even stronger potential in epitaxial free-standing films that can withstand unprecedentedly large strains.[226, 227]

Applications of the BPV effect, such as light-induced ferroelectric switching, photostriction, or photorefraction, rely on maximizing the photoinduced electric fields. Lower photoconductivity leads to a higher photoinduced electric field at the expense of slower decay times when the light is turned off. High conductivity leads to low photoinduced electric fields but allows a fast decay of the photoinduced electric field, being more useful for transient applications. Tuning the conductivity by modifying the deposition parameters or by doping is key to tuning the current-voltage characteristics.

Regarding the EO properties, strain is an effective way to tune the Pockels effect in $BiFeO_3$ films. Higher piezo-electro-optic coefficients are obtained under compressive stress. Additionally, this thesis proves the potential of using extrinsic contributions based on transient ferroelectric domain switching to obtain larger EO coefficients.

These results provide new pathways to enhance the EO coefficients of $BiFeO_3$ films. First, the use of epitaxial films where larger compressive strain values can be achieved. Second, exploring these extrinsic contributions as a new EO mechanism. Ferroelectric switching leads to a rotation of the refractive index ellipsoid, modifying the optical properties. These contributions would be maximized in highly birefringent ferroelectric materials, where the extraordinary refractive index, along the direction of ferroelectric polarization, is much larger than the ordinary refractive index. For example, considering that $BiFeO_3$ has a refractive index of 2.7 and a switching field of 200 kV cm^{-1} values equivalent to r_{eff} of 1500 pm V^{-1}, are estimated. This would arise only from the rotation of the refractive index ellipsoid during ferroelectric switching and would add up to the linear electro-optic response. This opens the path to fabricate artificial high birefringent ferroelectrics where a 90° transient ferroelectric switching induces a rotation of the optical indicatrix, resulting in a giant EO response.

The BPV effect characterization, together with the measurements of EO coefficients of polycrystalline $BiFeO_3$ can be combined to assess the potential of solution-processed $BiFeO_3$ for transient photorefractive applications such as reconfigurable waveguides.[237, 238] The change in refractive index under illumination can be estimated using the following equation:[238]

$$\Delta n = -\frac{1}{2} r_{\text{eff}} n^3 E_{ph} \tag{7.1}$$

where E_{ph} is the photoinduced electric field. For the films studied in this manuscript, upon illumination with 455 nm light at an intensity of 0.48 W cm^{-2}, photoinduced electric fields (E_{ph}) of 10 kV cm^{-1} were observed on a short time scale. With an EO coefficient of 2 pm V^{-1}, a change of refractive index (Δn) of 2×10^{-6} can be achieved due to the photoinduced electric field. For comparison, typical values of photoinduced Δn in $LiNbO_3$ single crystals have an order of magnitude of 10^{-5}.[239] Additionally, the

high dark conductivity of $BiFeO_3$ ($\sigma_{Dark} = 2 \times 10^{-7}\,\Omega^{-1}\,m^{-1}$) enables the built-up field to decay rapidly after the illumination stops. Although this may not be ideal for long-time applications such as optical data storage, it is highly beneficial for applications relying on transient changes of the refractive index such as optically reconfigurable waveguides.

Appendix A

Epitaxial chemical solution-deposited $PbZrO_3$ films

A.1 Motivation

Antiferroelectrics (AFE) are recognized by three main characteristics: an antiparallel atomic displacements of electric dipoles, a phase transition between two nonpolar phases, and the possibility to induce a phase transition to a polar phase by an electric field.[240–242] The prototypical AFE perovskite material is lead zirconate, $PbZrO_3$, first identified as an antiferroelectric by Shirane in 1951.[241] Around 510 K, it undergoes a phase transition from an orthorhombic antiferroelectric phase to a cubic paraelectric phase.[241] In the antiferroelectric phase, the Pb^{2+} ions shift along the $[100]_o$ direction of the orthorhombic unit cell.[243] The unique property of antiferroelectric materials is their transition from a linear dielectric response to a ferroelectric response, leading to exciting applications in high energy storage,[244, 245] electrocaloric cooling,[246] and electro-optics.[247, 248]

Practical applications of functional films require the development of high-quality films through scalable and cost-effective fabrication processes. Pulsed laser deposition[249–251] and metal organic chemical vapor deposition[252] have successfully produced high-quality epitaxial $PbZrO_3$ films. However, these methods rely on expensive vacuum technologies and lack scalability. In contrast, chemical solution deposition is a low-cost and scalable alternative for manufacturing functional thin films.[102] While numerous reports exist on high-quality polycrystalline films prepared through solution deposition methods,[253, 254] some applications require the fabrication of single crystal films. Nevertheless, obtaining high-quality

single-crystal films by chemical solution deposition is challenging due to the formation of grains, secondary phases, or defects during the process. Presently, there are no reports on the successful fabrication of $PbZrO_3$ single crystal thin films through solution deposition.

The presence of a ferroelectric (FE) contribution during antiferroelectric switching in $PbZrO_3$ has been a subject of debate among the AFE community. Recently, Aramberri et al.[255] have shown that the ground state of pure $PbZrO_3$ may not be AFE but ferrielectric.(FI) Indeed, the energy difference between the different phases is so small that defects,[256] strain,[251] or other energy contributions can stabilize one phase towards the other. TEM studies in different samples show how FE, FI, and AFE dipole arrangements can exist in different samples prepared under different conditions.[90, 257, 258]

In this appendix, a cost-effective solution process for fabricating high-quality epitaxial single crystal $PbZrO_3$ films on $SrTiO_3$ substrates is discussed. Moreover, the role of defects in the P(E) hysteresis loops of $PbZrO_3$ films is discussed.

A.2 Experimental details

$PbZrO_3$ precursor solution was synthesized from freeze dried lead(II) acetate (99.99%, Merck) and a zirconium(IV) propoxide solution (70% in propanol, Merck). The precursors were dissolved in anhydrous MOE (99.8%, Merck). Acetylacetone (99.5%, Merck) was used as a chelating agent. The mixture was refluxed for two hours under an argon atmosphere. The solution was then distilled and diluted with MOE until it reached a concentration of 0.3 M. A Pb-excess of 20% was used to compensate for PbO sublimation.[259]

$PbZrO_3$ films were deposited by spin coating technique. $SrTiO_3$ and Nb-doped $SrTiO_3$ substrates (Crystal GmbH) were cleaned first in acetone, then in isopropanol, and then in water. Subsequently, the substrates were annealed at 400 °C for 10 minutes before deposition. The precursor solution was spin coated at 3000 rpm for 30 seconds, followed by a drying step at 130 °C for 3 minutes and a pyrolysis step at 350 °C for 3 minutes. The films were crystallized in a rapid thermal annealing furnace (AS-Master, Annealsys) at 700 °C for 5 minutes in air. A thickness of 170 nm is obtained in each annealing cycle. The film thickness was engineered by repeating those steps. $PbZrO_3$ thin films with a thickness of 170 nm, 340 nm, and 680 nm were prepared. To remove surface pyrochlore, a PbO capping layer[260] was deposited on the top and crystallized at 700 °C. The remaining PbO crystals were removed with acetic acid (99.8%, Merck).

To measure the ferroelectric properties, MIM metal capacitors were fabricated as described in Section 3.1.2. The measurement was performed contacting two top electrodes to minimize the presence of imprint fields.[261] This configuration is equivalent to measuring two capacitors in series with a common electrode. The P(E) loops were measured at a frequency of 100 Hz.

A.3 Results and discussion

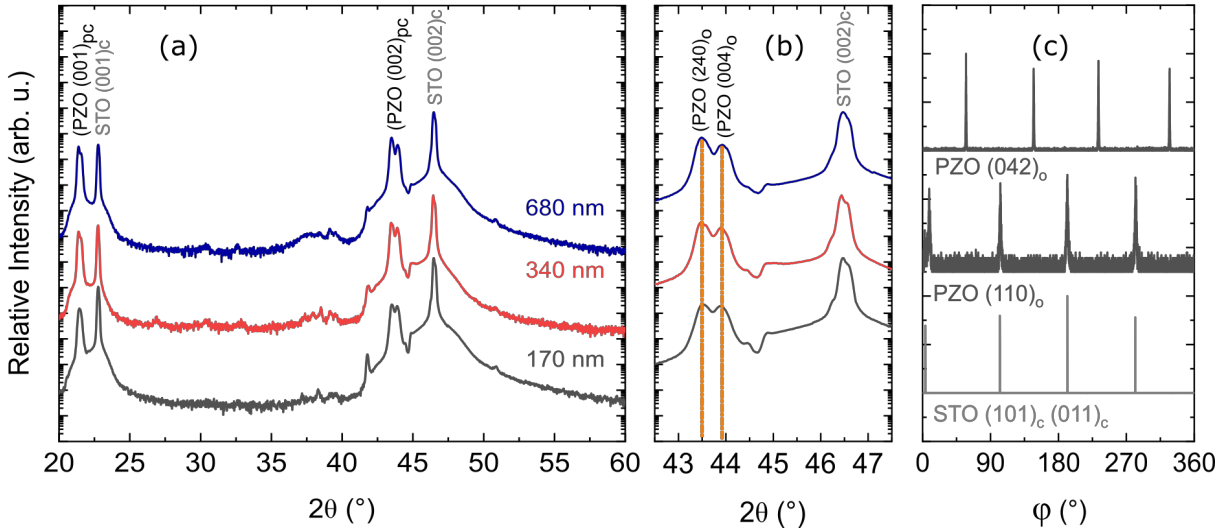

Figure A.1: (a) $\theta - 2\theta$ patterns of the $PbZrO_3$ films with different thicknesses. (b) Detailed view around $(240)_o$ and $(004)_o$ $PbZrO_3$ peaks (vertical lines denote their position according to PDF file No. 01-089-1296). All non-marked peaks correspond to the substrate. (c) Φ-scans of the 170 nm-thick film.

The XRD patterns in Figure A.1 (a) reveal a perfect $(001)_{pc}$ orientation of $PbZrO_3$ films and absence of pyrochlore peaks at all thickness. The $(002)_{pc}$ peak of the film is split into two (Figure A.1 (b)), indicating two out-of-plane crystal domains, i.e., $(120)_o$ and $(002)_o$. Their position matches well the theoretical positions of the orthorhombic Pbma phase. The peaks do not shift with increasing thickness, indicating that there is no significant stress relaxation. Figure A.1 (c) displays the expected four-fold symmetry observed in ϕ-scans. Peaks of the $(110)_o$ domain are at the same position as those of the $(101)_c$ and $(011)_c$ of the $SrTiO_3$ substrate, while peaks of the $(042)_o$ domain are shifted by 45°. These results give the following epitaxial relations: $(120)_o$ $PbZrO_3$||(001) $SrTiO_3$ and [2-10] $PbZrO_3$||[100] $SrTiO_3$ for the $(120)_o$ domain; $(002)_o$ $PbZrO_3$||(001) $SrTiO_3$ and [100] $PbZrO_3$||[110] $SrTiO_3$.

Detailed microstructure of the 170 nm-thick film was analyzed using TEM. High-angle annular dark field (HAADF) and bright-field (BF) scanning TEM micrographs (Figure A.2 (a)–(b)) reveal dense film with some pores present at the interface between the film and the substrate (see circles in Figure A.2 (b)). The

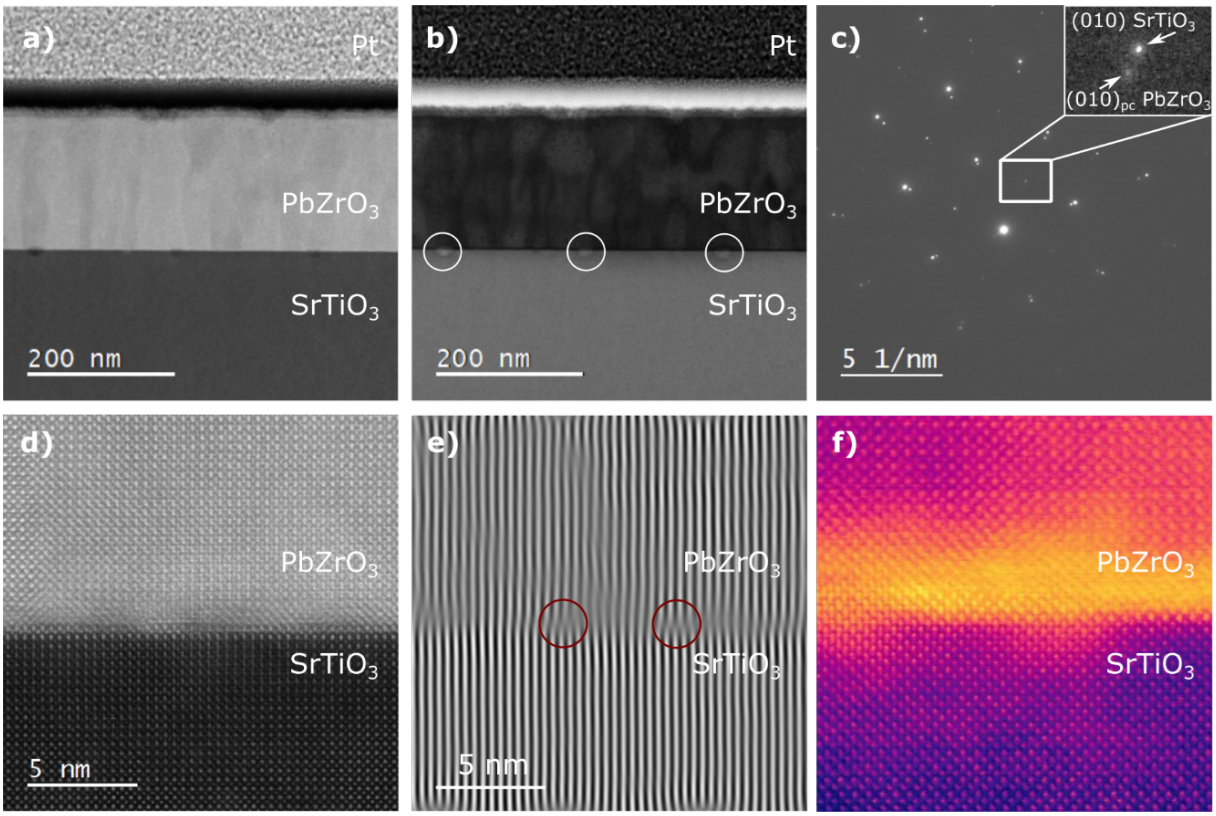

Figure A.2: (a) High-angle annular dark field (HAADF) and (b) bright-field (BF) scanning TEM (STEM) micrographs. (c) Selected area diffraction pattern (SAED) of a wide cross-section of the film. (d) High-resolution (HR HAADF) micrograph of the film/substrate interface. (e) Inverse fast Fourier transform (i-FFT) image and (f) 4D STEM images of the same interface. In b) white circles show pores. In e) red circles show dislocations.

shaded areas in Figure A.2 (a) indicate the formation of different structural domains. $PbZrO_3$ grows in a cubic phase during the crystallization step. During cooling, different structural domain variants are formed, in agreement with Figure A.1 (b).

Figure A.2 (c) shows the selected area diffraction (SAED) of the area depicted in Figure A.2 (a). It indicates that the $PbZrO_3$ is a single crystal, oriented towards the $[100]_{pc}$ direction, which corresponds to the $[120]_o$ and $[002]_o$ orientations. A closer look at the interface quality is shown in Figure A.2 (d). The HAADF TEM micrograph shows the epitaxial growth of $PbZrO_3$ on $SrTiO_3$ with a flat interface. The Inverse fast Fourier transform image in of the same image is shown in Figure A.2 (e). It displays the formation of misfit dislocations at the $PbZrO_3/SrTiO_3$ interface. The strain mapping of the interface $PbZrO_3/SrTiO_3$ (Figure A.2 (f)) indicates that epitaxial strain is relaxed in the first 5 nm, which agrees with the lack of epitaxial strain in the XRD patterns.

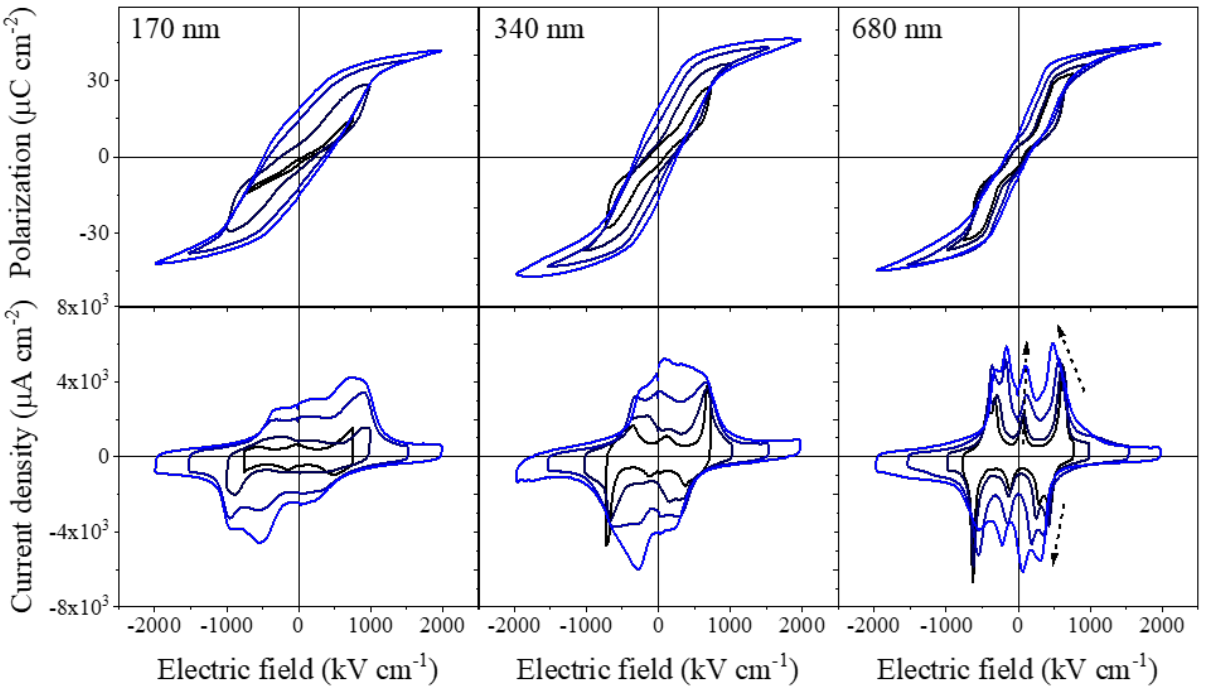

Figure A.3: P(E) loops and j(E) loops of epitaxial $PbZrO_3$ films measured at different electric field amplitudes. The measurements were performed in films with thicknesses of 170 nm, 340 nm and 680 nm.

Figure A.3 shows ferroelectric hysteresis loops under different electric fields for films with different thicknesses. Complex switching curves showing both FE and AFE contributions are observed in all the capacitors. In the 170 nm-thick films, no AFE-like switching is observed at low field or high fields. The switching curves correspond to pinched ferroelectric loops. An AFE-like switching can be observed in the 340 nm-thick and 680 nm-thick films when the films are cycled at low fields. The double hysteresis loops are more pronounced for thicker $PbZrO_3$ films. When the cycling field is increased, both $E_{AFE\rightarrow FE}$ and $E_{FE\rightarrow AFE}$ shift to lower electric fields.

The switching peaks at 50 kV cm^{-1} suggest the presence of a FE-like switching contribution. Similar contributions have been reported in other $PbZrO_3$ films: see [254]. The FE-like contribution at 50 kV cm^{-1} increases when the films are cycled at high fields. As a result, the shape of the loops switches from AFE-like to a pinched FE-like. $E_{AFE\rightarrow FE}$ decreases with increasing film thickness. Additionally, the AFE-switching peaks split at high fields. The films can withstand electric fields up to 2 MV cm^{-2} without electrical breakdown.

To understand the origin of the FE-like contributions in the P(E) loops, a high-resolution TEM study of the 170 nm-thick films was performed. The differential phase contrast (DPC) image of the HAADF TEM micrograph of Figure A.4 (a) is shown in Figure A.4 (b). Areas with different contrast are observed,

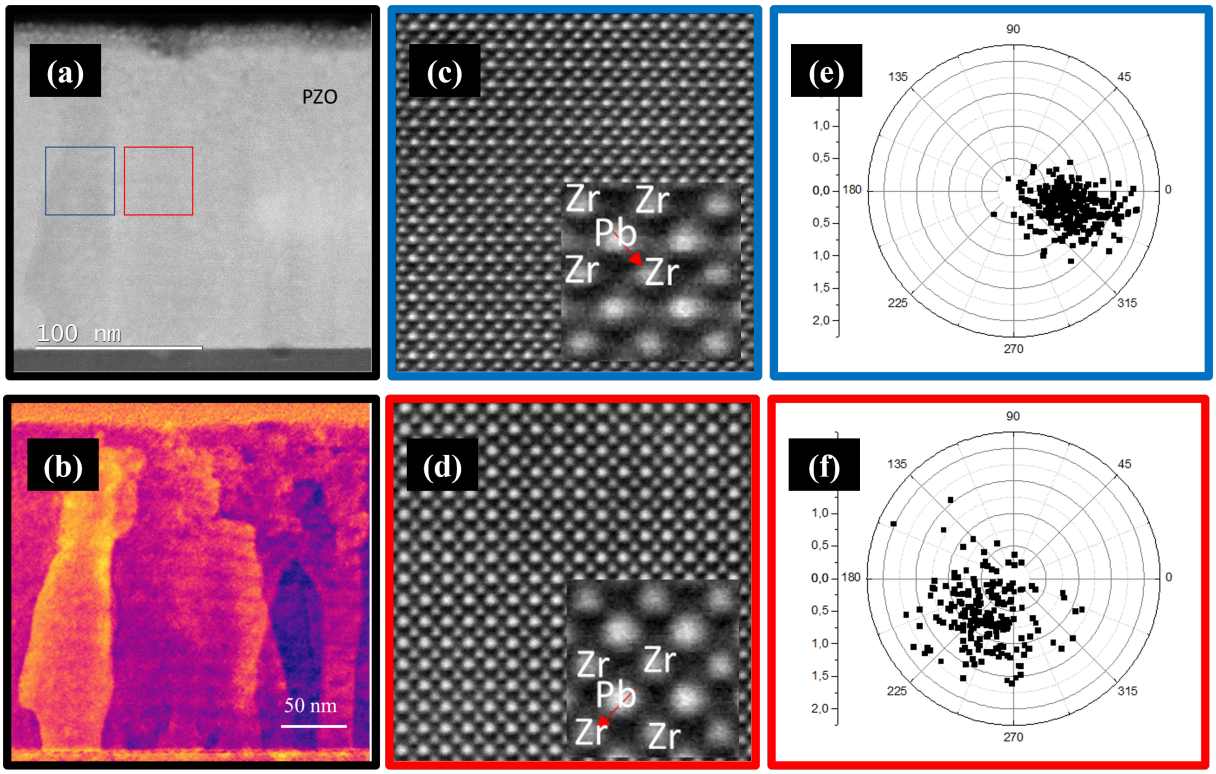

Figure A.4: (a) HAADF TEM micrographs of a $PbZrO_3$ film with a thickness of 170 nm (b) Differential phase contrast (DPC) image of $PbZrO_3$ shows areas with different contrast, due to different polarization orientations. (c) – (d) Atomic resolution HAADF images showing Pb (brighter) and Zr atomic columns. (e) – (f) Polar plots showing orientation and magnitude (in pixels) of Pb and Zr displacements in one unit cell.

indicating the presence of different polarization orientations. Figures A.4 (c) – (d) show the atomic resolution HAADF images that were performed in the blue and red regions of Figure A.4 (a) showing the columns of Pb and Zr atoms. Pb is displaced in the [110] direction. According to Figures A.4 (e) – (f), the polar plots indicate the presence of a net polarization pointing downwards. The TEM results match the electrical macroscopic characterization of the films, indicating the presence of a FE-like behavior.

The observation of ferroelectric-like loops in prototypical antiferroelectric $PbZrO_3$ films has been ascribed to the presence of strain[251] or defects,[256, 262] such as oxygen vacancies or lead vacancies. The presence of strain as a source to stabilize the FE phase can be ruled out since epitaxial strain is relaxed even in the thinner films. Consequently, the FE-like hysteresis loops are more likely to arise due to the presence of defect complexes that pin the antiferroelectric-to-ferroelectric phase boundaries and thus alter the polarization switching behavior.[262] In solution-processed films, the control of stoichiometry remains a challenge. Chemical gradients within the film are commonly observed,[136] which can result in the formation of defects.

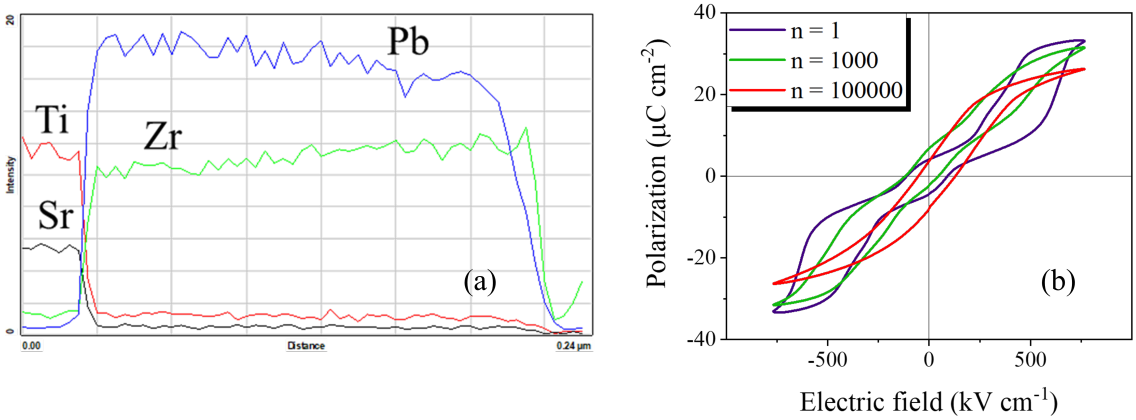

Figure A.5: (a)EDXS line profile mapping of the 170 nm-thick $PbZrO_3$ (b) P(E) loops recorded after bipolar electrical cycling using a triangular signal with an amplitude of 750 $kVcm^{-1}$ in the 680 nm-thick $PbZrO_3$ films.

The presence of a Pb-deficient composition at the surface is confirmed in the EDXS profile mapping in Figure A.5 (a). This points towards the presence of a small surface secondary phase. This may correlate with the 10 nm-thick nano-grained layer present at the top surface in Figure A.2 (b). Additionally, a gradient of the Pb/Zr ratio (more Pb at the film/substrate interface) is observed. Both are typical features of solution-deposited Pb-based perovskites. The crystallization of amorphous $PbZrO_3$ film happens at high temperatures (700 °C). At these high temperatures, there is a competition between PbO sublimation, heterogeneous nucleation of the perovskite on the $SrTiO_3$ surface, and crystal growth. Consequently, the lead content available for the formation of the perovskite is not constant during crystal growth, resulting in chemical gradients and the accumulation of defects at the interfaces. For example, the formation of Pb-vacancies close to the interface of the film can be accommodated either by the generation of the corresponding vacancies in anion sites (V_O) or by altering the valence state of cations.

The defects can be removed upon the crystallization of a second layer on the top. In thinner films, the defect-rich interfaces play a more important role, resulting the in observation of FE-like loops. On the other hand, at larger thicknesses, only a small FE-like contribution can be observed in the AFE-like switching. The application of high electric fields (2 $MV\,cm^{-1}$) as shown in Figure A.3, leads to the electromigration of defects over the whole thickness, that can pin the FE phase.

The same is observed during the repetitive cycling of the 680 nm-thick films as shown in Figure A.5 (b). The first hysteresis curves show a typical AFE-like behavior, with the characteristic double hysteresis loop. However, a non-zero remanent polarization is observed, indicating the presence of ferroelectric (FE) contribution to the hysteresis. Upon cycling, the AFE-like loops shift towards a FE-like loop.

These results suggest that the FE contribution observed in the solution-processed polycrystalline $PbZrO_3$ films of previous report[207, 254] may also be due to the formation of out-of-plane Pb and Zr gradients within the films, that creates defect complexes that pin the antiferroelectric-to-ferroelectric phase boundaries. The formation of defects closer to the interfaces could lead to the pinning of the FE phase in certain regions. In the interdigitated electrode (IDE, in-plane) configuration shown in [248, 254], the electromigration of defects, i.e. oxygen vacancies, within the whole thickness is not possible, (the electric field is applied perpendicular to the chemical gradient) and the FE contribution to the AFE loop remains unchanged upon cycling. Consequently, the stabilization of the AFE phase in epitaxial solution-processed thin films could be achieved by modifying the annealing conditions, e.g., annealing in a Pb-rich atmosphere, or by tuning the Pb excess in the solution.

In summary, a method to prepare epitaxial single crystal $PbZrO_3$ films by solution-deposition methods is shown. Epitaxial strain is relaxed due to the formation of dislocations in the first 5 nm of the films. A FE-like switching behavior is observed in the thinner films while an AFE-like switching behavior is observed in thicker films. Besides, the application of high electric fields or electrical cycling of the films leads to a FE-like switching behavior in all the films. The presence of FE-like loops is associated with the presence of defects such as oxygen vacancies, that redistribute upon the application of high electric fields or electrical cycling. The stabilization of the AFE phase requires an accurate control of the defect chemistry, through the modification of the annealing conditions or by tuning the Pb excess in the solution.

Appendix B

Fast-processing of $BiFeO_3$ films using flash lamp annealing

B.1 Motivation

In solution-processed films, the amorphous deposited film is transformed into a crystalline film via high-temperature annealing. Traditionally, crystallization takes place in tubular or rapid thermal annealing furnaces, where the annealing process occurs at temperatures above 500 °C for tens of minutes or more.

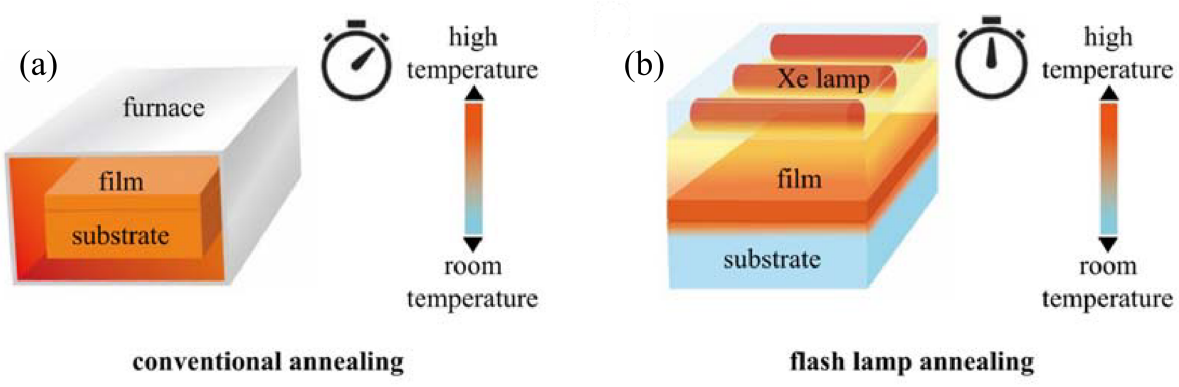

Figure B.1: Schematic representation of annealing processes. Heat distribution in a film, its substrate, and processing time in the case of (a) conventional box furnace annealing and (b) flash lamp annealing. Adapted from [263].

Flash lamp annealing (FLA) offers a solution to overcome the challenges of long crystallization times and high processing temperatures. In this technique, annealing through the absorption of sub-millisecond light pulses with a broad spectrum and strong intensity enables selective annealing of the films on temperature-sensitive substrates.[264] A schematic of the technique in comparison with a conventional rapid thermal annealing furnace is shown in Figure B.1.

FLA can be conducted in a regular atmospheric environment within a few seconds, and it allows for the treatment of large areas, reaching several hundreds of cm^2. These attributes make it suitable for efficient, cost-effective, and high-volume roll-to-roll production.[264] While FLA has been effectively employed in processing various functional materials,[265–267] there are only a few reports regarding its application in crystallizing perovskite oxide thin films. Yao et al. achieved nano-crystallization of piezoelectric lead zirconate titanate on glass and polyimide substrates using FLA. However, they did not demonstrate the macroscopic electromechanical properties essential for sensor and actuator applications.[268]

In this appendix, a cost-effective solution process for fabricating polycrystalline $BiFeO_3$ films using FLA is discussed.

B.2 Experimental details

$BiFeO_3$ films were deposited on fused silica with a crystallized $PbTiO_3$ seed layer fabricated as described in Section 3.1.1. The $BiFeO_3$ solution was spin-coated. Then, the film was heated at 90 °C and at 270 °C on a hot plate. The process was repeated four times until obtaining a film thickness of 100 nm. The crystallization of the layer was performed using a flash lamp annealer (Pulseforge Invent, Novacentrix).

The optimized flash lamp annealing parameters were 50 pulses with a pulse duration of 130 µs and a pulse energy density of $3\,J\,cm^{-2}$. The repetition rate of the pulses was 3.5 Hz. The parameters of the photonic annealing process were optimized by the finite element modeling of the time-dependent temperature profiles in the film, as shown in [263].

After crystallization, IDEs were deposited on the films as described in Section 3.1.2. Electrical characterization was performed as described in Section 3.2.2.

B.3 Results and discussion

Figure B.2 (a) compares the $\theta/2\theta$ scan of BFO/FS crystallized by RTA and FLA. No secondary phases were observed. Both patterns correspond to polycrystalline $BiFeO_3$ with a preferential orientation along the $[100]_{pc}$ direction. The P(E) loops of the FLA and RTA samples are compared in Figure B.2 (b). The

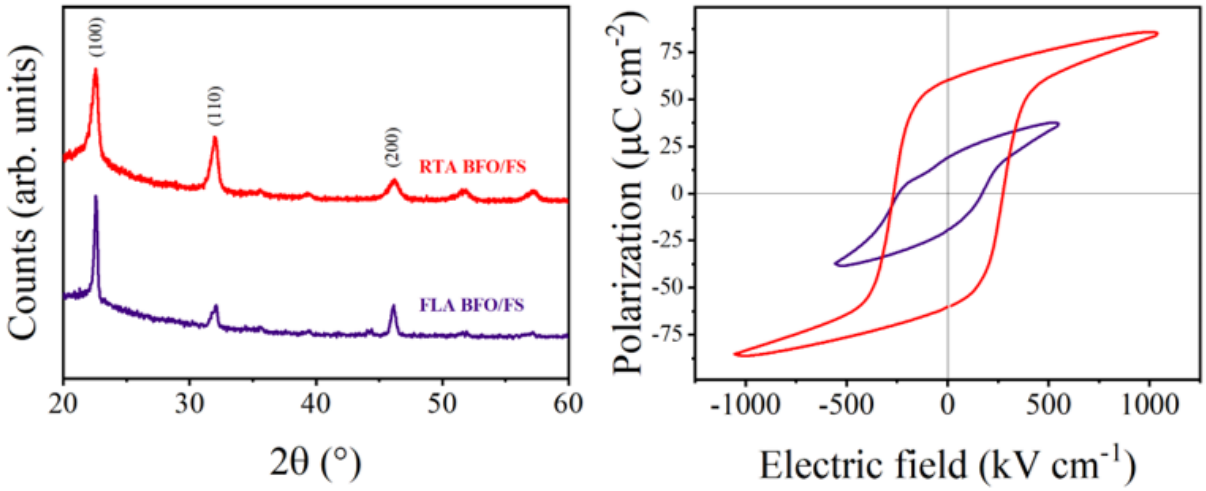

Figure B.2: (a) XRD $\theta/2\theta$ scan and (b) P(E) loops of the BFO/FS crystallized by rapid thermal annealing (RTA) and flash lamp annealing (FLA).

FLA samples show a P_r of 20 μCcm^{-2} and a breakdown field of 600 $kV\,cm^{-1}$. Lower breakdown field and lower remanent polarization are obtained in the FLA films. This is probably due to the high roughness of the FLA samples compared to the RTA samples, which underestimates the area of the IDE capacitor.

Extensive efforts were focused on crystallizing $BiFeO_3$ without a seed layer. However, no perovskite phase was obtained in any of the experiments. The crystallization of $BiFeO_3$ using FLA requires a $PbTiO_3$ seed layer. The presence of a perovskite-based seed layer seems to reduce the crystallization energy of $BiFeO_3$.

In summary, this appendix presents the first-time measurement of macroscopic P(E) loops in FLA $BiFeO_3$ thin films, demonstrating the potential of FLA for the rapid manufacturing of perovskite oxides. One distinctive advantage of FLA is its high compatibility with large-scale roll-to-roll processing. Nevertheless, more efforts are required to achieve the direct crystallization of $BiFeO_3$ by FLA without a $PbTiO_3$ nucleation layer. Different strategies can be investigated to increase the absorbed energy in the film. For example, incorporating organic dyes into the solution or using complexing agents to increase the absorbed energy could overcome the crystallization energy barrier of $BiFeO_3$ without causing damage to the substrate.

Appendix C

Role of electric field distribution in the electro-optic coefficients

C.1 Motivation

The theory described in Section 3.3.2 and the possibility of obtaining a meaningful electro-optic coefficient using IDE geometry relies on the assumption that the applied electric field is homogeneous throughout the entire volume of the sample, which might not be immediately obvious when applying an in-plane electric field with co-planar IDEs.

In this appendix, this limitation is illustrated in the attempt to measure the effective electro-optic coefficients of $LiNbO_3$ single crystals. The role of electric field penetration on the measured electro-optic coefficients is discussed.

C.2 Experimental details

A commercial double-side polished x-cut lithium niobate ($LiNbO_3$) single crystal (Crystal GmbH) with a thickness of 500 µm was used. The crystal has a known effective electro-optic coefficient, r_{eff} of 18 pm V^{-1}.[88] To measure the electro-optic properties, co-planar platinum electrodes separated by a distance of 100 µm were patterned on the x-face, so that the applied electric field is parallel to the z-axis. The electrode deposition was performed as described in Section 3.1.2. The electro-optic coefficients were measured as discussed in Section 3.3.2.

C.3 Results and discussion

As described in Section 3.3.2, upon alignment of the laser between the co-planar electrodes, the voltage at the photodiode, V_{PD}, was measured as a function of the phase controller phase shift. Then, a unipolar sinusoidal electrical signal with a frequency of 1 kHz and an amplitude of 150 V, resulting in an electric field of 15 kV cm^{-1}, was applied and the demodulation voltage amplitude, V_{LI}, and phase from the lock-in amplifier were recorded as a function of the phase controller phase shift.

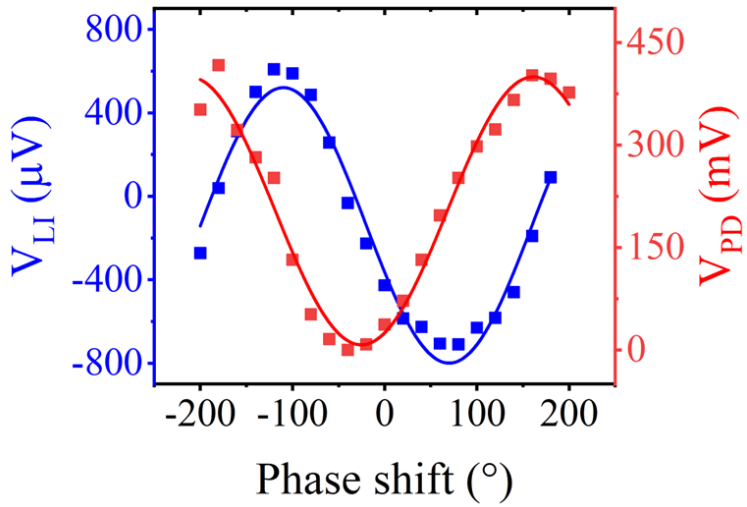

Figure C.1: V_{LI} and V_{PD} curves for a commercial $LiNbO_3$ single crystal measured using a Teng-Man set-up in transmission geometry with a driving field of 15 kV cm^{-1}.

The V_{PD} and V_{LI} as a function of the phase controller phase shift are displayed in Figure C.1. Under these conditions V^0_{PD} has a value of 420 mV. This corresponds to a 2π phase shift of the 45° polarized incoming light. On the other hand, V^0_{LI} has a value of 1.32 mV. Using these values, r_{eff} can be calculated using the equation described in Section 3.3.2:

$$r_{\text{eff}} = r_{33} - r_{13}\frac{n_o^3}{n_e^3} = \frac{\lambda V^0_{\text{LI}}}{\pi n_e^3 L_{\text{LNO}} A V^0_{\text{PD}}} \tag{C.1}$$

Using the extraordinary refractive index of $LiNbO_3$, $n_e = 2.2$, and the thickness of the single crystal, a r_{eff} of 0.08 pm V^{-1} is calculated, significantly underestimating the standard value. Between the possible origins of this underestimation, the insufficient field penetration along the whole thickness of the crystal seems to be the most plausible option.

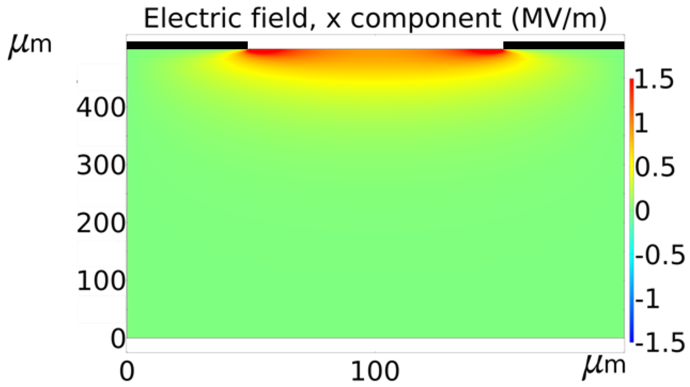

Figure C.2: Simulated electric field distribution in a $LiNbO_3$ single crystal. The black lines indicate the co-planar platinum pads on the surface of the crystal.

To estimate the field penetration, the in-plane component of the electric field distribution was numerically simulated by the Finite Element Method with the COMSOL software package, with a voltage of 150 V applied between the co-planar electrodes. The simulated in-plane component of the electric field distribution in the crystal is shown in Figure C.2. The simulations indicate that the electric field is confined to the surface of the crystal, showing a gradient along the electrode gap and the thickness of the crystal. Indeed, the correct r_{eff} is only obtained considering an active thickness of 2.2 μm. These results indicate that even if the phase shift induced in our ferroelectric upon the presence of an electric field can be measured in this geometry, special attention must be paid to the real penetration of the electric field in the crystal.

In summary, one of the main disadvantages of TM measurements in transmission geometry is the assumption that the applied electric field is homogeneous throughout the entire volume of the sample. In conventional IDEs, the electric field is applied from the surface of the film and produces a curved electric field that penetrates through the thickness of the material. The distribution of the electric field along the whole thickness depends on the distance between the IDE fingers among other parameters. An effective distribution of the electric field along the whole thickness can only be achieved in devices where the distance between the electrodes is one order of magnitude larger than the thickness of the material, i.e., thin films.

References

[1]M. E. Lines and A. M. Glass, *Principles and Applications of Ferroelectrics and Related Materials* (Oxford University Press, 2001).

[2]B. I. Sturman and V. M. Fridkin, *The Photovoltaic and Photorefractive Effects in Noncentrosymmetric Materials* (Routledge, 1992).

[3]Robert W. Boyd, *Nonlinear Optics. Third Edition.* (Academic Press, 2008).

[4]V. M. Fridkin, *Photoferroelectrics*, Vol. 9, Springer Series in Solid-State Sciences (Springer Berlin Heidelberg, 1979).

[5]C. Paillard, X. Bai, I. C. Infante, M. Guennou, G. Geneste, M. Alexe, J. Kreisel, and B. Dkhil, "Photovoltaics with Ferroelectrics: Current Status and Beyond", Advanced Materials **28**, 5153–5168 (2016).

[6]P. Würfel, *Physics of Solar Cells* (Wiley, 2005).

[7]V. M. Fridkin, "Bulk photovoltaic effect in noncentrosymmetric crystals", Crystallography Reports **46**, 654–658 (2001).

[8]A. Pusch, U. Römer, D. Culcer, and N. J. Ekins-Daukes, "Energy Conversion Efficiency of the Bulk Photovoltaic Effect", PRX Energy **2**, 013006 (2023).

[9]J. Kreisel, M. Alexe, and P. A. Thomas, "A photoferroelectric material is more than the sum of its parts", Nature Materials **11**, 260 (2012).

[10]S. Y. Yang, J. Seidel, S. J. Byrnes, P. Shafer, C.-H. Yang, M. D. Rossell, P. Yu, Y.-H. Chu, J. F. Scott, J. W. Ager, L. W. Martin, and R. Ramesh, "Above-bandgap voltages from ferroelectric photovoltaic devices", Nature Nanotechnology **5**, 143–147 (2010).

[11]V. M. Fridkin and B. N. Popov, "Anomalous photovoltaic effect in ferroelectrics", Sov. Phys Usp. **21**, 981–991 (1978).

[12]K. Uchiho, "New applications of photostrictive ferroics", Materials Research Innovations **1**, 163–168 (1997).

[13]B. Kundys, "Photostrictive materials", Applied Physics Reviews **2**, 011301 (2015).

[14]C. Chen and Z. Yi, "Photostrictive Effect: Characterization Techniques, Materials, and Applications", Advanced Functional Materials **31**, 2010706 (2021).

[15]D. Kip, "Photorefractive waveguides in oxide crystals: fabrication, properties, and applications", Applied Physics B: Lasers and Optics **67**, 131–150 (1998).

[16]M. Haw, "The light fantastic", Nature **422**, 556–558 (2003).

[17]L. Dhar, K. Curtis, and T. Fäcke, "Coming of age", Nature Photonics **2**, 403–405 (2008).

[18]A. M. Glass, D. von der Linde, and T. J. Negran, "High-voltage bulk photovoltaic effect and the photorefractive process in $LiNbO_3$", Applied Physics Letters **25**, 233–235 (1974).

[19]B. L. Volodin, C. Halvorson, B. Kraabel, K. Meerholz, Sandalphon, A. J. Heeger, and N. Peyghambarian, "Optical computing by use of photorefractive polymers", Optics Letters **20**, 76 (1995).

[20]T. Choi, S. Lee, Y. J. Choi, V. Kiryukhin, and S.-W. Cheong, "Switchable Ferroelectric Diode and Photovoltaic Effect in $BiFeO_3$", Science **324**, 63–66 (2009).

[21]H. T. Yi, T. Choi, S. G. Choi, Y. S. Oh, and S.-W. Cheong, "Mechanism of the Switchable Photovoltaic Effect in Ferroelectric $BiFeO_3$", Advanced Materials **23**, 3403–3407 (2011).

[22]M. C. Weber, M. Guennou, C. Toulouse, M. Cazayous, Y. Gillet, X. Gonze, and J. Kreisel, "Temperature evolution of the band gap in $BiFeO_3$ traced by resonant Raman scattering", Physical Review B **93**, 125204 (2016).

[23]J. Li, J. Wang, M. Wuttig, R. Ramesh, N. Wang, B. Ruette, A. P. Pyatakov, A. K. Zvezdin, and D. Viehland, "Dramatically enhanced polarization in (001), (101), and (111) $BiFeO_3$ thin films due to epitiaxial-induced transitions", Applied Physics Letters **84**, 5261–5263 (2004).

[24]J. T. Heron, J. L. Bosse, Q. He, Y. Gao, M. Trassin, L. Ye, J. D. Clarkson, C. Wang, J. Liu, S. Salahuddin, D. C. Ralph, D. G. Schlom, J. Íñiguez, B. D. Huey, and R. Ramesh, "Deterministic switching of ferromagnetism at room temperature using an electric field", Nature **516**, 370–373 (2014).

[25]S. Nadupalli, J. Kreisel, and T. Granzow, "Increasing bulk photovoltaic current by strain tuning", Science Advances **5**, eaau9199 (2019).

[26]J. Valasek, "Piezo-Electric and Allied Phenomena in Rochelle Salt", Physical Review **17**, 475–481 (1921).

[27]B. A. Strukov and A. P. Levanyuk, *Ferroelectric Phenomena in Crystals* (Springer Berlin Heidelberg, 1998).

[28]R. R. Mehta, B. D. Silverman, and J. T. Jacobs, "Depolarization fields in thin ferroelectric films", Journal of Applied Physics **44**, 3379–3385 (1973).

[29]P. Wurfel, I. P. Batra, and J. T. Jacobs, "Polarization Instability in Thin Ferroelectric Films", Physical Review Letters **30**, 1218–1221 (1973).

[30]A. K. Tagantsev, I. Stolichnov, E. L. Colla, and N. Setter, "Polarization fatigue in ferroelectric films: Basic experimental findings, phenomenological scenarios, and microscopic features", Journal of Applied Physics **90**, 1387–1402 (2001).

[31]D. Meier, J. Seidel, M. Gregg, and R. Ramesh, *Domain Walls* (Oxford University Press, 2020).

[32]L. Wang, X. Wang, and J. Shi, "Measurement and estimation of ferroelectric hysteresis loops", Ferroelectrics **411**, 86–92 (2011).

[33]R. Waser, U. Böttger, and S. Tiedke, *Polar Oxides: Properties, Characterization, and Imaging* (Wiley, 2004).

[34]E. Defaÿ, *Integration of Ferroelectric and Piezoelectric Thin Films* (Wiley, 2011).

[35]H. Ishiwara, M. Okuyama, and Y. Arimoto, *Ferroelectric Random Access Memories* (Springer Berlin Heidelberg, 2004).

[36]I. P. Kaminow, *An Introduction to Electrooptic Devices* (Elsevier, 1974).

[37]S. M. Sze and K. K. Ng, *Physics of Semiconductor Devices: Third Edition* (Wiley, 2006).

[38]J.-F. Guillemoles, T. Kirchartz, D. Cahen, and U. Rau, "Guide for the perplexed to the Shockley–Queisser model for solar cells", Nature Photonics **13**, 501–505 (2019).

[39]W. Shockley and H. J. Queisser, "Detailed Balance Limit of Efficiency of p-n Junction Solar Cells", Journal of Applied Physics **32**, 510–519 (1961).

[40]N. F. Mott, "Note on the contact between a metal and an insulator or semi-conductor", Mathematical Proceedings of the Cambridge Philosophical Society **34**, 568–572 (1938).

[41]D. Lee, S. H. Baek, T. H. Kim, J. G. Yoon, C. M. Folkman, C. B. Eom, and T. W. Noh, "Polarity control of carrier injection at ferroelectric/metal interfaces for electrically switchable diode and photovoltaic effects", Physical Review B **84**, 1–9 (2011).

[42]L. Pintilie, C. Dragoi, and I. Pintilie, "Interface controlled photovoltaic effect in epitaxial Pb(Zr,Ti)O_3 films with tetragonal structure", Journal of Applied Physics **110**, 044105 (2011).

[43]P. Lopez-Varo, L. Bertoluzzi, J. Bisquert, M. Alexe, M. Coll, J. Huang, J. A. Jimenez-Tejada, T. Kirchartz, R. Nechache, F. Rosei, and Y. Yuan, "Physical aspects of ferroelectric semiconductors for photovoltaic solar energy conversion", Physics Reports **653**, 1–40 (2016).

[44]L. You, A. Abdelsamie, Y. Zhou, L. Chang, Z. S. Lim, and J. Wang, "Revisiting the Ferroelectric Photovoltaic Properties of Vertical $BiFeO_3$ Capacitors: A Comprehensive Study", ACS Applied Materials & Interfaces **15**, 12070–12077 (2023).

[45]A. Grillo and A. Di Bartolomeo, "A Current–Voltage Model for Double Schottky Barrier Devices", Advanced Electronic Materials **7**, 2000979 (2021).

[46]Z. Dai and A. M. Rappe, "Recent progress in the theory of bulk photovoltaic effect", Chemical Physics Reviews **4**, 011303 (2023).

[47]H. Dember, "Über eine photoelektronische Kraft in Kupferoxydul-Kristallen", Phys. Z. **32**, 554 (1931).

[48]a. G. Chynoweth, "Surface Space-Charge Layers in Barium Titanate", Physical Review **102**, 705–714 (1956).

[49]W. T. H. Koch, R. Munser, W. Ruppel, and P. Würfel, "Anomalous photovoltage in $BaTiO_3$", Ferroelectrics **13**, 305–307 (1976).

[50]K. Buse, H. Hesse, U. Stevendaal, S. Loheide, D. Sabbert, and E. Krtzig, "Photorefractive properties of ruthenium-doped potassium niobate", Applied Physics A Solids and Surfaces **59**, 563–567 (1994).

[51]H. G. Festl, P. Hertel, E. Krätzig, and R. von Baltz, "Investigations of the Photovoltaic Tensor in Doped $LiNbO_3$", physica status solidi (b) **113**, 157–164 (1982).

[52]P. S. Brody and F. Crowne, "Mechanism for the high voltage photovoltaic effect in ceramic ferroelectrics", Journal of Electronic Materials **4**, 955–971 (1975).

[53]A. M. Glass, D. von der Linde, D. H. Auston, and T. J. Negran, "Excited state polarization, bulk photovoltaic effect and the photorefractive effect in electrically polarized media", Journal of Electronic Materials **4**, 915–943 (1975).

[54]S.-Y. Chu, Z. Ye, and K. Uchino, "Photovoltaic effect for the linearly polarized light in $(Pb,La)(Zr,Ti)O_3$ ceramics", Smart Materials and Structures **3**, 114–117 (1994).

[55]K. Nonaka, M. Akiyama, T. Hagio, and A. Takase, "Bulk Photovoltaic Effect in Reduced/Oxidized Lead Lanthanum Titanate Zirconate Ceramics", Japanese Journal of Applied Physics **34**, 2344 (1995).

[56]V. I. Belinicher and B. I. Sturman, "The photogalvanic effect in media lacking a center of symmetry", Soviet Physics - Uspekhi **23**, 199–223 (1980).

[57]V. I. Belinicher and B. I. Sturman, "The relation between shift and ballistic currents in the theory of photogalvanic effect", Ferroelectrics **83**, 29–34 (1988).

[58]B. I. Sturman, "Ballistic and shift currents in the bulk photovoltaic effect theory", Uspekhi Fizicheskih Nauk **190**, 441–445 (2020).

[59]J. Ahn, G.-Y. Guo, and N. Nagaosa, "Low-Frequency Divergence and Quantum Geometry of the Bulk Photovoltaic Effect in Topological Semimetals", Physical Review X **10**, 041041 (2020).

[60]S. M. Young, F. Zheng, and A. M. Rappe, "First-Principles Calculation of the Bulk Photovoltaic Effect in Bismuth Ferrite", Physical Review Letters **109**, 236601 (2012).

[61]S. M. Young and A. M. Rappe, "First Principles Calculation of the Shift Current Photovoltaic Effect in Ferroelectrics", Physical Review Letters **109**, 116601 (2012).

[62]S. M. Young, F. Zheng, and A. M. Rappe, "First-principles materials design of high-performing bulk photovoltaics with the $LiNbO_3$ structure", Physical Review Applied **4**, 1–8 (2015).

[63]L. Z. Tan, F. Zheng, S. M. Young, F. Wang, S. Liu, and A. M. Rappe, "Shift current bulk photovoltaic effect in polar materials—hybrid and oxide perovskites and beyond", npj Computational Materials **2**, 16026 (2016).

[64]A. M. Burger, R. Agarwal, A. Aprelev, E. Schruba, A. Gutierrez-Perez, V. M. Fridkin, and J. E. Spanier, "Direct observation of shift and ballistic photovoltaic currents", Science Advances **5**, eaau5588 (2019).

[65]J. E. Spanier, V. M. Fridkin, A. M. Rappe, A. R. Akbashev, A. Polemi, Y. Qi, Z. Gu, S. M. Young, C. J. Hawley, D. Imbrenda, G. Xiao, A. L. Bennett-Jackson, and C. L. Johnson, "Power conversion efficiency exceeding the Shockley-Queisser limit in a ferroelectric insulator", Nature Photonics **10**, 611–616 (2016).

[66] A. P. Kirk and D. W. Cardwell, "Reconsidering the Shockley–Queisser limit of a ferroelectric insulator device", Nature Photonics **11**, 329–329 (2017).

[67] W. Gong, J.-F. Li, X. Chu, Z. Gui, and L. Li, "Preparation and characterization of sol–gel derived (100)-textured Pb(Zr,Ti)O_3 thin films: PbO seeding role in the formation of preferential orientation", Acta Materialia **52**, 2787–2793 (2004).

[68] Y. Dong, M.-M. Yang, M. Yoshii, S. Matsuoka, S. Kitamura, T. Hasegawa, N. Ogawa, T. Morimoto, T. Ideue, and Y. Iwasa, "Giant bulk piezophotovoltaic effect in 3R-MoS_2", Nature Nanotechnology **18**, 36–41 (2023).

[69] M.-M. Yang, D. J. Kim, and M. Alexe, "Flexo-photovoltaic effect", Science **360**, 904–907 (2018).

[70] A. M. Schankler, L. Gao, and A. M. Rappe, "Large Bulk Piezophotovoltaic Effect of Monolayer 2 H-MoS_2", The Journal of Physical Chemistry Letters **12**, 1244–1249 (2021).

[71] H. Ai, Y. Kong, D. Liu, F. Li, J. Geng, S. Wang, K. H. Lo, and H. Pan, "1T Transition-Metal Dichalcogenides: Strong Bulk Photovoltaic Effect for Enhanced Solar-Power Harvesting", The Journal of Physical Chemistry C **124**, 11221–11228 (2020).

[72] N. T. Kaner, Y. Wei, Y. Jiang, W. Li, X. Xu, K. Pang, X. Li, J. Yang, Y. Jiang, G. Zhang, and W. Q. Tian, "Enhanced Shift Currents in Monolayer 2D GeS and SnS by Strain-Induced Band Gap Engineering", ACS Omega **5**, 17207–17214 (2020).

[73] R. Nechache, C. Harnagea, S. Li, L. Cardenas, W. Huang, J. Chakrabartty, and F. Rosei, "Bandgap tuning of multiferroic oxide solar cells", Nature Photonics **9**, 61–67 (2014).

[74] T. Yang, J. Wei, Y. Guo, Z. Lv, Z. Xu, and Z. Cheng, "Manipulation of Oxygen Vacancy for High Photovoltaic Output in Bismuth Ferrite Films", ACS Applied Materials & Interfaces **11**, 23372–23381 (2019).

[75] C. Paillard, X. Bai, I. C. Infante, M. Guennou, G. Geneste, M. Alexe, J. Kreisel, and B. Dkhil, "Photovoltaics with Ferroelectrics: Current Status and Beyond", Advanced Materials **28**, 5153–5168 (2016).

[76] B. Kundys, M. Viret, D. Colson, and D. O. Kundys, "Light-induced size changes in $BiFeO_3$ crystals", Nature Materials **9**, 803–805 (2010).

[77] M. M. Yang and M. Alexe, "Light-Induced Reversible Control of Ferroelectric Polarization in $BiFeO_3$", Advanced Materials **30**, 1–6 (2018).

[78] I. C. Amaechi, A. Hadj Youssef, A. Dörfler, Y. González, R. Katoch, and A. Ruediger, "Catalytic Applications of Non-Centrosymmetric Oxide Nanomaterials", Angewandte Chemie International Edition **61**, 10.1002/anie.202207975 (2022).

[79] A. K. Hamze and A. A. Demkov, "First-principles study of the linear electro-optical response in strained $SrTiO_3$", Physical Review Materials **2**, 115202 (2018).

[80] M. Veithen, X. Gonze, and P. Ghosez, "First-Principles Study of the Electro-Optic Effect in Ferroelectric Oxides", Physical Review Letters **93**, 187401 (2004).

[81]C. Chen, H. Yang, Z. Wang, and Z. Lin, "A theoretical model to calculate linear electro-optic effect in crystals", Chemical Physics Letters **397**, 222–226 (2004).

[82]X. Y. Meng, Z. Z. Wang, Y. Zhu, and C. T. Chen, "Mechanism of the electro-optic effect in the perovskite-type ferroelectric $KNbO_3$ and $LiNbO_3$", Journal of Applied Physics **101**, 103506 (2007).

[83]F. Wang, "Calculation of the electro-optical and nonlinear optical coefficients of ferroelectric materials from their linear properties", Physical Review B **59**, 9733–9736 (1999).

[84]L. Guilbert, J. P. Salvestrini, M. D. Fontana, and Z. Czapla, "Correlation between dielectric and electro-optic properties related to domain dynamics in $RbHSeO_4$ crystals", Physical Review B **58**, 2523–2528 (1998).

[85]V. Ivanov, "Direct electro-optic effect in langasites and α-quartz", Optical Materials **79**, 1–7 (2018).

[86]B. W. Wessels, "Ferroelectric Epitaxial Thin Films for Integrated Optics", Annual Review of Materials Research **37**, 659–679 (2007).

[87]Y. Qi and Y. Li, "Integrated lithium niobate photonics", Nanophotonics **9**, 1287–1320 (2020).

[88]J. D. Zook, D. Chen, and G. N. Otto, "Temperature dependence and model of the electro-optic effect in $LiNbO_3$", Applied Physics Letters **11**, 159–161 (1967).

[89]M. Zgonik, P. Bernasconi, M. Duelli, R. Schlesser, P. Günter, M. H. Garrett, D. Rytz, Y. Zhu, and X. Wu, "Dielectric, elastic, piezoelectric, electro-optic, and elasto-optic tensors of $BaTiO_3$ crystals", Physical Review B **50**, 5941–5949 (1994).

[90]X. Liu, P. Tan, X. Ma, D. Wang, X. Jin, Y. Liu, B. Xu, L. Qiao, C. Qiu, B. Wang, W. Zhao, C. Wei, K. Song, H. Guo, X. Li, S. Li, X. Wei, L.-Q. Chen, Z. Xu, F. Li, H. Tian, and S. Zhang, "Ferroelectric crystals with giant electro-optic property enabling ultracompact Q-switches", Science **376**, 371–377 (2022).

[91]E.-D. 2002/95/EC, "Restriction of the Use of Certain Hazardous Substances in Electrical and Electronic Equipment (RoHS).", Off. J. Eur. Union **46**, 19–23 (2003).

[92]R. S. Jacobsen, K. N. Andersen, P. I. Borel, J. Fage-Pedersen, L. H. Frandsen, O. Hansen, M. Kristensen, A. V. Lavrinenko, G. Moulin, H. Ou, C. Peucheret, B. Zsigri, and A. Bjarklev, "Strained silicon as a new electro-optic material", Nature **441**, 199–202 (2006).

[93]A. W. Fang, B. R. Koch, Jae Shin, E. J. Norberg, E. Hall, and G. Fish, "Heterogeneous integration on silicon photonics", in 2013 conference on lasers and electro-optics pacific rim (cleopr) (June 2013), pp. 1–2.

[94]F. Eltes, C. Mai, D. Caimi, M. Kroh, Y. Popoff, G. Winzer, D. Petousi, S. Lischke, J. Elliott Ortmann, L. Czornomaz, L. Zimmermann, J. Fompeyrine, and S. Abel, "A $BaTiO_3$-Based Electro-Optic Pockels Modulator Monolithically Integrated on an Advanced Silicon Photonics Platform", Journal of Lightwave Technology **37**, 1456–1462 (2019).

[95]S. Abel, F. Eltes, J. E. Ortmann, A. Messner, P. Castera, T. Wagner, D. Urbonas, A. Rosa, A. M. Gutierrez, D. Tulli, P. Ma, B. Baeuerle, A. Josten, W. Heni, D. Caimi, L. Czornomaz, A. A. Demkov, J. Leuthold, P. Sanchis, and J. Fompeyrine, "Large Pockels effect in micro- and nanostructured barium titanate integrated on silicon", Nature Materials **18**, 42–47 (2019).

[96]G. Catalan and J. F. Scott, "Physics and applications of bismuth ferrite", Advanced Materials **21**, 2463–2485 (2009).

[97]G. A. Smolenskiĭ and I. E. Chupis, "Ferroelectromagnets", Soviet Physics Uspekhi **25**, 475–493 (1982).

[98]S.-H. Baek, C. M. Folkman, J.-W. Park, S. Lee, C.-W. Bark, T. Tybell, and C.-B. Eom, "The Nature of Polarization Fatigue in $BiFeO_3$", Advanced Materials **23**, 1621–1625 (2011).

[99]D. Sando, Y. Yang, C. Paillard, B. Dkhil, L. Bellaiche, and V. Nagarajan, "Epitaxial ferroelectric oxide thin films for optical applications", Applied Physics Reviews **5**, 041108 (2018).

[100]I. Bozovic and J. Eckstein, "Analysis of Growing Films of Complex Oxides by RHEED", MRS Bulletin **20**, 32–38 (1995).

[101]D. H. Blank, G. J. Rijnders, G. Koster, and H. Rogalla, "In-situ monitoring during pulsed laser deposition using RHEED at high pressure", Applied Surface Science **127-129**, 633–638 (1998).

[102]P. Muralt, "Ferroelectric thin films for micro-sensors and actuators: a review", Journal of Micromechanics and Microengineering **10**, 136–146 (2000).

[103]T. Schneller, R. Waser, M. Kosec, and D. Payne, *Chemical Solution Deposition of Functional Oxide Thin Films* (Springer Vienna, 2013).

[104]A. Kareiva, I. Bryntse, M. Karppinen, and L. Niinistö, "Influence of Complexing Agents on Properties of $YBa_2Cu_4O_8$ Superconductors Prepared by the Sol-Gel Method", Journal of Solid State Chemistry **121**, 356–361 (1996).

[105]Y. Narendar and G. L. Messing, "Mechanisms of phase separation in gel-based synthesis of multicomponent metal oxides", Catalysis Today **35**, 247–268 (1997).

[106]L. E. Scriven, "Physics and Applications of DIP Coating and Spin Coating", MRS Proceedings **121**, 717 (1988).

[107]M. Tomczyk, A. Mahajan, A. Tkach, and P. M. Vilarinho, "Interface-based reduced coercivity and leakage currents of $BiFeO_3$ thin films: A comparative study", Materials & Design **160**, 1322–1334 (2018).

[108]C. Gutiérrez-Lázaro, I. Bretos, R. Jiménez, J. Ricote, H. E. Hosiny, D. Pérez-Mezcua, R. J. Jiménez Rioboõ, M. García-Hernández, and M. L. Calzada, "Solution synthesis of $BiFeO_3$ thin films onto silicon substrates with ferroelectric, magnetic, and optical functionalities", Journal of the American Ceramic Society **96**, 3061–3069 (2013).

[109]C. Ederer and N. A. Spaldin, "Influence of strain and oxygen vacancies on the magnetoelectric properties of multiferroic bismuth ferrite", Physical Review B **71**, 224103 (2005).

[110]M. Schrade, N. Masó, A. Perejón, L. A. Pérez-Maqueda, and A. R. West, "Defect chemistry and electrical properties of $BiFeO_3$", J. Mater. Chem. C **5**, 10077–10086 (2017).

[111]J. Wu, J. Wang, D. Xiao, and J. Zhu, "Migration Kinetics of Oxygen Vacancies in Mn-Modified $BiFeO_3$ Thin Films", ACS Applied Materials & Interfaces **3**, 2504–2511 (2011).

[112]I. Bretos, R. Jiménez, C. Gutiérrez-Lázaro, I. Montero, and M. L. Calzada, "Defect-mediated ferroelectric domain depinning of polycrystalline $BiFeO_3$ multiferroic thin films", Applied Physics Letters **104**, 092905 (2014).

[113]T. Rojac, A. Bencan, B. Malic, G. Tutuncu, J. L. Jones, J. E. Daniels, and D. Damjanovic, " $BiFeO_3$ Ceramics: Processing, Electrical, and Electromechanical Properties", Journal of the American Ceramic Society **97**, 1993–2011 (2014).

[114]S. M. Selbach, M. A. Einarsrud, and T. Grande, "On the thermodynamic stability of $BiFeO_3$", Chemistry of Materials **21**, 169–173 (2009).

[115]H. Béa, M. Bibes, A. Barthélémy, K. Bouzehouane, E. Jacquet, A. Khodan, J.-P. Contour, S. Fusil, F. Wyczisk, A. Forget, D. Lebeugle, D. Colson, and M. Viret, "Influence of parasitic phases on the properties of $BiFeO_3$ epitaxial thin films", Applied Physics Letters **87**, 1–4 (2005).

[116]C.-C. Leu, T.-J. Lin, S.-Y. Chen, and C.-T. Hu, "Effects of Bismuth Oxide Buffer Layer on $BiFeO_3$ Thin Film", Journal of the American Ceramic Society **98**, edited by P. Paranthaman, 724–731 (2015).

[117]X. Qi, J. Dho, R. Tomov, M. G. Blamire, and J. L. MacManus-Driscoll, "Greatly reduced leakage current and conduction mechanism in aliovalent-ion-doped $BiFeO_3$", Applied Physics Letters **86**, 062903 (2005).

[118]Y. Noguchi, H. Matsuo, Y. Kitanaka, and M. Miyayama, "Ferroelectrics with a controlled oxygen-vacancy distribution by design", Scientific Reports **9**, 4225 (2019).

[119]S. K. Singh, H. Ishiwara, and K. Maruyama, "Room temperature ferroelectric properties of Mn-substituted $BiFeO_3$ thin films deposited on Pt electrodes using chemical solution deposition", Applied Physics Letters **88**, 262908 (2006).

[120]S. K. Singh, H. Ishiwara, K. Sato, and K. Maruyama, "Microstructure and frequency dependent electrical properties of Mn-substituted $BiFeO_3$ thin films", Journal of Applied Physics **102**, 094109 (2007).

[121]C. Yang, Y. Han, J. Qian, P. Lv, X. Lin, S. Huang, and Z. Cheng, "Flexible, Temperature-Resistant, and Fatigue-Free Ferroelectric Memory Based on $BiFe_{0.93}Mn_{0.05}Ti_{0.02}O_3$ Thin Film", ACS Applied Materials & Interfaces **11**, 12647–12655 (2019).

[122]T. Kawae, Y. Terauchi, H. Tsuda, M. Kumeda, and A. Morimoto, "Improved leakage and ferroelectric properties of Mn and Ti codoped $BiFeO_3$ thin films", Applied Physics Letters **94**, 112904 (2009).

[123]M. Yang, A. Bhatnagar, and M. Alexe, "Electronic Origin and Tailoring of Photovoltaic Effect in $BiFeO_3$ Single Crystals", Advanced Electronic Materials **1**, 1500139 (2015).

[124]T. Rojac, A. Bencan, G. Drazic, N. Sakamoto, H. Ursic, B. Jancar, G. Tavcar, M. Makarovic, J. Walker, B. Malic, and D. Damjanovic, "Domain-wall conduction in ferroelectric $BiFeO_3$ controlled by accumulation of charged defects", Nature Materials **16**, 322–327 (2017).

[125]P. Machado, M. Scigaj, J. Gazquez, E. Rueda, A. Sánchez-Díaz, I. Fina, M. Gibert-Roca, T. Puig, X. Obradors, M. Campoy-Quiles, and M. Coll, "Band Gap Tuning of Solution-Processed Ferroelectric Perovskite $BiFe_{1-x}Co_xO_3$ Thin Films", Chemistry of Materials **31**, 947–954 (2019).

[126]A. Bhatnagar, A. Roy Chaudhuri, Y. Heon Kim, D. Hesse, and M. Alexe, "Role of domain walls in the abnormal photovoltaic effect in $BiFeO_3$", Nature Communications **4**, 2835 (2013).

[127]H. Matsuo, Y. Kitanaka, R. Inoue, Y. Noguchi, M. Miyayama, T. Kiguchi, and T. J. Konno, "Bulk and domain-wall effects in ferroelectric photovoltaics", Physical Review B **94**, 214111 (2016).

[128]D. J. Kim and M. Alexe, "Bulk photovoltaic effect in monodomain $BiFeO_3$ thin films", Applied Physics Letters **110**, 183902 (2017).

[129]H. Matsuo, Y. Noguchi, and M. Miyayama, "Gap-state engineering of visible-light-active ferroelectrics for photovoltaic applications", Nature Communications **8**, 207 (2017).

[130]S. Nakashima, T. Higuchi, A. Yasui, T. Kinoshita, M. Shimizu, and H. Fujisawa, "Enhancement of photovoltage by electronic structure evolution in multiferroic Mn-doped $BiFeO_3$ thin films", Scientific Reports **10**, 15108 (2020).

[131]R. P. S. M. Lobo, R. L. Moreira, D. Lebeugle, and D. Colson, "Infrared phonon dynamics of a multiferroic $BiFeO_3$ single crystal", Physical Review B **76**, 172105 (2007).

[132]S. Kamba, D. Nuzhnyy, M. Savinov, J. Šebek, J. Petzelt, J. Prokleška, R. Haumont, and J. Kreisel, "Infrared and terahertz studies of polar phonons and magnetodielectric effect in $BiFeO_3$", Physical Review B **75**, 024403 (2007).

[133]S. Chu, D. Singh, J. Wang, E.-P. Li, and K. Ong, "High optical performance and practicality of active plasmonic devices based on rhombohedral $BiFeO_3$", Laser & Photonics Reviews **6**, 684–689 (2012).

[134]D. Sando, P. Hermet, J. Allibe, J. Bourderionnet, S. Fusil, C. Carrétéro, E. Jacquet, J.-C. Mage, D. Dolfi, A. Barthélémy, P. Ghosez, and M. Bibes, "Linear electro-optic effect in multiferroic $BiFeO_3$ thin films", Physical Review B **89**, 195106 (2014).

[135]M. Zhu, Z. Du, Q. Liu, B. Chen, S. H. Tsang, and E. H. T. Teo, "Ferroelectric $BiFeO_3$ thin-film optical modulators", Applied Physics Letters **108**, 233502 (2016).

[136]N. Godard, P. Grysan, E. Defay, and S. Glinšek, "Growth of 100-oriented lead zirconate titanate thin films mediated by a safe solvent", Journal of Materials Chemistry C **9**, 281–287 (2021).

[137]A. Blázquez Martínez, N. Godard, N. Aruchamy, C. Milesi-Brault, O. Condurache, A. Bencan, S. Glinsek, and T. Granzow, "Solution-processed $BiFeO_3$ thin films with low leakage current", Journal of the European Ceramic Society **41**, 6449–6455 (2021).

[138]R. J. Errington, J. Ridland, W. Clegg, R. A. Coxall, and J. M. Sherwood, "β-diketonate derivatives of titanium alkoxides : X-ray crystal structures and solution dynamics of the binuclear complexes [Ti(OR)3(dik)2]", Polyhedron **17**, 659–674 (1998).

[139]G. Teowee, J. M. Boulton, K. Mccarthy, E. K. Franke, T. P. Alexander, T. J. Bukowski, and D. R. Uhlmann, "Effect of PbO content on the properties of sol-gel derived PZT films", Integrated Ferroelectrics **14**, 265–273 (1997).

[140]H. Miyazaki, T. Goto, Y. Miwa, T. Ohno, H. Suzuki, T. Ota, and M. Takahashi, "Preparation and evaluation of $LaNiO_3$ thin film electrode with chemical solution deposition", Journal of the European Ceramic Society **24**, 1005–1008 (2004).

[141]Q. Zhang, N. Valanoor, and O. Standard, "Chemical solution deposition derived (001)-oriented epitaxial $BiFeO_3$ thin films with robust ferroelectric properties using stoichiometric precursors (invited)", Journal of Applied Physics **116**, 066810 (2014).

[142]Q. Zhang, N. Valanoor, and O. Standard, "Epitaxial (001) $BiFeO_3$ thin-films with excellent ferroelectric properties by chemical solution deposition-the role of gelation", Journal of Materials Chemistry C **3**, 582–595 (2015).

[143]J. Gebhardt and A. M. Rappe, "Doping of $BiFeO_3$: A comprehensive study on substitutional doping", Physical Review B **98**, 1–16 (2018).

[144]J. Jutimoosik, S. Hunpratub, S. Maensiri, S. Rujirawat, and R. Yimnirun, "On preferred Mn site in multiferroic $BiFeO_3$: A view by synchrotron x-ray absorption near edge structure spectroscopy", Journal of Applied Physics **116**, 3–7 (2014).

[145]Y. Yoneda, Y. Kitanaka, Y. Noguchi, and M. Miyayama, "Electronic and local structures of Mn-doped $BiFeO_3$ crystals", Physical Review B **86**, 184112 (2012).

[146]B. C. Fritzler, S. Dharmavaram, R. T. Hartrim, and G. F. Diffendall, "Acetic Anhydride Hydrolysis at High Acetic Anhydride to Water Ratios", International Journal of Chemical Kinetics **46**, 151–160 (2014).

[147]F. Lotgering, "Topotactical reactions with ferrimagnetic oxides having hexagonal crystal structures—II", Journal of Inorganic and Nuclear Chemistry **16**, 100–108 (1960).

[148]N. Aruchamy, T. Schenk, S. Girod, S. Glinsek, E. Defay, and T. Granzow, "Influence of substrate stress on in-plane and out-of-plane ferroelectric properties of PZT films", Journal of Applied Physics **131**, 014101 (2022).

[149]T. Schenk, C. M. Fancher, M. H. Park, C. Richter, C. Künneth, A. Kersch, J. L. Jones, T. Mikolajick, and U. Schroeder, "On the Origin of the Large Remanent Polarization in La:HfO_2", Advanced Electronic Materials **5**, 1900303 (2019).

[150]X. Zheng, J. Li, and Y. Zhou, "X-ray diffraction measurement of residual stress in PZT thin films prepared by pulsed laser deposition", Acta Materialia **52**, 3313–3322 (2004).

[151]W. Kang, Y. Li, Z. Zheng, S. Yan, and R. Zhao, "The influence of structure evolution on dielectric performance in $BaZr_{0.1}Ti_{0.89}Fe_{0.01}O_3$ ceramics", Journal of Materials Science: Materials in Electronics **31**, 5746–5751 (2020).

[152]M. Birkholz, *Thin film analysis by x-ray diffraction*, 527 (Wiley, 2006).

[153]A. Glavic and M. Bjorck, "GenX 3 : the latest generation of an established tool", Journal of Applied Crystallography **55**, 1063–1071 (2022).

[154]P. Eaton and P. West, *Atomic Force Microscopy* (OUP Oxford, 2010).

[155]A. Gruverman, M. Alexe, and D. Meier, "Piezoresponse force microscopy and nanoferroic phenomena", Nature Communications **10**, 1661 (2019).

[156]B. J. Rodriguez, C. Callahan, S. V. Kalinin, and R. Proksch, "Dual-frequency resonance-tracking atomic force microscopy", Nanotechnology **18**, 475504 (2007).

[157]R. Nigon, T. M. Raeder, and P. Muralt, "Characterization methodology for lead zirconate titanate thin films with interdigitated electrode structures", Journal of Applied Physics **121**, 204101 (2017).

[158]R. Nigon, "Internal electric fields and electrode effects in ferroelectric thin films for piezoelectric energy harvesting", PhD thesis (2017).

[159]T. Schmitz, K. Prume, S. Tiedke, A. Roelofs, T. Schneller, U. Kall, M. Grossmann, R. Waser, C. Ganpule, A. Stanishefsky, and R. Ramesh, "Electrical measurements on capacitor sizes in the submicron regime for the characterization of real memory cell capacitors", Integrated Ferroelectrics **37**, 163–172 (2001).

[160]S. Tiedke and T. Schmitz, "Electrical Characterization of Nanoscale Ferroelectric Structures", in *Nanoscale characterisation of ferroelectric materials: scanning probe microscopy approach*, edited by M. Alexe and A. Gruverman (Springer Berlin Heidelberg, Berlin, Heidelberg, 2004), pp. 87–114.

[161]J. T. S. Irvine, D. C. Sinclair, and A. R. West, "Electroceramics: Characterization by Impedance Spectroscopy", Advanced Materials **2**, 132–138 (1990).

[162]A. R. West, D. C. Sinclair, and N. Hirose, "Characterization of Electrical Materials, Especially Ferroelectrics, by Impedance Spectroscopy", Journal of Electroceramics **1**, 65–71 (1997).

[163]J. R. Macdonald and a. J. Wiley, *Impedance Spectroscopy*, edited by E. Barsoukov and J. R. Macdonald (John Wiley & Sons, Inc., Hoboken, NJ, USA, Apr. 2018).

[164]W. H. G. Horsthuis and G. J. M. Krijnen, "Simple measuring method for electro-optic coefficients in poled polymer waveguides", Applied Physics Letters **55**, 616–618 (1989).

[165]B. A. Smith, S. Herminghaus, and J. D. Swalen, "Electrooptic Coefficients in Electric Field Poled Polymer Waveguides", MRS Proceedings **228**, 111 (1991).

[166]A. Boudrioua, E. Dogheche, D. Remiens, and J. C. Loulergue, "Electro-optic characterization of (Pb,La)TiO_3 thin films using prism-coupling technique", Journal of Applied Physics **85**, 1780–1783 (1999).

[167]B. Chen, P.-R. Hua, S.-Y. Xu, D.-Y. Yu, E. Y.-B. Pun, and D.-L. Zhang, "Mode Indices Measurement of a Special Ti-Diffused $LiNbO_3$ Waveguide Structure: A Strip Waveguide Array Embedded in a Planar Waveguide", IEEE Photonics Journal **4**, 1553–1559 (2012).

[168]P. K. Tien and R. Ulrich, "Theory of Prism–Film Coupler and Thin-Film Light Guides", Journal of the Optical Society of America **60**, 1325 (1970).

[169]E. Nitiss, A. Bundulis, A. Tokmakov, J. Busenbergs, E. Linina, and M. Rutkis, "Review and comparison of experimental techniques used for determination of thin film electro-optic coefficients", physica status solidi (a) **212**, 1867–1879 (2015).

[170]M. Sigelle and R. Hierle, "Determination of the electrooptic coefficients of 3-methyl 4-nitropyridine 1-oxide by an interferometric phase-modulation technique", Journal of Applied Physics **52**, 4199–4204 (1981).

[171]K. D. Singer, M. G. Kuzyk, W. R. Holland, J. E. Sohn, S. J. Lalama, R. B. Comizzoli, H. E. Katz, and M. L. Schilling, "Electro-optic phase modulation and optical second-harmonic generation in corona-poled polymer films", Applied Physics Letters **53**, 1800–1802 (1988).

[172]C. C. Teng and H. T. Man, "Simple reflection technique for measuring the electro-optic coefficient of poled polymers", Applied Physics Letters **56**, 1734–1736 (1990).

[173]D. Park, "Characterization of Linear Electro-Optic Effect of Poled Organic Thin Films", PhD thesis (2008).

[174]D. Sando, Y. Yang, E. Bousquet, C. Carrétéro, V. Garcia, S. Fusil, D. Dolfi, A. Barthélémy, P. Ghosez, L. Bellaiche, and M. Bibes, "Large elasto-optic effect and reversible electrochromism in multiferroic $BiFeO_3$", Nature Communications **7**, 10718 (2016).

[175]S. E. Park, S. Wada, L. E. Cross, and T. R. Shrout, "Crystallographically engineered $BaTiO_3$ single crystals for high-performance piezoelectrics", Journal of Applied Physics **86**, 2746–2750 (1999).

[176]S. Wada, K. Yako, H. Kakemoto, T. Tsurumi, and T. Kiguchi, "Enhanced piezoelectric properties of barium titanate single crystals with different engineered-domain sizes", Journal of Applied Physics **98**, 014109 (2005).

[177]K. Kariya, T. Yoshimura, S. Murakami, and N. Fujimura, "Enhancement of piezoelectric properties of (100)-orientated $BiFeO_3$ films on (100)$LaNiO_3$/Si", Japanese Journal of Applied Physics **53**, 09PA14 (2014).

[178]L. Liu, X. Qiu, S. Zhang, Z. Zhou, Y. Huang, L. Shu, Y.-Y.-S. Cheng, X. Wang, and J.-F. Li, "Impact of texturing on the phase transitions in sol–gel-processed Bi(Sm)FeO_3 thin films on $LaNiO_3$-buffered silicon", Journal of the American Ceramic Society **103**, 6554–6564 (2020).

[179]W. Sun, Z. Zhou, and J.-F. Li, "Sol–gel-processed (001)-textured $BiFeO_3$ thin films on Pt(111)/Ti/SiO_2/Si substrates with PbO seeding nanocrystals", RSC Advances **6**, 489–494 (2016).

[180]K. Nagasaka, N. Oshima, J. W. Kim, H. Shima, A. Akama, T. Kiguchi, K. Nishida, T. J. Konno, H. Funakubo, and H. Uchida, "Fabrication of $(100)_c$-oriented Mn-doped bismuth ferrite films on silicon and stainless steel substrates using calcium niobate nanosheets", Journal of the Ceramic Society of Japan **123**, 322–328 (2015).

[181]A. Kumar and D. Varshney, "Crystal structure refinement of $Bi_{1-x}Nd_xFeO_3$ multiferroic by the Rietveld method", Ceramics International **38**, 3935–3942 (2012).

[182]M. Slouf, R. Skoupy, E. Pavlova, and V. Krzyzanek, "High Resolution Powder Electron Diffraction in Scanning Electron Microscopy", Materials **14**, 7550 (2021).

[183]H. G. Yeo and S. Trolier-McKinstry, "001 Oriented piezoelectric films prepared by chemical solution deposition on Ni foils", Journal of Applied Physics **116**, 014105 (2014).

[184]L. Qiao and X. Bi, "Effect of different buffer layers on the microstructure and dielectric properties of $BaTiO_3$ thin films grown on Si substrates", Journal of Alloys and Compounds **477**, 560–564 (2009).

[185]M. H. G. Koster and G. Rijnders, eds., *Epitaxial Growth of Complex Metal Oxides* (Elsevier, 2015).

[186]Y.-H. Chu, Q. Zhan, L. W. Martin, M. P. Cruz, P.-L. Yang, G. W. Pabst, F. Zavaliche, S.-Y. Yang, J.-X. Zhang, L.-Q. Chen, D. G. Schlom, I.-N. Lin, T.-B. Wu, and R. Ramesh, "Nanoscale Domain Control in Multiferroic $BiFeO_3$ Thin Films", Advanced Materials **18**, 2307–2311 (2006).

[187]G. W. Pabst, L. W. Martin, Y.-H. Chu, and R. Ramesh, "Leakage mechanisms in $BiFeO_3$ thin films", Applied Physics Letters **90**, 072902 (2007).

[188]H. W. Jang, D. Ortiz, S.-H. Baek, C. M. Folkman, R. R. Das, P. Shafer, Y. Chen, C. T. Nelson, X. Pan, R. Ramesh, and C.-B. Eom, "Domain Engineering for Enhanced Ferroelectric Properties of Epitaxial (001) BiFeO Thin Films", Advanced Materials **21**, 817–823 (2009).

[189]I.-T. Bae, S. Yasui, T. Ichinose, M. Itoh, T. Shiraishi, T. Kiguchi, and H. Naganuma, "Growth mechanism and domain structure study on epitaxial $BiFeO_3$ film grown on $(La_{0.3}Sr_{0.7})(Al_{0.65}Ta_{0.35})O_3$", Journal of Applied Physics **127**, 245303 (2020).

[190]M. Rizwan, S. Gul, T. Iqbal, U. Mushtaq, M. H. Farooq, M. Farman, R. Bibi, and M. Ijaz, "A review on perovskite lanthanum aluminate $(LaAlO_3)$, its properties and applications", Materials Research Express **6**, 112001 (2019).

[191]Y. Bastani and N. Bassiri-Gharb, "Enhanced dielectric and piezoelectric response in PZT superlattice-like films by leveraging spontaneous Zr/Ti gradient formation", Acta Materialia **60**, 1346–1352 (2012).

[192]D. Kaewchinda, T. Chairaungsri, M. Naksata, S. Milne, and R. Brydson, "TEM characterisation of PZT films prepared by a diol route on platinised silicon substrates", Journal of the European Ceramic Society **20**, 1277–1288 (2000).

[193]Q. Ke, X. Lou, Y. Wang, and J. Wang, "Oxygen-vacancy-related relaxation and scaling behaviors of $Bi_{0.9}La_{0.1}Fe_{0.98}Mg_{0.02}O_3$", Physical Review B **82**, 024102 (2010).

[194]K. Min, F. Huang, Y. Jin, X. Lu, H. Wu, and J. Zhu, "Control of oxygen vacancies and their kinetic behaviours via reversible oxygen loss in $BiFeO_3$ ceramics", Journal of Physics D: Applied Physics **48**, 445301 (2015).

[195]C. H. Park, "Microscopic study on migration of oxygen vacancy in ferroelectric perovskite oxide", Journal of the Korean Physical Society **42**, 1420–1424 (2003).

[196]H. Matsuo, Y. Noguchi, and M. Miyayama, "Gap-state engineering of visible-light-active ferroelectrics for photovoltaic applications", Nature Communications **8**, 207 (2017).

[197]Microchem, *SU-8 3000 Permanent Epoxy Negative Photoresist*, 2000.

[198]M. Dawber, K. M. Rabe, and J. F. Scott, "Physics of thin-film ferroelectric oxides", Reviews of Modern Physics **77**, 1083–1130 (2005).

[199]M.-s. Chen, T.-B. Wu, and J.-m. Wu, "Effect of textured $LaNiO_3$ electrode on the fatigue improvement of $Pb(Zr_{0.53}Ti_{0.47})O_3$ thin films", Applied Physics Letters **68**, 1430–1432 (1996).

[200]T. Minami, "Transparent conducting oxide semiconductors for transparent electrodes", Semiconductor Science and Technology **20**, S35–S44 (2005).

[201]M. Martínez, J. Herrero, and M. Gutiérrez, "Deposition of transparent and conductive Al-doped ZnO thin films for photovoltaic solar cells", Solar Energy Materials and Solar Cells **45**, 75–86 (1997).

[202]R. Bel Hadj Tahar, T. Ban, Y. Ohya, and Y. Takahashi, "Tin doped indium oxide thin films: Electrical properties", Journal of Applied Physics **83**, 2631–2645 (1998).

[203]Z. Banyamin, P. Kelly, G. West, and J. Boardman, "Electrical and Optical Properties of Fluorine Doped Tin Oxide Thin Films Prepared by Magnetron Sputtering", Coatings **4**, 732–746 (2014).

[204]Y.-N. Kim, H.-G. Shin, J.-K. Song, D.-H. Cho, H.-S. Lee, and Y.-G. Jung, "Thermal Degradation Behavior of Indium Tin Oxide Thin Films Deposited by Radio Frequency Magnetron Sputtering", Journal of Materials Research **20**, 1574–1579 (2005).

[205]M. Espindola-Rodriguez, D. Sylla, Y. Sánchez, F. Oliva, S. Grini, M. Neuschitzer, L. Vines, V. Izquierdo-Roca, E. Saucedo, and M. Placidi, "Bifacial Kesterite Solar Cells on FTO Substrates", ACS Sustainable Chemistry & Engineering **5**, 11516–11524 (2017).

[206]H. Zhao, J. Kiwi, C. Pulgarin, and J. Yang, "Oxygen Distribution of Fluorine-doped Tin Oxide Films Coated on Float Glass along Depth Before and After Heat Treatment", International Journal of Applied Glass Science **4**, 242–247 (2013).

[207]S. Glinsek, M. A. Mahjoub, M. Rupin, T. Schenk, N. Godard, S. Girod, J.-B. Chemin, R. Leturcq, N. Valle, S. Klein, C. Chappaz, and E. Defay, "Fully Transparent Friction-Modulation Haptic Device Based on Piezoelectric Thin Film", Advanced Functional Materials **30**, 2003539 (2020).

[208]"EU-Directive 2002/95/EC: Restriction of the Use of Certain Hazardous Substances in Electrical and Electronic Equipment (RoHS).", Off. J. Eur. Union **46**, 19–23 (2003).

[209]J. Narayan, "Recent progress in thin film epitaxy across the misfit scale", Acta Materialia **61**, 2703–2724 (2013).

[210]A. K. Sharma, J. Narayan, C. Jin, A. Kvit, S. Chattopadhyay, and C. Lee, "Integration of $PbZr_{0.52}Ti_{0.48}O_3$ epilayers with Si by domain epitaxy", Applied Physics Letters **76**, 1458–1460 (2000).

[211]S. S. Rao, J. T. Prater, F. Wu, C. T. Shelton, J.-P. Maria, and J. Narayan, "Interface Magnetism in Epitaxial $BiFeO_3$-$La_{0.7}Sr_{0.3}MnO_3$ heterostructures integrated on si(100)", Nano Letters **13**, 5814–5821 (2013).

[212]R. A. McKee, F. J. Walker, and M. F. Chisholm, "Crystalline Oxides on Silicon: The First Five Monolayers", Physical Review Letters **81**, 3014–3017 (1998).

[213]G. De Luca, J. Spring, M. Kaviani, S. Jöhr, M. Campanini, A. Zakharova, C. Guillemard, J. Herrero-Martin, R. Erni, C. Piamonteze, M. D. Rossell, U. Aschauer, and M. Gibert, "Top-Layer Engineering Reshapes Charge Transfer at Polar Oxide Interfaces", Advanced Materials **34**, 2203071 (2022).

[214]F. Werner, "Hall measurements on low-mobility thin films", Journal of Applied Physics **122**, 10.1063/1.4990470 (2017).

[215]W. Cai, C. Fu, R. Gao, W. Jiang, X. Deng, and G. Chen, "Photovoltaic enhancement based on improvement of ferroelectric property and band gap in Ti-doped bismuth ferrite thin films", Journal of Alloys and Compounds **617**, 240–246 (2014).

[216]G. Abadias, E. Chason, J. Keckes, M. Sebastiani, G. B. Thompson, E. Barthel, G. L. Doll, C. E. Murray, C. H. Stoessel, and L. Martinu, "Review Article: Stress in thin films and coatings: Current status, challenges, and prospects", Journal of Vacuum Science & Technology A: Vacuum, Surfaces, and Films **36**, 10.1116/1.5011790 (2018).

[217]C. Guo-Feng, R. Yin-Jie, S. Yue, and Y. Han-Di, "Thermodynamic Stability and Thermal Expansion of Pure-phase $BiFeO_3$", Journal of Inorganic Materials **34**, 46 (2019).

[218]S. Hu, A. Alsubaie, Y. Wang, J. H. Lee, K.-R. Kang, C.-H. Yang, and J. Seidel, "Poisson's ratio of $BiFeO_3$ thin films: X-ray reciprocal space mapping under variable uniaxial strain", physica status solidi (a) **214**, 1600356 (2017).

[219]S.-R. Jian, H.-W. Chang, Y.-C. Tseng, P.-H. Chen, and J.-Y. Juang, "Structural and nanomechanical properties of $BiFeO_3$ thin films deposited by radio frequency magnetron sputtering", Nanoscale Research Letters **8**, 297 (2013).

[220]D. H. Kim, H. N. Lee, M. D. Biegalski, and H. M. Christen, "Effect of epitaxial strain on ferroelectric polarization in multiferroic $BiFeO_3$ films", Applied Physics Letters **92**, 1–4 (2008).

[221]M. Makarovic, M. Ç. Bayir, H. Ursic, A. Bradesko, and T. Rojac, "Domain wall conductivity as the origin of enhanced domain wall dynamics in polycrystalline $BiFeO_3$", Journal of Applied Physics **128**, 064104 (2020).

[222]O. F. Schirmer, M. Imlau, and C. Merschjann, "Bulk photovoltaic effect of $LiNbO_3$:Fe and its small-polaron-based microscopic interpretation", Physical Review B **83**, 165106 (2011).

[223]I. C. Infante, S. Lisenkov, B. Dupé, M. Bibes, S. Fusil, E. Jacquet, G. Geneste, S. Petit, A. Courtial, J. Juraszek, L. Bellaiche, A. Barthélémy, and B. Dkhil, "Bridging Multiferroic Phase Transitions by Epitaxial Strain in $BiFeO_3$", Physical Review Letters **105**, 057601 (2010).

[224]"Crafting the magnonic and spintronic response of $BiFeO_3$ films by epitaxial strain", Nature Materials **12**, 641–646 (2013).

[225]D. Ji, S. Cai, T. R. Paudel, H. Sun, C. Zhang, L. Han, Y. Wei, Y. Zang, M. Gu, Y. Zhang, W. Gao, H. Huyan, W. Guo, D. Wu, Z. Gu, E. Y. Tsymbal, P. Wang, Y. Nie, and X. Pan, "Freestanding crystalline oxide perovskites down to the monolayer limit", Nature **570**, 87–90 (2019).

[226]R. Guo, L. You, W. Lin, A. Abdelsamie, X. Shu, G. Zhou, S. Chen, L. Liu, X. Yan, J. Wang, and J. Chen, "Continuously controllable photoconductance in freestanding $BiFeO_3$ by the macroscopic flexoelectric effect.", Nature communications **11**, 2571 (2020).

[227]G. Dong, S. Li, M. Yao, Z. Zhou, Y.-Q. Zhang, X. Han, Z. Luo, J. Yao, B. Peng, Z. Hu, H. Huang, T. Jia, J. Li, W. Ren, Z.-G. Ye, X. Ding, J. Sun, C.-W. Nan, L.-Q. Chen, J. Li, and M. Liu, "Super-elastic ferroelectric single-crystal membrane with continuous electric dipole rotation", Science **366**, 475–479 (2019).

[228]A. Kumar, R. C. Rai, N. J. Podraza, S. Denev, M. Ramirez, Y.-H. Chu, L. W. Martin, J. Ihlefeld, T. Heeg, J. Schubert, D. G. Schlom, J. Orenstein, R. Ramesh, R. W. Collins, J. L. Musfeldt, and V. Gopalan, "Linear and nonlinear optical properties of $BiFeO_3$", Applied Physics Letters **92**, 67–70 (2008).

[229]A. Blázquez Martínez, P. Grysan, S. Girod, S. Glinsek, and T. Granzow, "Direct evidence for bulk photovoltaic charge transport in a ferroelectric polycrystalline film", Scripta Materialia **211**, 114498 (2022).

[230]C. Li, F. Yang, and W. L. Guo, "Strain-Induced Modulations of Electro-Optic and Nonlinear Optical Properties of ZnO: A First-Principles Study", Applied Mechanics and Materials **29-32**, 1803–1808 (2010).

[231]C. Paillard, S. Prokhorenko, and L. Bellaiche, "Strain engineering of electro-optic constants in ferroelectric materials", npj Computational Materials **5**, 6 (2019).

[232]K. D. Fredrickson, V. V. Vogler-Neuling, K. J. Kormondy, D. Caimi, F. Eltes, M. Sousa, J. Fompeyrine, S. Abel, and A. A. Demkov, "Strain enhancement of the electro-optical response in $BaTiO_3$ films integrated on $Si(001)$", Physical Review B **98**, 075136 (2018).

[233]M. Guennou, P. Bouvier, G. S. Chen, B. Dkhil, R. Haumont, G. Garbarino, and J. Kreisel, "Multiple high-pressure phase transitions in $BiFeO_3$", Physical Review B **84**, 174107 (2011).

[234]D. Sando, A. Barthélémy, and M. Bibes, "$BiFeO_3$ epitaxial thin films and devices: past, present and future", Journal of Physics: Condensed Matter **26**, 473201 (2014).

[235]L. You, F. Zheng, L. Fang, Y. Zhou, L. Z. Tan, Z. Zhang, G. Ma, D. Schmidt, A. Rusydi, L. Wang, L. Chang, A. M. Rappe, and J. Wang, "Enhancing ferroelectric photovoltaic effect by polar order engineering", Science Advances **4**, 1–10 (2018).

[236]C. Toulouse, J. Fischer, S. Farokhipoor, L. Yedra, F. Carlà, A. Jarnac, E. Elkaim, P. Fertey, J.-N. Audinot, T. Wirtz, B. Noheda, V. Garcia, S. Fusil, I. P. Alonso, M. Guennou, and J. Kreisel, "Patterning enhanced tetragonality in $BiFeO_3$ thin films with effective negative pressure by helium implantation", Physical Review Materials **5**, 024404 (2021).

[237]P. Dittrich, G. Montemezzani, P. Bernasconi, and P. Günter, "Fast, reconfigurable light-induced waveguides", Optics Letters **24**, 1508 (1999).

[238]F. Juvalta, B. Koziarska-Glinka, M. Jazbinsek, G. Montemezzani, K. Kitamura, and P. Günter, "Deep UV light induced, fast reconfigurable and fixed waveguides in Mg doped $LiTaO_3$", Optics Express **14**, 8278 (2006).

[239]Y. Kong, S. Liu, and J. Xu, "Recent Advances in the Photorefraction of Doped Lithium Niobate Crystals", Materials **5**, 1954–1971 (2012).

[240]C. Kittel, *Introduction to Solid State Physics, 8th edition* (Wiley, 2004).

[241]G. Shirane, E. Sawaguchi, and Y. Takagi, "Dielectric Properties of Lead Zirconate", Physical Review **84**, 476–481 (1951).

[242]C. A. Randall, Z. Fan, I. Reaney, L.-Q. Chen, and S. Trolier-McKinstry, "Antiferroelectrics: History, fundamentals, crystal chemistry, crystal structures, size effects, and applications", Journal of the American Ceramic Society **104**, 3775–3810 (2021).

[243]Y. Liu, R. Niu, A. Majchrowski, K. Roleder, K. Cordero-Edwards, J. M. Cairney, J. Arbiol, and G. Catalan, "Translational Boundaries as Incipient Ferrielectric Domains in Antiferroelectric $PbZrO_3$", Physical Review Letters **130**, 216801 (2023).

[244]Z. Liu, T. Lu, J. Ye, G. Wang, X. Dong, R. Withers, and Y. Liu, "Antiferroelectrics for Energy Storage Applications: a Review", Advanced Materials Technologies **3**, 1–21 (2018).

[245]P. Gao, C. Liu, Z. Liu, H. Wan, Y. Yuan, H. Li, Y. Pu, and Z.-G. Ye, "Softening of antiferroelectric order in a novel $PbZrO_3$-based solid solution for energy storage", Journal of the European Ceramic Society **42**, 1370–1379 (2022).

[246]P. Vales-Castro, R. Faye, M. Vellvehi, Y. Nouchokgwe, X. Perpiñà, J. M. Caicedo, X. Jordà, K. Roleder, D. Kajewski, A. Perez-Tomas, E. Defay, and G. Catalan, "Origin of large negative electrocaloric effect in antiferroelectric $PbZrO_3$", Physical Review B **103**, 054112 (2021).

[247]F. Wang, K. K. Li, and G. H. Haertling, "Transverse electro-optic effect of antiferroelectric lead zirconate thin films", Optics Letters **17**, 1122 (1992).

[248]P. P. Biswas, C. Milesi-Brault, A. B. Martínez, N. Aruchamy, L. Song, V. Kovacova, S. Glinšek, T. Granzow, E. Defay, and M. Guennou, "Birefringence induced by antiferroelectric switching in transparent polycrystalline $PbZr_{0.95}Ti_{0.05}O_3$ film", Physical Review Materials **6**, 1–7 (2022).

[249]K. Boldyreva, D. Bao, G. Le Rhun, L. Pintilie, M. Alexe, and D. Hesse, "Microstructure and electrical properties of $(120)_O$ -oriented and of $(001)_O$ -oriented epitaxial antiferroelectric $PbZrO_3$ thin films on (100) $SrTiO_3$ substrates covered with different oxide bottom electrodes", Journal of Applied Physics **102**, 10.1063/1.2769335 (2007).

[250]L. Pintilie, K. Boldyreva, M. Alexe, and D. Hesse, "Coexistence of ferroelectricity and antiferroelectricity in epitaxial $PbZrO_3$ films with different orientations", Journal of Applied Physics **103**, 10.1063/1.2831023 (2008).

[251]A. Roy Chaudhuri, M. Arredondo, A. Hähnel, A. Morelli, M. Becker, M. Alexe, and I. Vrejoiu, "Epitaxial strain stabilization of a ferroelectric phase in $PbZrO_3$ thin films", Physical Review B **84**, 1–8 (2011).

[252]M. P. Moret, J. J. Schermer, F. D. Tichelaar, E. Aret, and P. R. Hageman, "Structure and morphology of epitaxial $PbZrO_3$ films grown by metalorganic chemical vapor deposition", Journal of Applied Physics **92**, 3947–3957 (2002).

[253]T. Sa, N. Qin, G. Yang, and D. Bao, "W-doping induced antiferroelectric to ferroelectric phase transition in $PbZrO_3$ thin films prepared by chemical solution deposition", Applied Physics Letters **102**, 10.1063/1.4803941 (2013).

[254]C. Milesi-Brault, N. Godard, S. Girod, Y. Fleming, B. El Adib, N. Valle, S. Glinšek, E. Defay, and M. Guennou, "Critical field anisotropy in the antiferroelectric switching of $PbZrO_3$ films", Applied Physics Letters **118**, 10.1063/5.0029599 (2021).

[255]H. Aramberri, C. Cazorla, M. Stengel, and J. Íñiguez, "On the possibility that $PbZrO_3$ not be antiferroelectric", npj Computational Materials **7**, 196 (2021).

[256]R. Gao, S. E. Reyes-Lillo, R. Xu, A. Dasgupta, Y. Dong, L. R. Dedon, J. Kim, S. Saremi, Z. Chen, C. R. Serrao, H. Zhou, J. B. Neaton, and L. W. Martin, "Ferroelectricity in $Pb_{1+\delta}ZrO_3$ Thin Films", Chemistry of Materials **29**, 6544–6551 (2017).

[257]X. K. Wei, K. Vaideeswaran, C. S. Sandu, C. L. Jia, and N. Setter, "Preferential Creation of Polar Translational Boundaries by Interface Engineering in Antiferroelectric $PbZrO_3$ Thin Films", Advanced Materials Interfaces **2**, 1–5 (2015).

[258]Z. Fu, X. Chen, Z. Li, T. Hu, L. Zhang, P. Lu, S. Zhang, G. Wang, X. Dong, and F. Xu, "Unveiling the ferrielectric nature of $PbZrO_3$-based antiferroelectric materials", Nature Communications **11**, 1–8 (2020).

[259]X. G. Tang, A. L. Ding, Y. Ye, and H. L. Chan, "Preparation and characterization of lead zirconate thin films by chemical solution deposition", Chemistry of Materials **14**, 2129–2133 (2002).

[260]T. Tani and D. A. Payne, "Lead Oxide Coatings on Sol-Gel-Derived Lead Lanthanum Zirconium Titanate Thin Layers for Enhanced Crystallization into the Perovskite Structure", Journal of the American Ceramic Society **77**, 1242–1248 (1994).

[261]F. Liu, I. Fina, R. Bertacco, and J. Fontcuberta, "Unravelling and controlling hidden imprint fields in ferroelectric capacitors", Scientific Reports **6**, 25028 (2016).

[262]H. Pan, Z. Tian, M. Acharya, X. Huang, P. Kavle, H. Zhang, L. Wu, D. Chen, J. Carroll, R. Scales, C. J. G. Meyers, K. Coleman, B. Hanrahan, J. E. Spanier, and L. W. Martin, "Defect-Induced, Ferroelectric-Like Switching and Adjustable Dielectric Tunability in Antiferroelectrics", Advanced Materials **35**, 1–9 (2023).

[263]L. Song, J. Cardoletti, A. Blazquez Martinez, A. Bencan, B. Kmet, S. Girod, E. Defay, and S. Glinsek, "Low-temperature growth of piezoceramic films on glass", https://doi.org/10.48550/arXiv.2303.13103 (2023).

[264]L. Rebohle, S. Prucnal, and D. Reichel, *Flash Lamp Annealing*, Vol. 288, Springer Series in Materials Science (Springer International Publishing, Cham, 2019).

[265]E. Gilshtein, S. Bolat, G. T. Sevilla, A. Cabas-Vidani, F. Clemens, T. Graule, A. N. Tiwari, and Y. E. Romanyuk, "Inkjet-Printed Conductive ITO Patterns for Transparent Security Systems", Advanced Materials Technologies, 2000369 (2020).

[266]"Rapid and up-scalable manufacturing of gigahertz nanogap diodes", Nature Communications **13**, 3260 (2022).

[267]E. Yarali, H. Faber, E. Yengel, A. Seitkhan, K. Loganathan, G. T. Harrison, B. Adilbekova, Y. Lin, C. Ma, Y. Firdaus, and T. D. Anthopoulos, "Low-Voltage Heterojunction Metal Oxide Transistors via Rapid Photonic Processing", Advanced Electronic Materials **6**, 2000028 (2020).

[268]Y. Yao, A. B. Naden, F. Zhang, D. Edwards, P. Joshi, B. J. Rodriguez, A. Kumar, and N. Bassiri-Gharb, "Direct processing of $PbZr_{0.53}Ti_{0.47}O_3$ films on glass and polymeric substrates", Journal of the European Ceramic Society **40**, 5369–5375 (2020).

Contributions to this thesis

The work presented in this thesis is the result of scientific collaborations. The contributions of the collaborators are outlined below:

Chapter 4: TEM measurements were performed by O. Condurache and A. Bencan from the Jozef Stefan Institute. SIMS profiles were conducted by N. Valle and B. El-Adib from the Luxembourg Institute of Science and Technology. AFM/PFM images were obtained in collaboration with P. Grysan from the Luxembourg Institute of Science and Technology. DTA/TGA measurements were carried out by B. Marcolini. The development of F:SnO_2 was a joint effort with M. Melchiorre from the University of Luxembourg.

Chapter 5: AFM/PFM images were obtained in collaboration with P. Grysan. Line profile analysis of topography and amplitude images was performed by P. Grysan.

Chapter 6: COMSOL simulations were conducted by T. Granzow from the Luxembourg Institute of Science and Technology. The deposition of conductive F:SnO_2 was performed in collaboration with M. Melchiorre.

Appendix A: Thin film deposition was performed by A. Ost. from the Luxembourg Institute of Science and Technology. Structural and electrical characterization was carried out in collaboration with A. Ost. TEM measurements were performed by A. Bencan, M. Koblar, and G. Dražić from the Jozef Stefan Institute.

Appendix B: FLA crystallization was performed in collaboration with L. Song from the Luxembourg Institute of Science and Technology.

Appendix C: COMSOL simulations were performed by T. Granzow.

The work was supervised by T. Granzow and S. Glinsek. All work not mentioned above was performed solely by the author of this thesis.

Ph.D. Output

Publications

Articles in peer-reviewed journals

1. **A. Blázquez Martínez**, P. Grysan, S. Girod, S. Glinsek, N. Aruchamy, P. Biswas, M. Guennou, and T. Granzow, Strain Engineering of the Electro-Optic Effect in Polycrystalline $BiFeO_3$ Films [Invited], **Opt. Mater. Express** 13, 2061 (2023).

2. **A. Blázquez Martínez**, P. Grysan, S. Girod, V. Kovacova, S. Glinsek, and T. Granzow, Stress-Tuning the Bulk Photovoltaic Response in Polycrystalline Bismuth Ferrite Films, **Appl. Phys. Lett.** 122, 152903 (2023).

3. **A. Blázquez Martínez**, P. Grysan, S. Girod, S. Glinsek, and T. Granzow, Direct Evidence for Bulk Photovoltaic Charge Transport in a Ferroelectric Polycrystalline Film, **Scr. Mater.** 211, 114498 (2022).

4. P. P. Biswas, C. Milesi-Brault, **A. Blázquez Martínez**, N. Aruchamy, L. Song, V. Kovacova, S. Glinšek, T. Granzow, E. Defay, and M. Guennou, Birefringence Induced by Antiferroelectric Switching in Transparent Polycrystalline $PbZr_{0.95}Ti_{0.05}O_3$, **Phys. Rev. Mater.** 6, L091403 (2022).

5. **A. Blázquez Martínez**, N. Godard, N. Aruchamy, C. Milesi-Brault, O. Condurache, A. Bencan, S. Glinsek, and T. Granzow, Solution-Processed $BiFeO_3$ Thin Films with Low Leakage Current, **J. Eur. Ceram. Soc.** 41, 6449 (2021).

Submitted

1. L. Song,* J. Cardoletti,* **A. Blázquez Martínez**, A. Bencan, B. Kmet, S. Girod, E. Defay, and S. Glinsek, Low-Temperature Growth of Piezoceramic Films on Glass, **Under review** (2023).

Patents

1. **A. Blázquez Martinez**, T. Granzow. Transparent ferroelectric device. **LU 503207**. 2022.
2. N. Godard, S. Glinsek, **A. Blázquez Martinez**, E. Defay. Material deposition method. **WO 2021260165**. 2020.

Conferences

Oral Presentations

1. **A. Blázquez Martínez**, P. Grysan, S. Girod, N. Aruchamy, V. Kovacova, S. Glinsek, P. Biswas, M. Guennou and T. Granzow, "Bulk photovoltaic and electro-optic response in solution-processed $BiFeO_3$ films" European Materials Research Society Fall meeting 2022. **September 19th - 22nd 2022**. Warsaw, Poland.
2. **A. Blázquez Martínez**, P. Grysan, S. Girod, N. Aruchamy, V. Kovacova, S. Glinsek, P. Biswas, M. Guennou and T. Granzow, "Electro-optic effect in polycrystalline $BiFeO_3$ films" Photorefractive Photonics and beyond. **September 5th - 9st, 2022**. Monastier di Treviso, Italy.
3. **A. Blázquez Martínez**, P. Grysan, S. Girod, V. Kovacova, S. Glinsek, P. Biswas, M. Guennou and T. Granzow, "Linear electro-optic effect in polycrystalline $BiFeO_3$ films" IEEE ISAF. **June 27th - July 1st, 2022**. Tours, France.
4. **A. Blázquez Martínez**, P. Grysan, S. Girod, V. Kovacova, S. Glinsek, and T. Granzow, "Bulk Photovoltaic Effect in Solution Processed $BiFeO_3$ Films with Low Leakage" International conference on Advanced Electromaterials. **November 9th - November 12th, 2021**. Jeju Island, Korea.
5. **A. Blázquez Martínez**, P. Grysan, S. Girod, V. Kovacova, S. Glinsek, and T. Granzow, "Bulk photovoltaic effect in solution processed $BiFeO_3$ films with low leakage current" MASSENA Young Scientist Conference. **June 24th - 25th, 2021**. Lipperscheid, Luxembourg.
6. **A. Blázquez Martínez**, P. Grysan, S. Girod, V. Kovacova, S. Glinsek, and T. Granzow, "Influence of substrate stress on the bulk photovoltaic effect of polycrystalline bismuth ferrite thin films" IEEE ISAF. **May 16th - 23rd, 2021**. Sydney, Australia.

Summer Schools

1. 2022 UFFC Ferroelectrics School. **June 20th - 24th, 2022.** Lyon, France.
2. 6th International School of Oxide Electronics. **August 24th - September 3rd, 2021.** Cargèse, France.

3. Optically Controlled Ferroelectric Memristors. **October 22nd - 23rd, 2020.** Barcelona, Spain.